10-31-2018

Design and Application of Task-Specific GUMBOS and NanoGUMBOS for Sensing and Separation

Mingyan Cong
Louisiana State University and Agricultural and Mechanical College, mcong1@lsu.edu

DESIGN AND APPLICATION OF TASK-SPECIFIC GUMBOS AND NANOGUMBOS FOR SENSING AND SEPARATION

A Dissertation

Submitted to the Graduate Faculty of the
Louisiana State University
Agricultural and Mechanical College
In partial fulfillment of the
Requirements for the degree of
Doctor of Philosophy

in

The Department of Chemistry

by
Mingyan Cong
B.S. Shandong University, 2013
December 2018

I dedicate this dissertation to my parents, my husband, and my grandparents for their endless love and encouragement.

This dissertation is also dedicated to my advisor, Professor Isiah M. Warner, who has been a great source of knowledge, encouragement, and inspiration.

ACKNOWLEDGEMENT

I appreciate everyone that helped me throughout graduate school, especially:

Prof. Isiah M. Warner, for the opportunity to pursue doctoral research under his mentorship and his encouragement, inspiration, guidance, and constant support

Doctoral Committee Members: Prof. John A. Pojman, Prof. Louis H. Haber, and Prof. Neil Johannsen for their guidance, insightful questions and discussions

Dr. Waduge Indika Subodha Galpothdeniya for mentoring during my early doctoral research and introducing me to sensor research

Dr. Noureen Siraj, Dr. Pratap Chhotaray, Dr. Rocio Perez, and Dr. Sudhir Ravula for their discussions

Collaborators: Prof. Kevin S. McCarter, Dr. Ashleigh R. Wright, Dr. Nimisha Bhattarai, Dr. Paulina Kolic, Mi Chen, and Dr. Punprabhashi Vidanapathirana for their invaluable contribution to my thesis research

Warner Research Group for their endless support

TABLE OF CONTENTS

LIST OF TABLES

LIST OF FIGURES

SCHEME

LIST OF ABBREVIATIONS

BETI	Bis(pentafluorethane)sulfonamide
C_{16}mim	1-hexadecyl-3-methylimidazolium
CMC	Critical micelle concentration
CD	Circular dichroism
Cyt-c	Cytochrome c
DCM	Dichloromethane
ELISA	Enzyme-linked immunosorbent assay
FRET	Förster resonance energy transfer
FT-IR	Fourier transform infrared spectroscopy
IL	Ionic liquid
GUMBOS	Group of uniform materials based on organic salts
Hb	Hemoglobin
HOMO	Highest energy occupied molecular orbital
HSA	Albumin from human serum
LDA	Linear discriminant analysis
LUMO	Lowest energy unoccupied molecular orbital
Lys	Lysozyme
MSPE	Magnetic solid-phase extraction

NanoGUMBOS	Nanoparticles fabricated from GUMBOS
NTf2	Bis(trifluoromethylsulfonyl)imide
PC	1,1’-diethyl-2,2’-carbocyanine
PCA	Principal component analysis
PD	Polymethine dyes
PIC	1,1’-diethyl-2,2’-cyanine
PAGE	Polyacrylamide gel electrophoresis
RTILs	Room temperature ionic liquids
SDS	Sodium dodecyl sulfate
SPE	Solid-phase extraction
TSILs	Task specific ionic liquids
TC	Thiacarbocyanine
TEM	Transmission electron microscope
Trans	Transferrin
UV-vis	Ultraviolet-visible

ABSTRACT

The work presented in this dissertation employs task-specific materials for sensing and protein separation applications. These materials were derived from a ***g***roup of ***u***niform ***m***aterials ***b***ased on ***o***rganic ***s***alts (GUMBOS). GUMBOS are organic salts similar to ionic liquids, but have melting points ranging from 25 to 250 °C. As with ionic liquids, the properties of GUMBOS can be easily tuned by changing the counter-ion. Thus, task-specific GUMBOS can be designed and prepared with properties that are beneficial for applications in sensing or protein separation. In this dissertation, the selective responsive behavior of a series of GUMBOS and nanomaterials derived from GUMBOS (nanoGUMBOS) were evaluated. Firstly, binary nanoGUMBOS, containing two cyanine cations, were synthesized and characterized. Based on significant spectral overlap and differences in reactivity towards hydroxyl radicals, the two cyanine cations in the binary nanoGUMBOS were able to generate a ratiometric fluorescence response. These results suggest a promising ratiometric probe for detection and quantification of hydroxyl radicals. This approach of investigating binary nanoprobes will serve as the basis for designing other cyanine-based fluorescent probes for biosensing and imaging. Secondly, a series of cyanine-based GUMBOS were combined to serve as a sensor array for detection of proteins. The cyanine-based sensor elements utilized in this sensor array, exhibit different aggregation behaviors when mixed with the seven proteins, giving various fluorescence responses. The resulting responses exhibited cross-reactive patterns, which can be analyzed to discriminate

proteins at a low concentration. Finally, nanoGUMBOS derived from imidazolium ionic liquids and magnetic dysprosium-based anions were designed as magnetic, nanoadsorbent materials for selective hemoglobin isolation. These nanoGUMBOS were successfully applied in selective hemoglobin (Hb) isolation from human whole blood. All studies presented in this dissertation demonstrate promising advantages of GUMBOS-based materials in the field of sensing and protein separation.

CHAPTER 1: INTRODUCTION

1.1 Ionic Materials

1.1.1 Ionic Liquids

Ionic liquids (ILs), are defined as low melting (melting points less than 100 °C) organic salts that are typically composed of a combination of bulky cations and anions. [1] These liquid salts typically have properties such as thermal stability, wide liquid temperature range, considerable ionic conductivities, broad electrochemical window, and good solubility and miscibility. [2, 3] ILs were first recorded in 1914 by Paul Walden, who designed and studied ethylammonium nitrates. [4, 5] In 1948, Frank H. Hurley and Thomas P. Wier synthesized a series of chloroaluminate ILs by combining quaternary heterocyclic cations with aluminum chloride. [6] In the following years, more chloroaluminate ILs were discovered and studied for various applications. [7-11] Unfortunately, these findings did not gain much attention due to their sensitivity to moisture.

A major step forward in ILs was made by John S. Wilkes and Michael J. Zaworotko in 1992, through the report of moisture stable ILs based on 1-ethyl-3-methylimidazolium cation and either a tetrafluoroborate or hexafluorophosphate counter-anion. [12] Since then, development of ILs has grown exponentially. Examples of the commonly used ILs cations and anions are listed in Figure 1.1. [13]

As organic salts, the physicochemical properties of ILs can be tuned simply through pairing

of counter-ions. In 2001, the concept of task specific ionic liquids (TSILs) was conceived by Rogers *et al.* using amine and thiol groups to extract mercury and cadmium ions from water. [14] ILs can also be designed to possess magnetic, [15, 16] protic, [17-19] chiral, [20-22] luminescent, [23-25] ion conductive, [26-28] and catalytic. [29, 30] These characteristics allow ILs to be applied to be used in various areas including as solvents for targeted synthesis,[31] biological reaction media, [32] extraction, [14, 33, 34] catalysis, [1, 29] sensing, [35-37] as well as energy storage and conversion. [38-40]

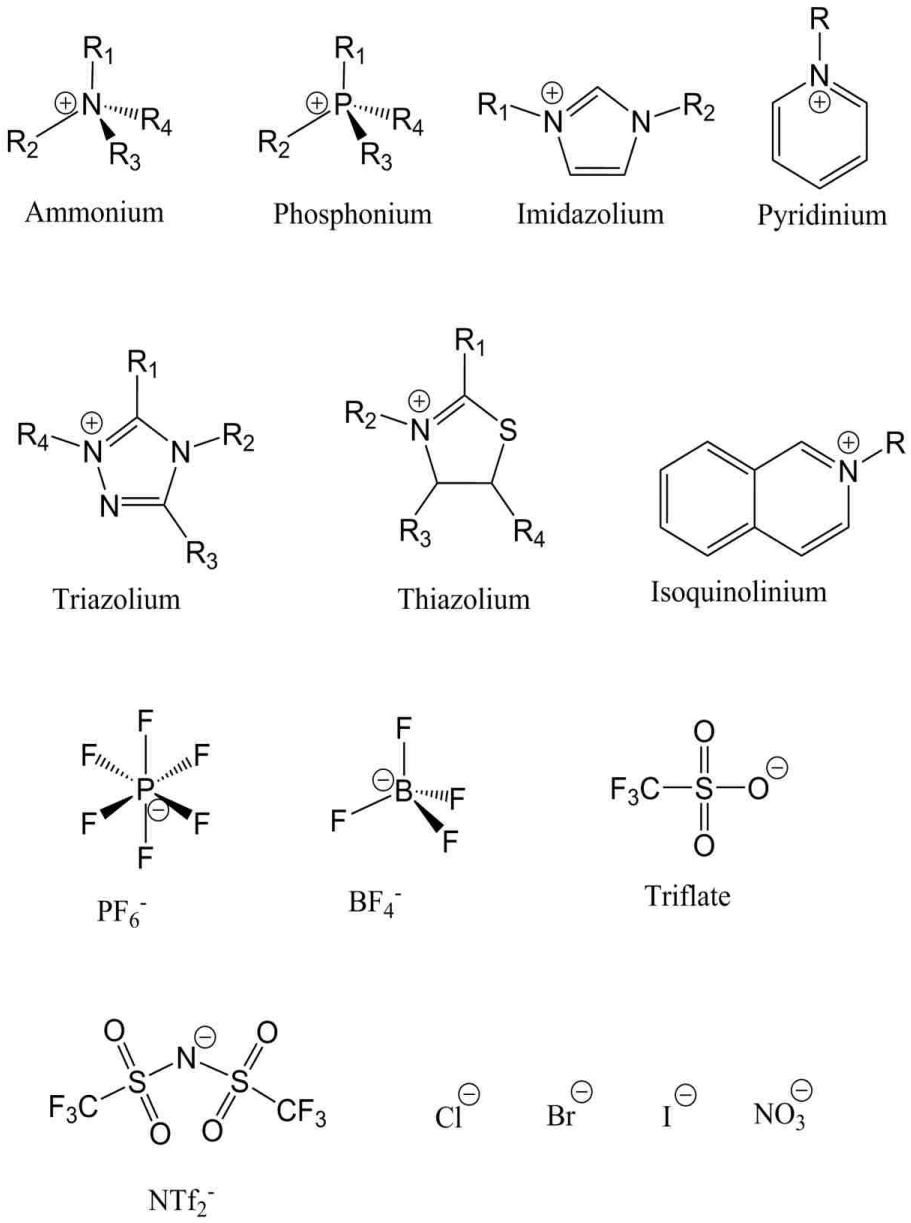

Figure 1.1. Commonly used ILs cations and anions

1.1.2 Group of Uniform Material Based on Organic Salts

As mentioned earlier, ILs are organic salts with melting points below 100 ºC. Room temperature ionic liquids (RTILs) are ILs that are liquid below room temperature. The low

melting points of these salts is the reason why most applications of ILs use RTILs. Frozen ILs are defined as ILs with melting points above room temperature. These salts are typically reported in applications such as rewritable imaging, [41] and dye-sensitized solar cells. [42]

GUMBOS (**g**roup of **u**niform **m**aterial **b**ased on **o**rganic **s**alts) are solid phase organic salts with tunable properties similar to ILs, but with a wider range of melting points (25°C to 250°C). This group of materials was first introduced by Isiah Warner *et al.* in 2008. [43] Figure 1.2 shows a diagram of the defined melting point ranges of ILs, RTILs, frozen ILs and GUMBOS.

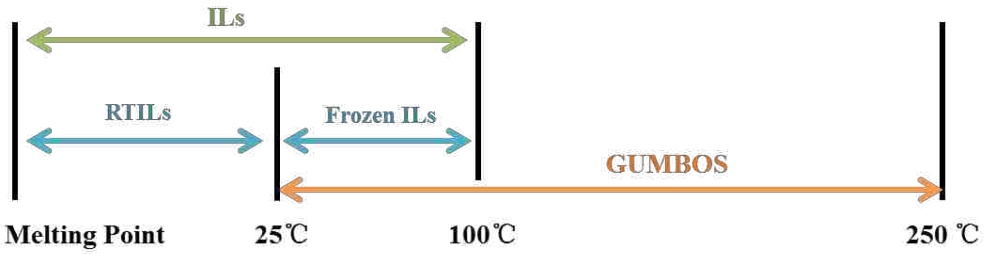

Figure 1.2. Melting point ranges of ILs, RTILs, Frozen ILs, and GUMBOS

GUMBOS exhibit many of the desired tunable properties of ILs, including high thermal stability, low volatility, and high ionic conductivity. [43, 44] A variety of GUMBOS have been prepared in the Warner research group with unique fluorescent, magnetic, sensing, and tumor-targeting properties. [2, 43, 45-47] For example, Min Li and coworkers synthesized a multifunctional lipophilic phosphonium–lanthanide GUMBOS that simultaneously possess paramagnetism, luminescence, and tumor mitochondrial targeting properties. [48] In another work, it was found that by simply altering the anion of rhodamine 6G, the tumor-targeting property is

tuned due to the variation of hydrophobicity. [49]

1.1.3 Preparation of GUMBOS

Similar to the synthesis of ILs, GUMBOS synthesis is fairly simple and does not require laborious, time-consuming procedures. An ion-exchange reaction is the most widely used method for preparation of GUMBOS when a bulky organic counter-ion is introduced. There are two representatives for such a reaction. The first representative reaction is the preparation of the hydrophobic GUMBOS 3,3'-diethylthiacarbocyanine bis(pentafluoroethane)sulfonimide ([TC1][BETI]) (Figure 1.3). This reaction was performed in a biphasic mixture of water and dichloromethane (DCM) under ambient conditions and was completed in 24 hours. A slight molar excess of lithium bis(pentafluoroethane)sulfonimide (Li[BETI]) is required to push the reaction to completion. The compounds 3,3'-diethylthiacarbocyanine iodide ([TC1][I]) and lithium bis(pentafluoroethane)sulfonimide (Li[BETI]) at a molar ratio of 1 to 1.1 are allowed to stir for 24 h at room temperature. After the reaction is complete, the aqueous phase is discarded and the IL containing organic phase is washed several times with distilled water to remove any remaining lithium iodide byproduct. Finally, DCM is removed under reduced pressure. [46]

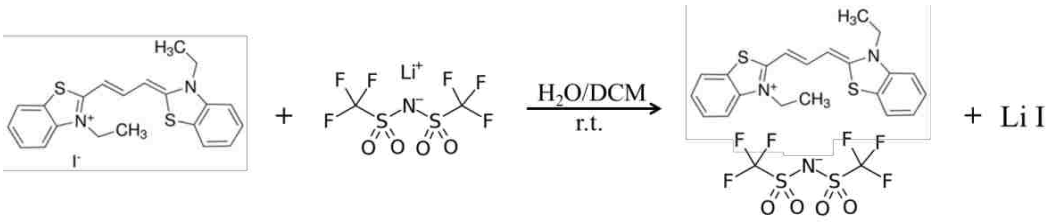

Figure 1. 3. Synthesis of hydrophobic [TC1][BETI] GUMBOS

The second representative ion-exchange reaction is the preparation of hydrophilic GUMBOS rhodamine 6G trifluoromethanesulfonate ([R6G][OTf]) and rhodamine 6G ascorbate ([R6G][Asc]). This is a one-phase reaction. As shown in Figure 1.4, the starting materials, rhodamine 6G chloride ([R6G][Cl]) and sodium trifluoromethanesulfonate ([Na][OTf]) are dissolved in anhydrous acetonitrile and stirred for 72 h. The byproduct NaCl is removed by filtration. Acetonitrile is removed under vacuum, yielding the pure [R6G][OTf] GUMBOS. [49]

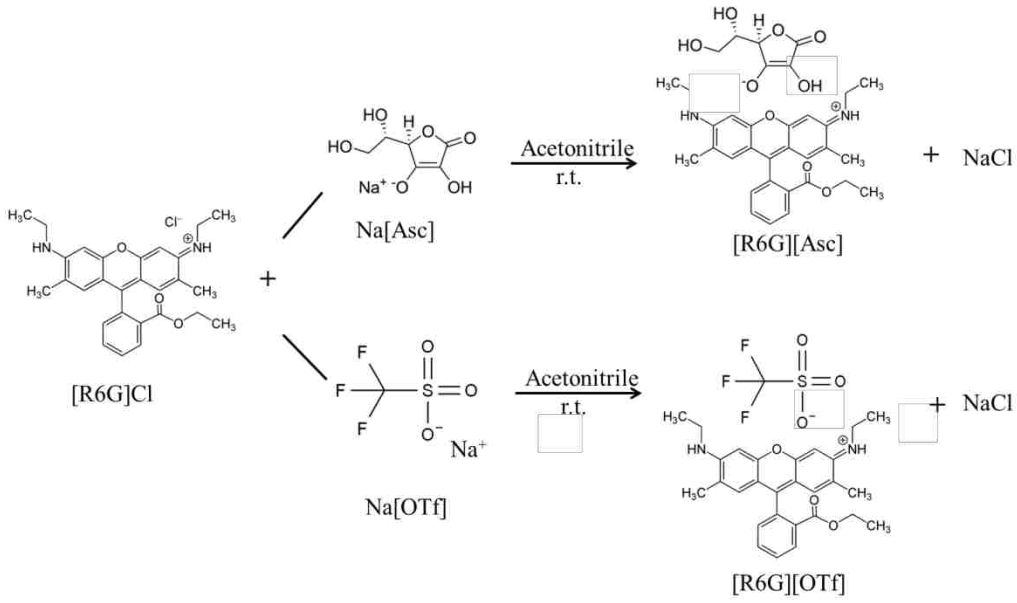

Figure 1. 4. Synthesis of hydrophilic GUMBOS [R6G][OTf] and [R6G][Asc]

1.1.4 Nanoparticles Derived from GUMBOS

Nanoparticles were initially studied because of their size-dependent physical and chemical properties. [50, 51] In recent years, the unique properties and utility of nanoparticles for a variety of biological applications including drug delivery, [52, 53] enhancing conductivity, [54, 55] battery improvement, [56-58] medical imaging, [59-61] sensing, [62-64] and thermal therapy [65-67] have been reported. Nanomaterials fabricated from GUMBOS (nanoGUMBOS) are able to provide several complementary properties into one nanoscale material, which allows us to develop multifunctional organic nanomaterials easily. [68-70]

Preparation of uniform and ambient-stable nanoparticles from GUMBOS has been studied for a wide variety of applications. [43, 46, 47, 69, 71-78] Following these studies, there has been an upsurge of interest in the application of nanomaterials fabricated from solid-state organic salts. Many approaches have been developed for the preparation of nanoGUMBOS. Reprecipitation is the most commonly used technique, although other techniques such as cyclodextrin-assisted,[79] microwave-assisted, [80] and surfactant-assisted [81] syntheses were also available. In this dissertation, nanoGUMBOS were prepared using the reprecipitation method as seen in Figure 1.5. In this method, the GUMBOS material is dissolved in a suitable volatile organic solvent to make a concentrated stock solution. A small volume of the stock solution is then pipetted rapidly into water under sonication. After aging for 15 to 60 min, dispersed nanoparticles would be obtained.

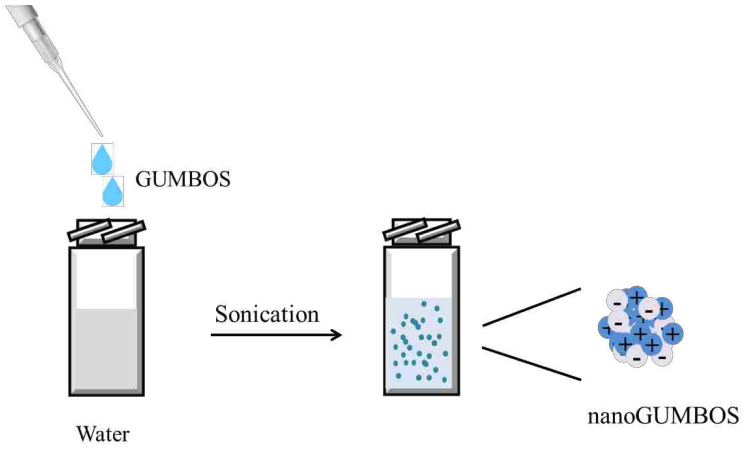

Figure 1. 5. Preparation of nanoGUMBOS through reprecipitation method

In addition to reprecipitation, a reverse micelle method is also commonly used for preparation of nanoGUMBOS. [45, 81] Micelles are aggregates formed from surfactant monomers above their critical micelle concentration (CMC). Typically, micelles are formed in aqueous medium, in which the hydrophilic heads are on the outside and the hydrophobic tails buried in the interior. Conversely, reverse micelles are formed in organic medium wherein the hydrophobic tails face the external medium and the hydrophilic head face inward. Since these reverse micelles are able to stabilize relatively large water pools of defined size, this reverse micelle system is suitable for formation of relatively monodispersed nanoparticles. [82, 83]

1.2 Chemical Sensors

1.2.1 Chemical Sensors: Definition and Components

A chemical sensor is a device that is used to determine the presence or quantity of an analyte, and transform chemical information to real-time analytical information. [84, 85] An ideal chemical sensor should be inexpensive, stable, easy to use, and selectively responsive to a target analyte at required concentrations. Over the past few decades, researchers have disclosed intensive efforts to develop and improve sensor performance with the aim of making ideal chemical sensors.

Chemical sensors have two main functions, recognition and transduction. [86-88] It is very important that interaction occurs between the sensor and the analyte of interest. This interaction can be selective or partially selective and usually take place as chemical or physical reactions，which will change the properties of the chemical sensors. Figure 1.6 is a display of a representative chemical sensor operation. In the transduction step, chemical sensors convert the unmeasurable interactions into measurable physical properties, such as mass, conductivity, light intensity and refractive index. This allows people to assess and quantify the alteration in reaction components. While the sensor does not respond to a square analyte, it shows partial selectivity towards the other three analytes and gives similar signals with different intensities. In this study, if the analyte of interest is the orange analyte, the oval and triangle analytes can be considered interferences.

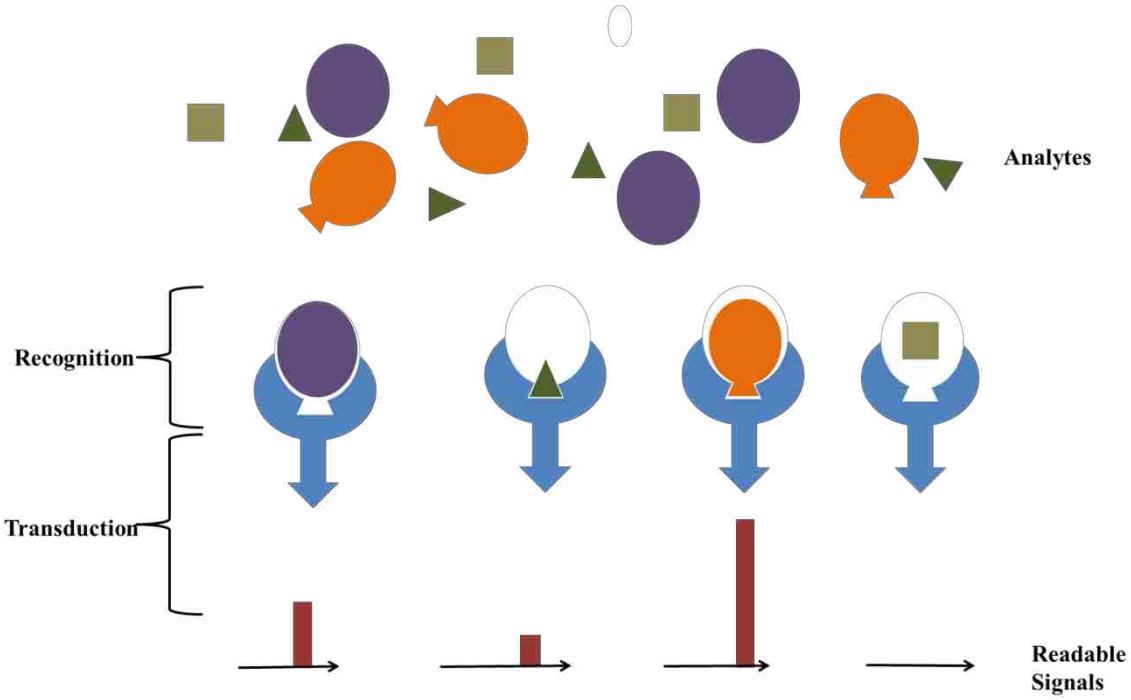

Figure 1. 6. Representative scheme of a partially selective chemical sensor.

1.2.2 Chemical Sensor Arrays

With the properties of an ideal chemical sensor in mind, the requirement of a selective response to a particular target analyte at any required concentrations seems far from reality. Most often, a chemical sensor only has partial selectivity. Sensor arrays are a complementary approach that could put partially selective sensors into good use.

The representative and most widely known sensor arrays are electronic noses, or artificial sensor arrays of odorants. [89, 90] These sensor arrays were inspired by the biological olfactory system, where there are thousands of odor receptors. Upon interaction with odorant molecules, electrical signals are generated and transported from the receptor to brain through neurons. [91, 92]

Interestingly, these olfactory receptors are not strictly “lock-and-key” with any specific odorants; instead, they are partially selective. [93-95] In other words, an olfactory receptor has the ability to respond to many odorants, and many receptors are able to interact with one odorant. Thus, pattern recognition systems are considered an essential element of the olfactory signal processing and analyzing.

Similar to olfactory system, a chemical sensor array contains an assembly of cross-reactive sensor elements and an appropriate pattern recognition system. [96-98] A graphical representation of a sensor array operation is displayed in Figure 1.7, where partially selective interactions between the sensing elements and analytes generate unique sensor response patterns. The patterns contain information about each analyte and can be used as the fingerprint for a given analyte of interest.

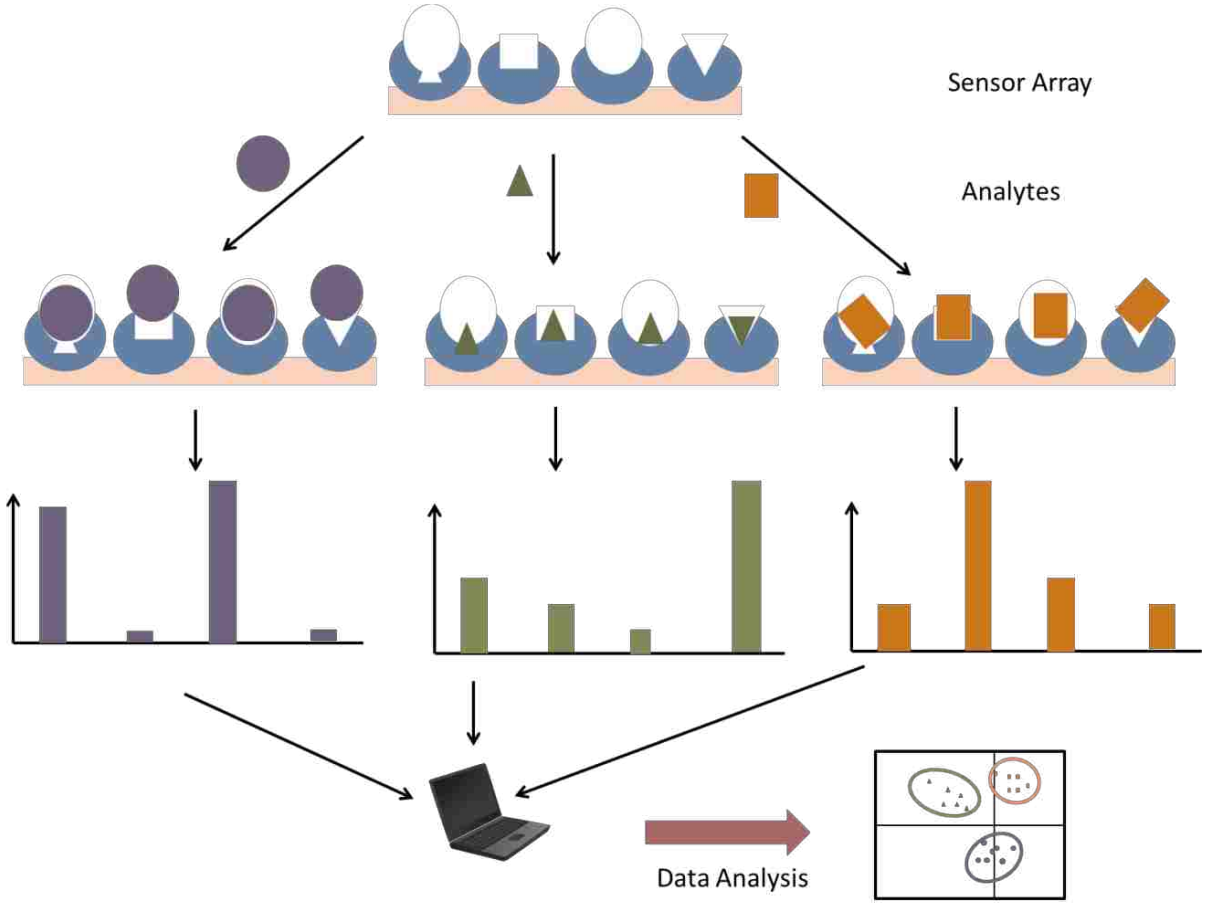

Figure 1. 7. Graphic representation of a chemical sensor array

This array-based sensing method offers the ability to respond to a variety of different analytes. Moreover, sensor arrays have the potential of generating unique signals for complex but distinctive analyte mixtures. In recent decades, chemical sensor arrays have been reported to successfully discriminate volatile organic compounds (VOCs), [99] visualize odors, [100] detect and monitor the growth of bacteria [99] and cancer cells. [101] In this dissertation, a series of cyanine-based GUMBOS were used to perform array-sensing of proteins. Each GUMBOS served as a sensor element and had partial selectivity. Data was analyzed using a pattern recognition system combining principal component analysis and linear discrimination analysis.

This sensor array showed impressive performance of discriminating protein mixtures at different concentration levels.

1.3 Protein Structure

Proteins are macromolecules that play important roles in biological activities. The function of proteins depend on their structure, which has four levels: primary, secondary, tertiary, and quaternary (Figure 1.8). [102, 103] Amino acids are the building blocks of proteins. An amino acid consists of a central carbon linked to an amino group, a hydrogen atom, a carboxyl group, and a side chain. Through a condensation reaction, amino acids are able to link together via peptide bonds, and form a peptide chain. This linear chain of amino acids is known as the primary structure of a protein. The peptide chain can be coiled to form a random coil, α helix, or β sheet through intramolecular hydrogen bonding. These stable coiling peptide chains represent the secondary structure of a protein. Most of the time, one protein contains several random coil, α-helices and β-sheets. They interact, fold and twist in order to achieve lower energy levels and higher stability. The resulting three-dimensional structure is designed as the tertiary structure of the protein. The tertiary structure is primarily stabilized by interactions between the side groups of amino acids, which include hydrogen bonding, disulfide bonding, ionic bonding, dipole-dipole interactions, hydrophobic interaction and London dispersion forces. [104] While some proteins only contain one polypeptide chain with a tertiary structure, many proteins contain several polypeptide subunits. These subunits are assembled together through those amino acid

side chain interactions mentioned above and form a quaternary structure.

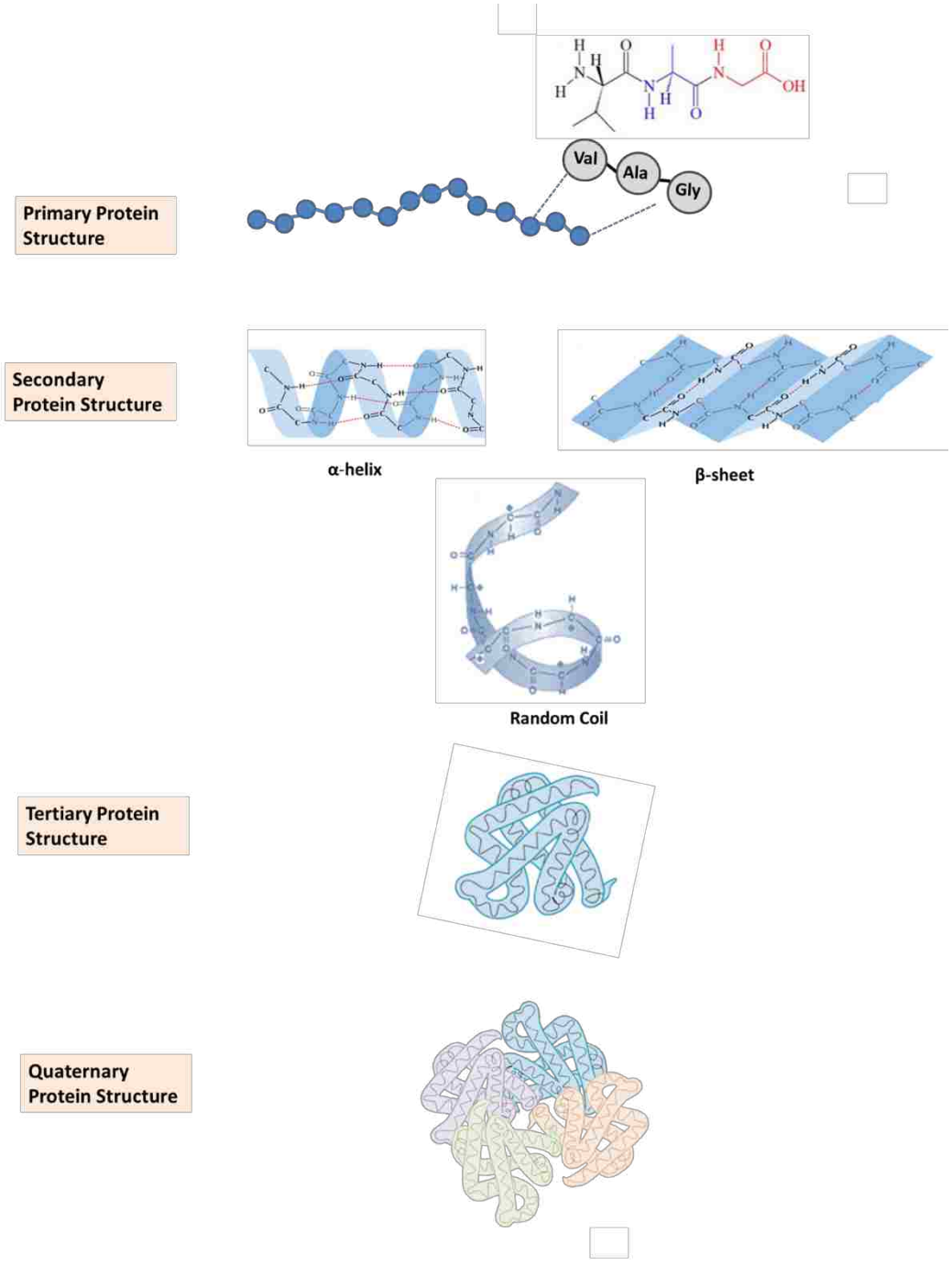

Figure 1. 8. Four levels of protein structure

1.4 Protein Extraction and Separation

Before a specific protein present in a complex mixture can be studied for further applications, protein extraction and separation are often essential steps. Various analytical methods have been used to separate or extract proteins from complicated biological matrices, such as plant or animal tissues. The most conventionally used protein separation methods are chromatography, such as size exclusion chromatography and reverse phase chromatography; [101, 105-107] fractionation techniques such as sonication, centrifugation and filtration; [108-110] gel electrophoresis;[111, 112] solvent extraction using organic solvents or ionic liquids; [113-115] and solid-phase protein extraction. [116-118] In this dissertation, GUMBOS were used to design a magnetic nanoparticle that was capable of selectively extracting hemoglobin from whole blood.

1.4.1 Hemoglobin Isolation

Hemoglobin (Hb) is a protein present in red blood cells that plays an essential role in the transportation of oxygen. As shown in Figure 1.9, Hb proteins consist of four subunits, two α-chains and two β-chains. Each subunit contains a heme group with a ferrous atom at the center of each heme ring. Four of the six ferrous coordination sites are occupied by nitrogen atoms from the heme porphyrin ring. One of the vertical coordination sites is occupied by a nitrogen atom from a histidine side chain. The last vertical coordination site is left available to bind to an oxygen molecule.

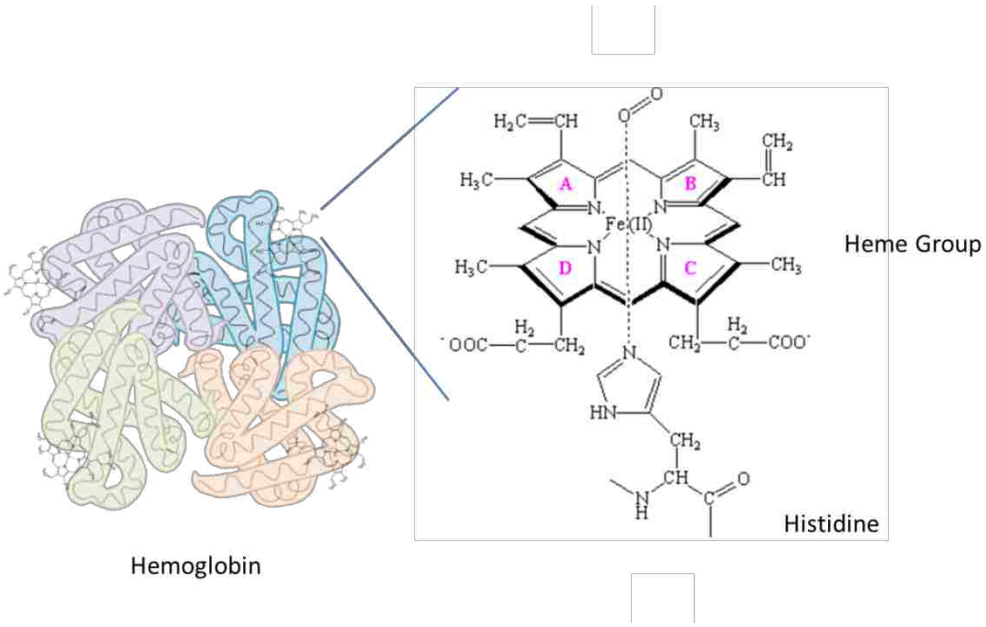

Figure 1. 9. Hemoglobin and heme group

Hb's oxygen transportation properties make it potentially useful for production of blood substitutes for blood transfusions in extreme situations, particularly for persons with rare types of blood. [119, 120] Therefore, as a prerequisite step for such investigations, isolation of Hb has drawn considerable attention over the last decade. In this dissertation, a magnetic nanoadsorbent GUMBOS was developed for selective Hb isolation. In this nanomaterial, the imidazolium cation serves as a selective Hb affinity group, while dysprosium contributes paramagnetic properties. The affinity interaction between imidazolium and the heme group from hemoglobin is shown in Figure 1.10, where a coordinating bond forms between the nitrogen atom in the imidazolium cation and the ferrous atom in the heme group.

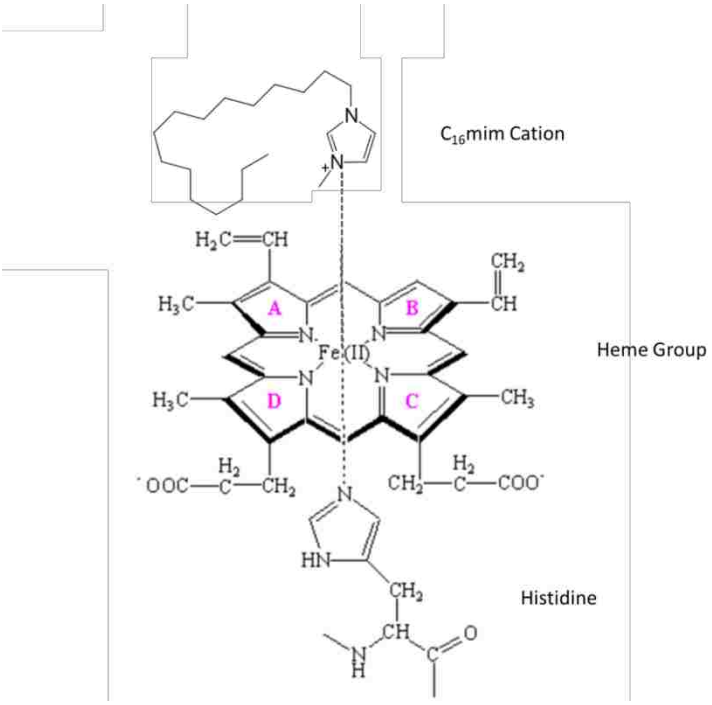

Figure 1. 10. Affinity interaction between heme group and imidazolium cation

1.5 Analytical Techniques

1.5.1 Ultraviolet-Visible Spectroscopy

Ultraviolet visible (UV-Vis) spectroscopy is an analytical technique, that measures the absorption of photons of light by a sample in the ultraviolet and visible light region (uv <400 nm, visible = 400 to 800 nm). The ultraviolet and visible light region comprises light energy of approximately 36 kcal/mol to 143 kcal/mol. When a molecule absorbs light, the absorbed energy promotes one electron from a lower energy level to a higher energy level. In particular, the promotion of electron from the highest energy occupied molecular orbital (HOMO) to the lowest energy unoccupied molecular orbital (LUMO) is energetically favored. The wavelength or

energy of an absorbed photon can be explained using a molecular orbital diagram. For example, Figure 1.11 is a diagram explaining the electron excitation of an ethene molecule. If a molecule is exposed to a photon of light with energy equal to the HOMO-LUMO energy gap (ΔE), this photon will be absorbed. The absorbed energy promotes one electron from the HOMO to the LUMO. In this case, ethene absorbs light with wavelength of 165 nm and energy of 173 kcal/mol.

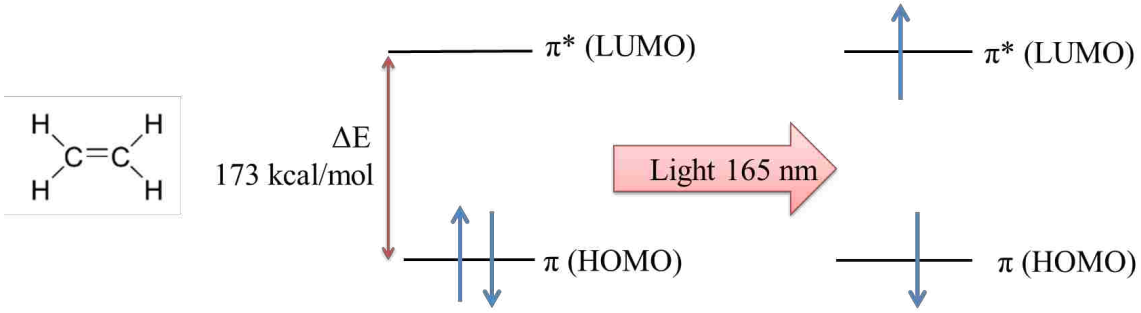

Figure 1. 11. Partial molecular orbital diagram showing the electronic excitation of ethene

Molecules with conjugated double bonds, e.g. polyaromatic hydrocarbons, tend to have a narrower energy gap between the HOMO and the LUMO. This allows these conjugated π systems to absorb light of longer wavelength. As a result, most of these molecules have distinct absorption energies. The molecular orbital diagram for 1,3-butadiene, the simplest conjugated system, is shown in Figure 1.12. In comparison to ethene, the narrower HOMO-LUMO gap allows 1,3-butadiene to absorb light with energy of 132 kcal/mol and wavelength of 217 nm.

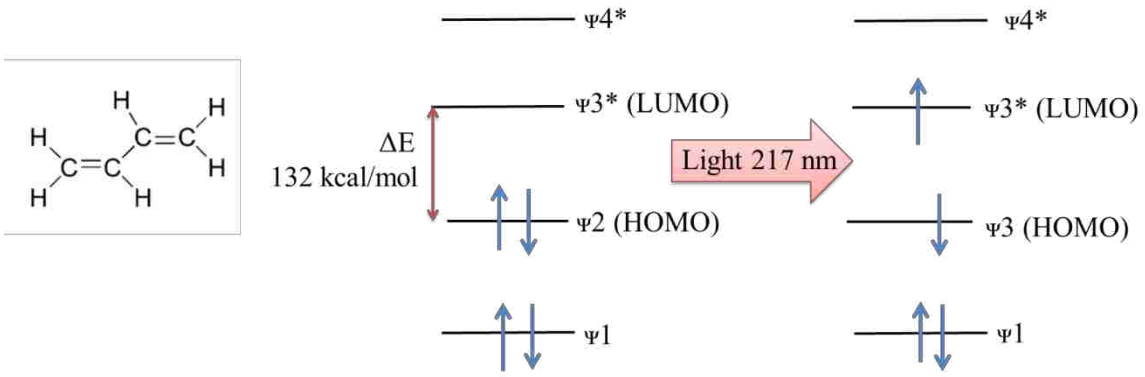

Figure 1. 12. Partial molecular orbital diagram showing the electronic excitation of 1,3-butadiene

Absorbance is defined to represent the amount of light absorbed. It can be determined by measuring the transmission of light through the sample. Assume that the sample has low scatter, thus almost all of the light not absorbed will be transmitted.

$$T = I/I_0, \qquad (1.1)$$

where T is transmission, I_0 is the intensity of the incident light, I is the intensity of the transmitted light.

Transmission can be converted to absorbance (A) using the following equation:

$$A = log_{10}(\frac{1}{T}). \qquad (1.2)$$

The amount of light absorbed by a sample is proportional to the amount of absorbing molecules in the given sample, in the region where the spectrometer light beam transverses. In Beer's Law "molar absorptivity (ε)" is defined to be the ability of an analyte to absorb light at a

given wavelength, and correlates the absorbance value to the concentration of the analyte, as demonstrated in the following equation:

$$A=\varepsilon bc, \qquad (1.3)$$

where A is absorbance value, ε is molar absorptivity ($L \cdot mol^{-1} \cdot cm^{-1}$), b is path length of the cuvette (cm), c is concentration of analyte ($mol \cdot L^{-1}$). [121]

The working principle of a UV-Vis spectrophotometer is displayed in Figure 1.13. The light source of a UV-Vis spectrometer is typically designed as a combination of a deuterium lamp with a tungsten lamp. This allows coverage of the entire UV and visible light range. The light beam first reaches a monochromator, that only allows light with a desired wavelength to pass through. Then, the beam will be split into two beams by a beam-splitter. One beam passes through a reference cell, the other passes through the sample cell. A detector records the absorbance of both the reference and the sample.

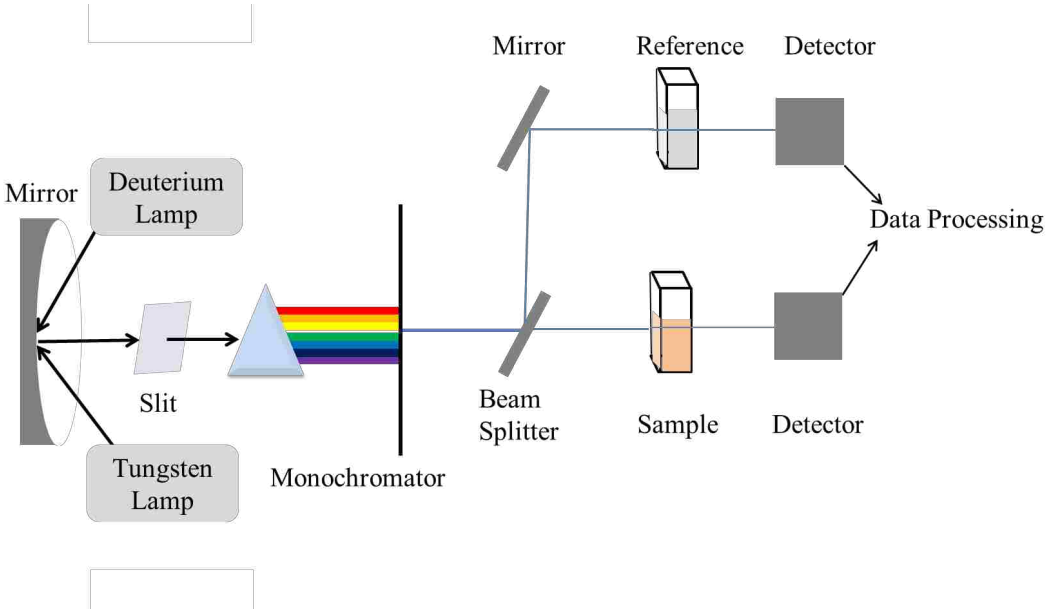

Figure 1. 13. Schematic diagram of a conventional UV-Vis spectrometer

1.5.2 Fluorescence Spectroscopy

Fluorescence is a form of luminescence that involves emission of light from electronically excited states not created by heat. Luminescence can be a result of physical (absorption of light), mechanical (rubbing or shearing), or chemical (reactions) mechanisms. Luminescence generated from molecules excited by ultraviolet or visible light is termed photoluminescence, which includes fluorescence and phosphorescence. The process of photoluminescence can be illustrated with the Jablonksi diagram as seen in Figure 1.14. [122] In the Jablonksi diagram, energy levels are arranged on a vertical axis. The singlet spin state S_0 is the ground state of the electrons, and S_1 and S_2 are singlet excited states. The thin horizontal lines above S_0, S_1 and S_2, represent rotational/vibrational energy levels. As a molecule absorbs photons of light, an electron is excited from the ground state to an excited state. This process occurs extremely rapidly, on the order of

10^{-15} seconds. Fluorescence is emitted when the electron decays from the first excited state (S_1) back to the ground state (S_0) on a timescale of nanoseconds. Several non-radiative transitions of electrons from a higher energy level to a lower energy level can also occur. For example, internal conversion (IC) is a non-radiative decay process that allows an electron in an excited state higher than S_1 to decay to S_1. If IC occurs between absorbance and fluorescence, the emitted light will have less energy than the absorbed light, resulting in fluorescence of longer wavelength than absorbance. This wavelength difference is called a Stokes shift (Figure.1.15). [123] Intersystem crossing (ISC) is another non-radiative process. It occurs when electrons transition between S_1 and T_1 (the first excited triplet state). Both of these two non-radiative transitions happen in nanoseconds or less in order to compete with fluorecence. If an electron transitions to T_1, phosphorescence (10^{-3} - 10^{-16} s) may occur, where the electron will decay from T_1 to S_0. Phosphorescence is a radiative phenomenon that could be interference relative to the fluorescence process, but has a decreased probability of occurring.

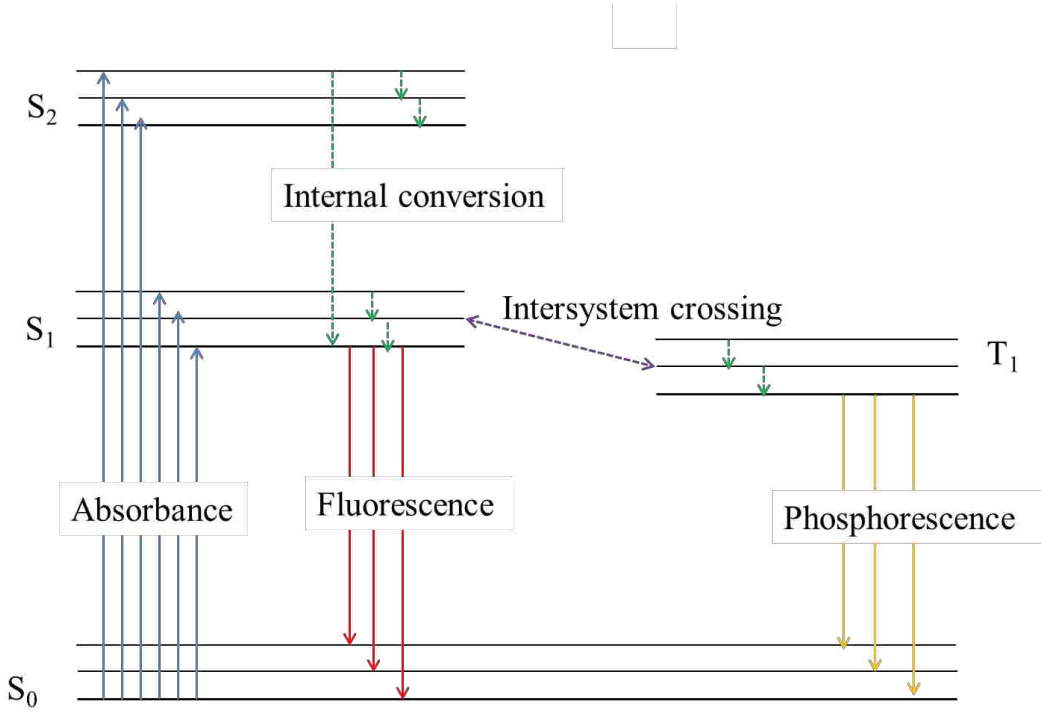

Figure 1. 14. Jablonski diagram

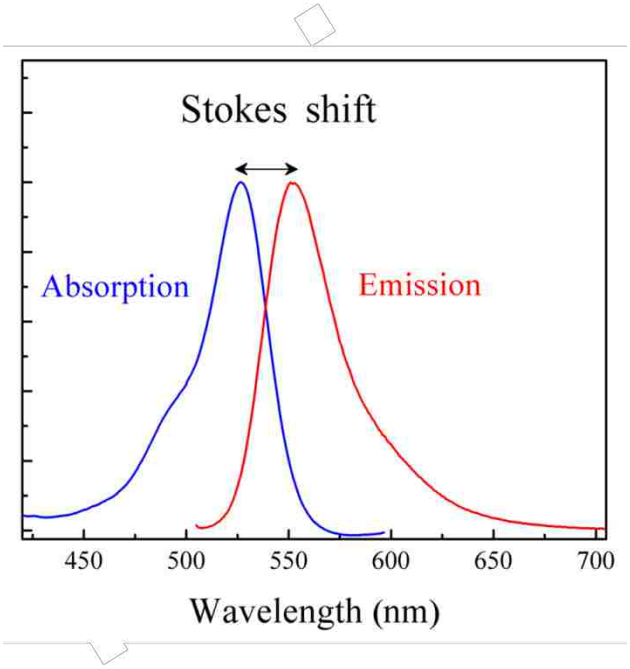

Figure 1. 15. Representative absorbance and fluorescence spectra of a compund showing a stokes shift

A graphical representation of a fluorescence spectrometer is displayed in Figure 1.16. The light from the light source (*e.g.* xenon arc lamp) reaches a monochromator, which only allows the desired excitation wavelength to pass through. The filtered light then reaches and excites the sample. In order to minimize interferences introduced by excitation light, emitted light is monitored at a 90°angle relative to excitation. Prior to reaching the detector, the emitted light passes through another monochromator (90° angle) that assists the detector in recording intensity of emitted light at each wavelength and form a spectrum.

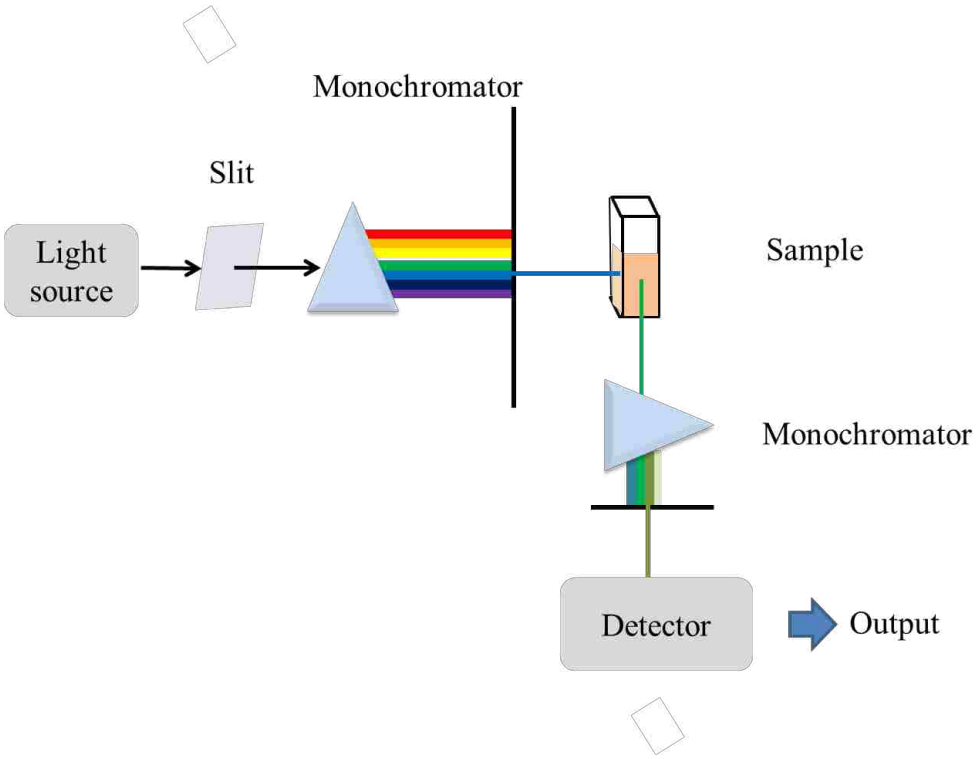

Figure 1. 16. Schematic diagram of a fluorescence spectrometer

1.5.3 Circular Dichroism Spectroscopy

Circular dichroism (CD) spectroscopy is a special type of absorption spectroscopy. The principle is based on the differential absorption of left circularly polarized light and right circularly polarized light by chiral molecules. The CD spectrometer is widely used to study chiral molecules, in particular, chiral biological molecules such as amino acids and proteins.

Optically active chiral molecules tend to absorb more of the circularly polarized light in one direction than the other direction. The difference in absorption of the circularly polarized light with two directions can be illustrated as:

$$\Delta A = A_L - A_R, \qquad (1.4)$$

where A_L is the absorbance of left-handed circularly polarized light (LCPL), A_R is the absorbance of right-handed circularly polarized light (RCPL). If we recall Beer's Law, the above equation can be written as:

$$\Delta A = (\varepsilon_L - \varepsilon_R), \qquad (1.5)$$

where ε_L is molar absorptivity for LCPL, ε_R is molar absorptivity for RCPL ($L \cdot mol^{-1} \cdot cm^{-1}$), b is path length of the cuvette (cm), and c is concentration of analyte ($mol \cdot L^{-1}$).

Generally, scientists report CD data using spectra with molar ellipticity ([θ]) as Y axis. Molar ellipticity can be calculated using such an equation:

$$[\theta] = 3298\Delta\varepsilon, \qquad (1.5)$$

where $\Delta\varepsilon$ is molar absorptivity difference ($\Delta\varepsilon=\varepsilon_L-\varepsilon_R$), [θ] is molar ellipticity (degrees·cm^2·dmol^{-1}).

A schematic diagram of a CD spectropolarimeter based on modulation techniques introduced by Grosjean and Legrand, is given in Figure 1.17.[124] The most commonly used light source of a CD spectropolarimeter is a Xenon lamp. The polychromatic light first passes through a monochromator and a linear polarizer. This generates a linearly polarized monochromatic light, which is then converted to circularly polarized light (LCPL or RCPL) by a photoelastic modulator (PEM). LCPL and RCPL pass through the sample alternately. Finally, the detector signal allows a recording of this absorbance.

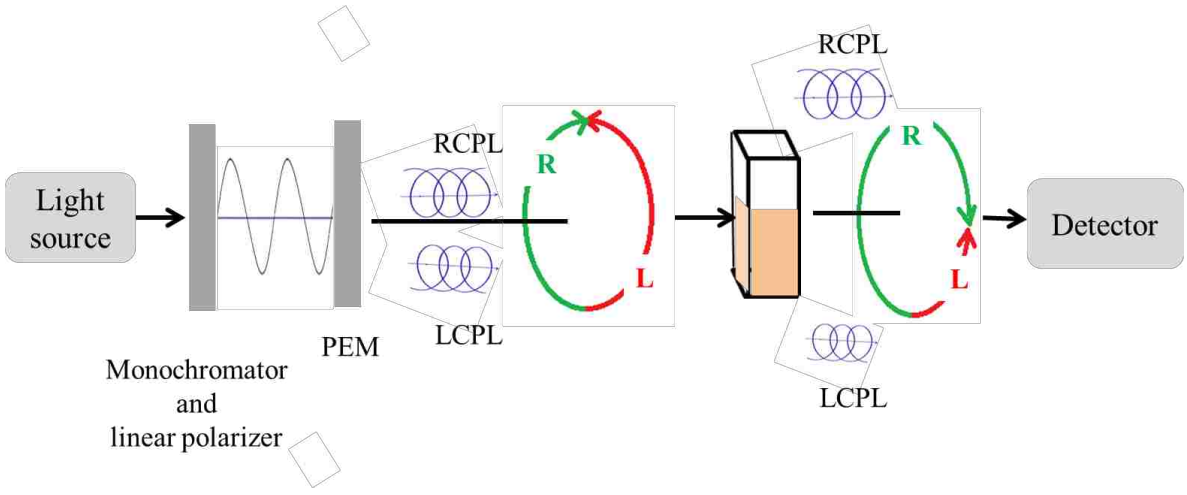

Figure 1. 17. Schematic diagram of a circular dichroism spectropolarimeter

Recently, CD has been increasingly recognized as a powerful tool for studying secondary

structure of proteins in solution. Protein secondary structure can be determined by using "far-UV" (190-250 nm) CD spectroscopy. The chromophores of interest here is the peptide bond, which absorbs light with wavelength below 240 nm. CD spectrometry gives characteristic spectral bands that are easily assigned to an alpha-helix, beta-sheet, and random coil structures (Figure 1.18). The approximate composition of each secondary structure in a protein can be calculated using the CD spectrum. [125]

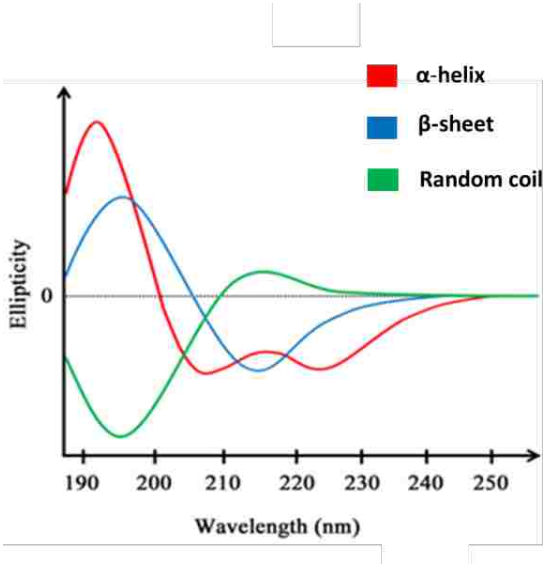

Figure 1. 18. CD spectra showing three secondary protein structures

1.5.4 Fluorescence Microscopy

Fluorescence microscopy is a special type of optical microscopy that is widely used when studying biological applications of fluorescent samples. In a fluorescence microscope, a sample is excited with light of desired wavelength. The emitted photon are then measured and visualized. A simplified schematic of the instrumental setup of a fluorescence microscope is illustrated in

Figure 1.19. The schematic is similar to that of a fluorescence spectrometer, where the device includes a light source, an excitation filter, an emission filter, and detection at a 90° angle. The use of a dichroic mirror in fluorescence microscopy is a result of the requirement of upright geometry.

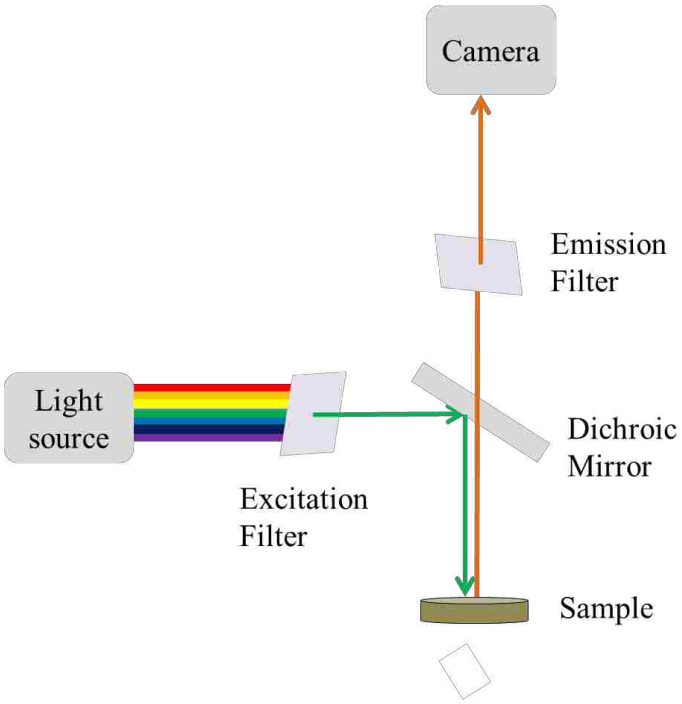

Figure 1. 19. Schematic representation of a fluorescence microscope

1.5.5 Fourier-transform Infrared Spectroscopy

Fourier Transform Infrared (FT-IR) spectroscopy is an important analytical technique that enables identification of functional groups.[126] FT-IR is a measure of the absorbance of light in the infrared region (wavelength range from 2500 to 16000 nm). Since infrared light has lower energy than UV or visible light, it does not have enough energy to promote electrons in the

ground state to the exited state. In contrast, when a compound is exposed to IR light, the resultant energy will cause the molecular bonds to vibrate. This allows for identification of characteristic stretching and bending vibration bands of certain functional groups.[127]

A graphical representation of an FT-IR spectrometer is illustrated in Figure 1.20. Briefly, light generated by the source passes through the beam-splitter and is divided into two equal beams. One beam is reflected back by a fixed mirror, while the other beam is reflected by a sliding mirror. Due to the movement of the sliding mirror, the reflected beam path is constantly changing. The two beams meet again at the beamsplitter and combine together to form a new beam, which then passes through the sample and reaches the detector. The collected signal is an interferogram which results from the interference between the two reflected beams. Figure 1.21 shows the representative light interference and an example interferogram. The detector records absorbed energy versus time for all wavelengths, simultaneously. The time-domain raw data is then transferred into a frequency-domain spectrum. This data-transfer process is called a Fourier transform. [128]

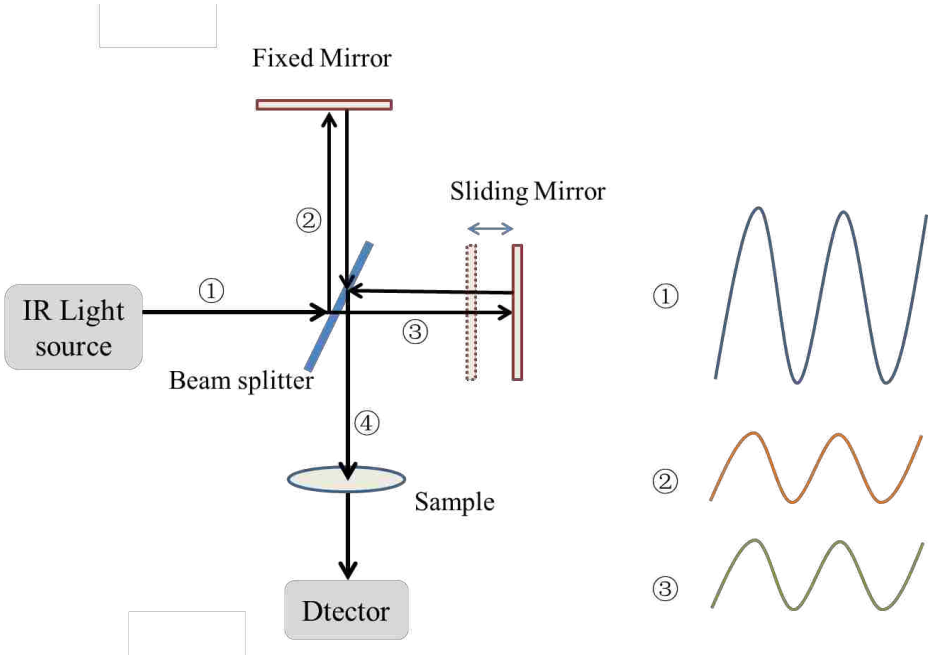

Figure 1. 20. Schematic diagram of an FT-IR sepctrometer

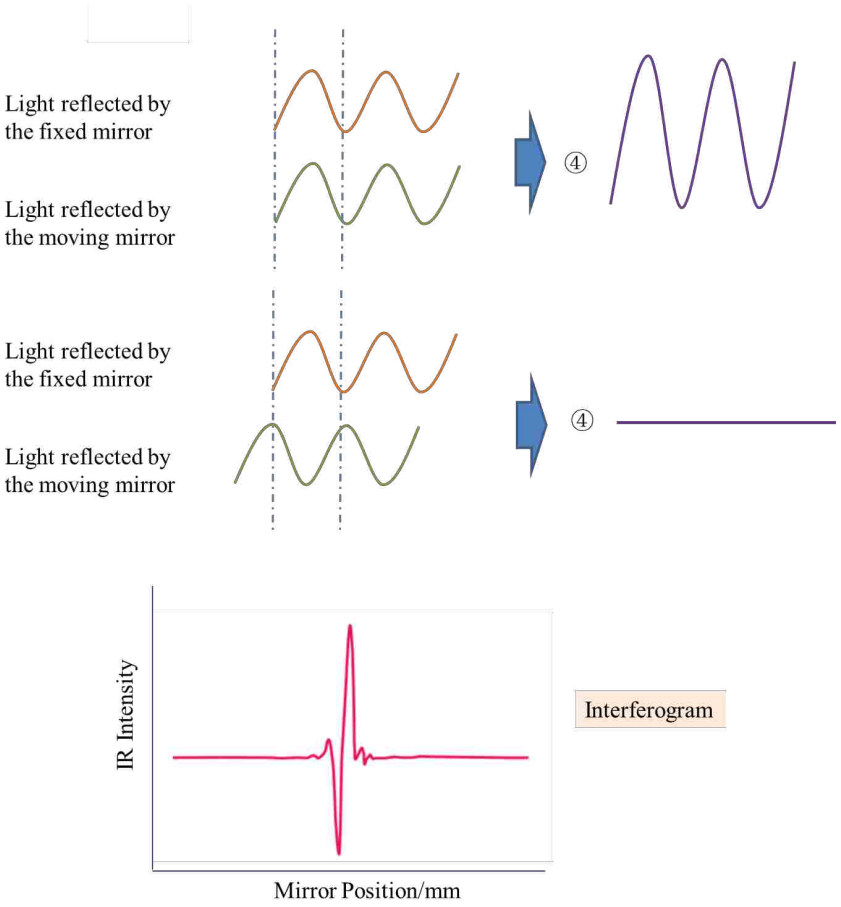

Figure 1. 21. Light interference and an example interferogram

1.5.6 Transmission Electron Microscopy

Transmission electron microscopy (TEM) is an analytical technique used to visualize the morphology of specimens in micro- and nanoscale. TEM operates under similar basic principles as an optical microscope, but TEM uses electron beam instead of photon beam. Since these high-speed electrons have wavelengths a million times shorter than that of visible light, the predicted attainable resolution of a TEM is much better than that of an optical microscope.[129] In fact, in the high resolution imaging mode, a TEM is able to reach a direct map of atomic

arrangements.[130] The working principle of a TEM is shown in Figure 1.22.

Briefly, an electron gun produces electrons with high energy and at nearly the speed of light. Theses electrons pass through a condenser system that focuses the beam onto the sample, where some of the electrons are scattered and some of the electrons transmit through the sample. The transmission of electrons depends on the thickness and density of the sample. An objective lens, movable specimen stage, and projector lenses work together to focus the transmitted electrons and form a high-quality image. The image can be directly observed with the human eye and form a photograph on the fluorescent screen or recorded by CCD (charge-coupled device) camera.[131, 132]

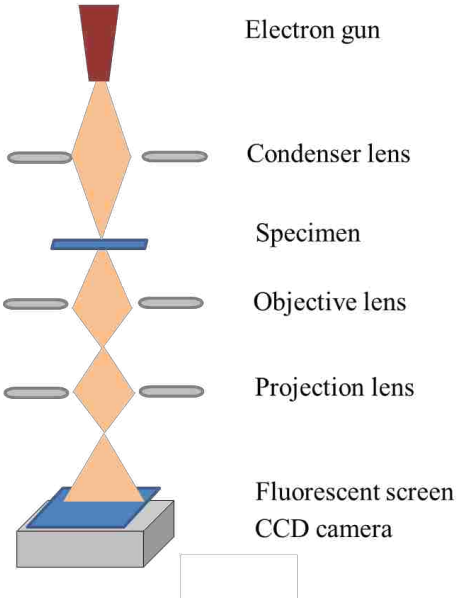

Figure 1. 22. Schematic representation of a transmission electron microscope

1.5.7 Sodium Dodecyl Sulfate Polyacrylamide Gel Electrophoresis

Sodium dodecyl sulfate polyacrylamide gel electrophoresis (SDS-PAGE) is an analytical technique widely used to separate proteins. In PAGE, charged molecules will migrate through a polyacrylamide gel in an electric field with different rate. The migrating rate of a molecule in a given gel and electric field depends on both charge and size. Due to the complicated secondary, tertiary and quaternary structure of protein, the migrating rate in PAGE conditions is not able to determine their molecular weight. In this regard, protein samples are first treated with SDS and 2-mercaptoethanol to eliminate the tridimensional structure (quaternary and tertiary structures). In this treatment, 2-mercaptoethanol breaks the disulfide bonds, [133] while the hydrophobic side of SDS binds the protein interior hydrophobic groups. [134] This results in a linear peptide chain, which is uniformly coated with negatively charged molecules (~1.4 g SDS/g protein). By doing so, the migration rate of these peptide chains depends primarily on the molecular weight. Diagrams of SDS amphipathic structure and protein pretreatment are illustrated in Figure 1.23 and Figure 1.24, respectively.

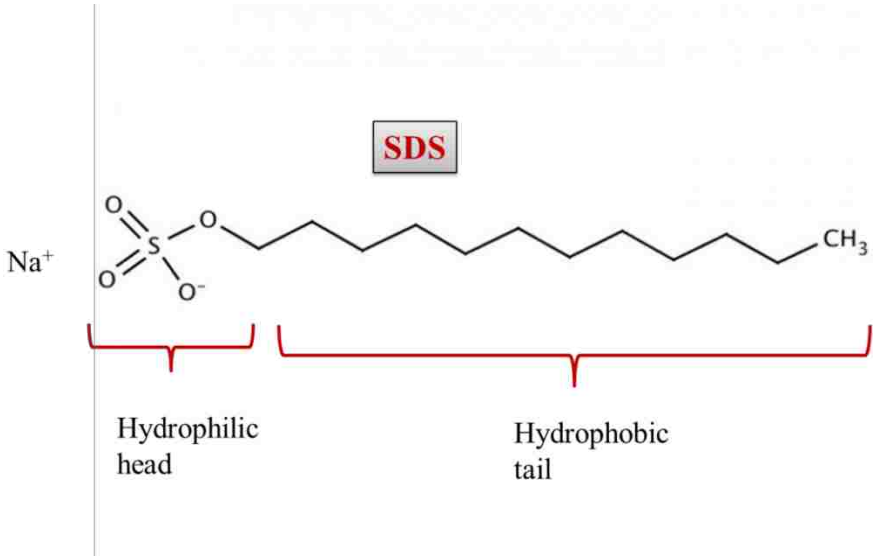

Figure 1. 23. Amphipathic structure of sodium dodecyl sulfate

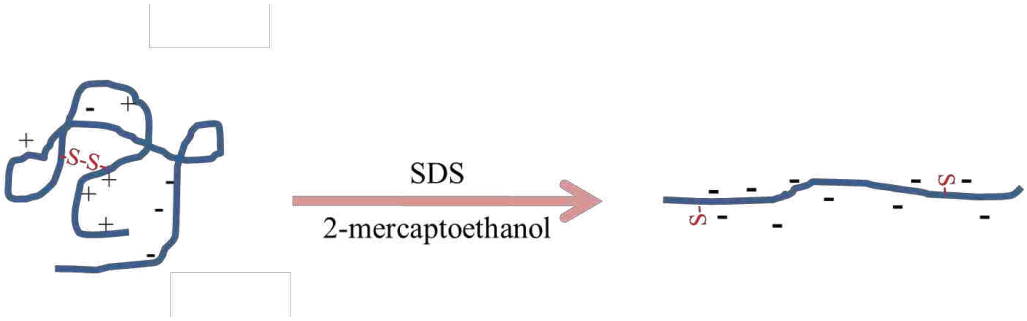

Figure 1. 24. Protein pretreatment with SDS and 2-mercaptoethanol

A schematic diagram of SDS-PAGE principle, based on Laemmli system, [135] is shown in Figure 1.25. Polyacrylamide gels are prepared by acrylamide polymerization and N,N'-methylenebisacrylamide cross linking (Figure 1.26). The gel is discontinuous, and consists of a stacking gel and a running gel. Chloride is the mobile anion in the gels, while in the upper and lower tank buffers, glycine is the mobile anion. Pretreated protein samples are loaded into wells in the stacking gel. When an electric field is applied, proteins migrate through the gel

toward the anode, which is at the bottom of the system. Proteins are sufficiently separated by size with smaller proteins migrate faster toward the anode.

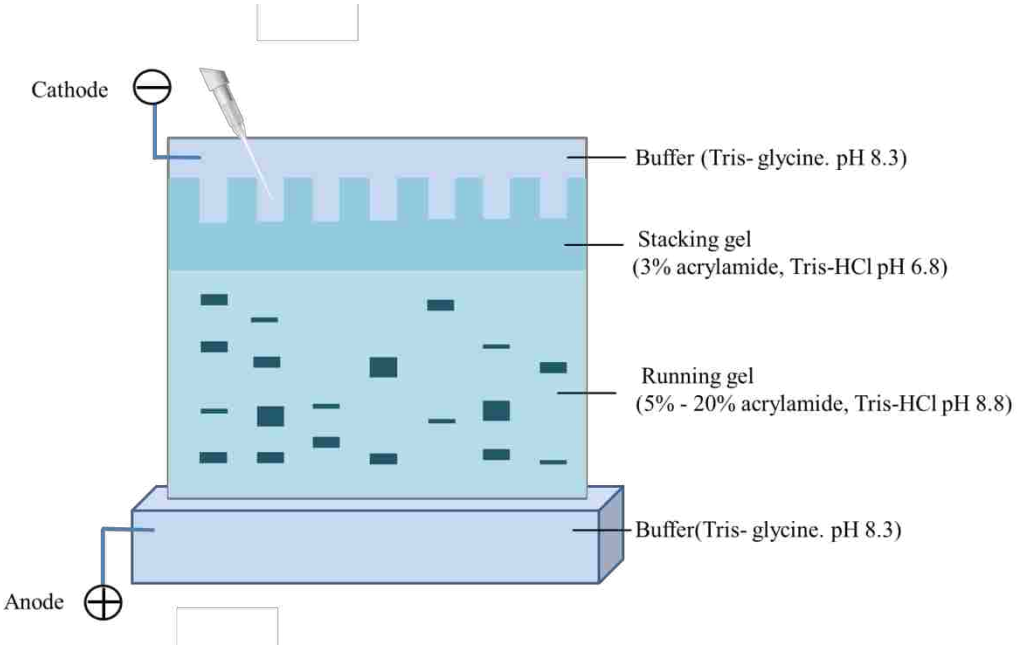

Figure 1. 25. PAGE working principal

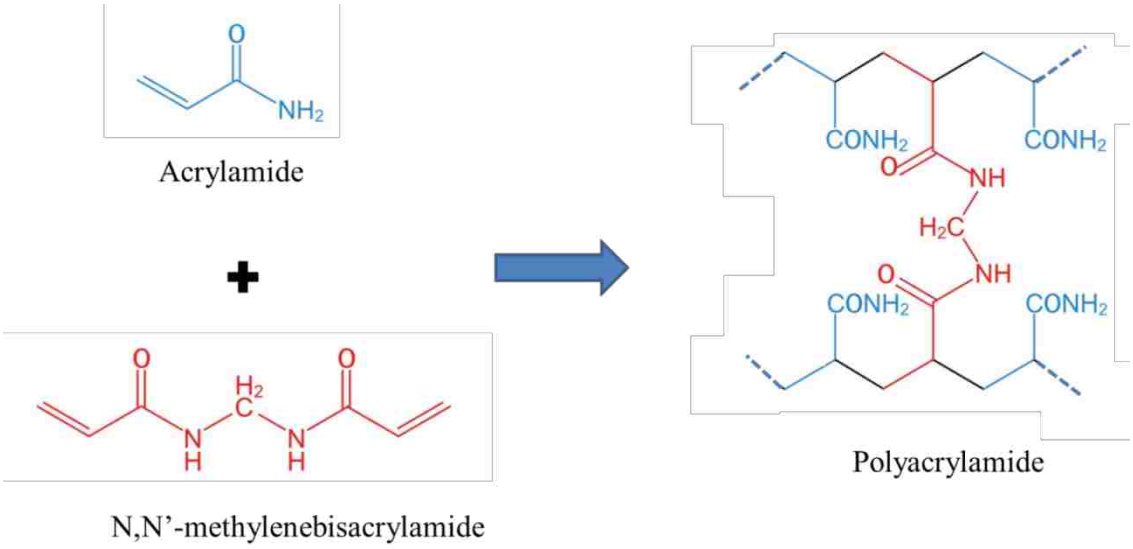

Figure 1. 26. The preparation of polyacrylamide gels

1.5.8 Principal Component Analysis and Linear Discriminant Analysis

Both principal component analysis (PCA) and linear discriminant analysis (LDA) are statistical techniques that commonly used for dimensionality reduction. PCA was first reported in 1901 by Karl Pearson; [136] and now is mostly used as a technique for making predictive models. The goal of using PCA is to transform several correlated variables into a smaller number of uncorrelated variables (principal components); these principal components will maximize the variance in a dataset. [137-139] The first principal component gives information from as much of the variability in the data as possible, and the following components accounts for as much of the remaining information as possible. [140, 141] Most often, the first few principal components are able to represent the most useful information of a dataset. For example, if we want to visualize a multivariate dataset using each variable as an axis, a high-dimensional data space is needed. With the help of statistical software, such as SAS (Statistical Analysis System) and R, principal components can be generated from the raw data. By using only the first two or three principal components, the dimensionality of the data is reduced.

While PCA is "unsupervised", in that it ignores class labels, LDA is a "supervised" technique and computes the linear discrimination factors that maximize the separation between multiple classes. [142, 143] Figure 1.27 presents a simple conceptual scheme of PCA and LDA methods.

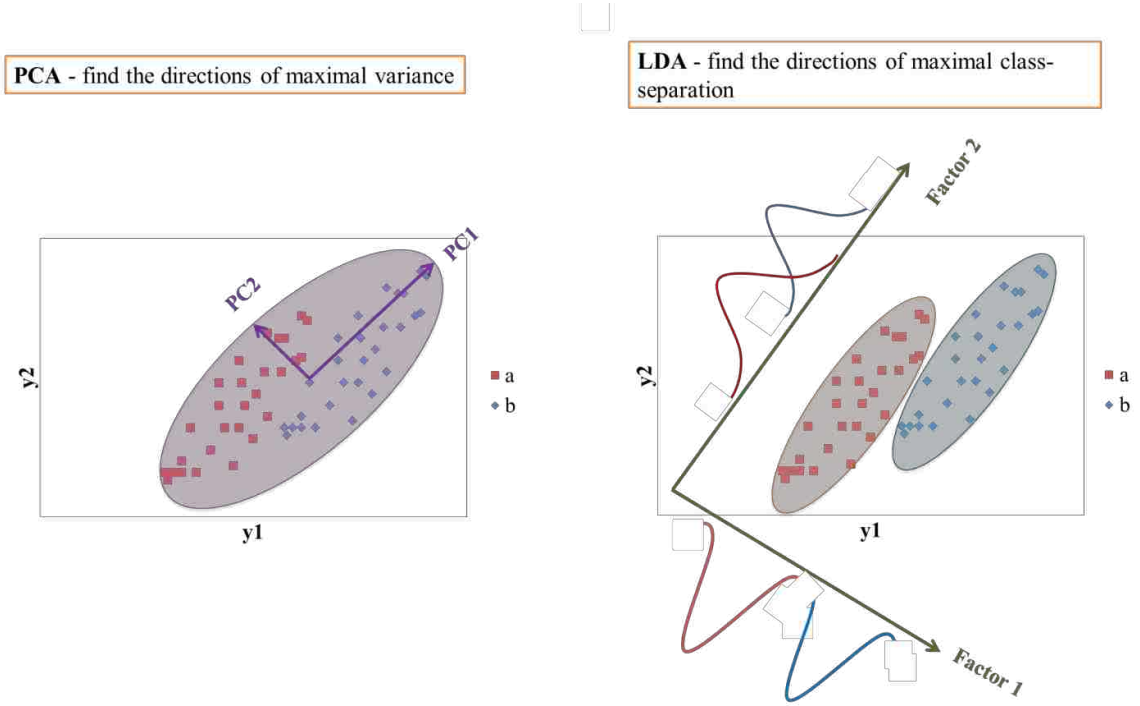

Figure 1. 27. Conceptual scheme of PCA and LDA methods

In this thesis, PCA and LDA were used to analyze data generated by sensor arrays and facilitate identification and classification of analytes. A method combining PCA and LDA was used here. In this method, the first few principal components created by PCA were used as input variables for LDA. This PCA-plus-LDA method has been verified as effective, and capable of addressing computational difficulties caused by high-dimensionality and helps to avoid over-fitting. [144-147]

1.6 Overview of the Dissertation

The work presented in this dissertation is based on the development of task-specific organic salts for sensing and protein separation. In Chapter 2, a sensitive and selective ratiometric

fluorescent nanodiamond probe was developed for detection of hydroxyl radicals. These materials were based on the use of GUMBOS that were derived from 1,1'-diethyl-2,2'-cyanine (PIC) iodide and 1,1'-diethyl-2,2'-carbocyanine (PC) iodide. Each GUMBOS compound exhibited different reactivity towards reactive oxygen species. Without the use of any organic linkage, the two GUMBOS were combined to provide a ratiometric fluorescence sensing profile. The cyanine based ratiometric nanoprobe exhibited high selectivity toward hydroxyl radicals in comparison to other reactive species, such as superoxide anion ($O_2^{\bullet-}$), singlet oxygen ($^1O_2$), hydrogen peroxide (H_2O_2), and peroxynitrite ($ONOO^-$). In addition, in vitro detection of hydroxyl radical was successfully demonstrated by use of the binary nanoGUMBOS using hormone-independent human breast adenocarcinoma cells (MDA-MB-231).

In Chapter 3, an imidazolium-dysprosium-based nanoGUMBOS was prepared using a facile method. This nanomaterial served as a magnetic nanoadsorbent for selective hemoglobin isolation. The imidazolium cation was introduced as the selective hemoglobin affinity group, with a dysprosium element possessing the paramagnetic property as the anion. These nanoGUMBOS exhibited high adsorption capacity and good selectivity toward hemoglobin. In addition, they were successfully applied in the selective Hb isolation from human whole blood.

In Chapter 4, a cyanine-based fluorescent sensor array was studied for discrimination of serum proteins. The physicochemical properties of the sensor array components were tuned through variation of the counter-ions. Three cyanine cations and two hydrophobic anions were

used to fabricate GUMBOS sensors in this study. The resulting six sensor elements respond differently to seven proteins. By following with a pattern recognition system, this sensor array was able to discriminate protein mixtures at different concentration levels.

1.7 References

1. Welton T. Room-temperature ionic liquids. Solvents for synthesis and catalysis. *Chemical reviews.* 1999;99(8):2071-2084.

2. Pandey S. Analytical applications of room-temperature ionic liquids: A review of recent efforts. *Analytica Chimica Acta.* 2006;556(1):38-45.

3. Seddon KR. Ionic liquids: a taste of the future. *Nature materials.* 2003;2(6):363.

4. Walden P. Ueber die Molekulargrösse und elektrische Leitfähigkeit einiger geschmolzenen Salze. *Известия Российской академии наук Серия математическая.* 1914;8(6):405-422.

5. Wilkes JS. A short history of ionic liquids—from molten salts to neoteric solvents. *Green Chemistry.* 2002;4(2):73-80.

6. Hurley FH, WIer TP. The electrodeposition of aluminum from nonaqueous solutions at room temperature. *Journal of the Electrochemical Society.* 1951;98(5):207-212.

7. Chum HL, Koch V, Miller L, Osteryoung R. Electrochemical scrutiny of organometallic iron complexes and hexamethylbenzene in a room temperature molten salt. *Journal of the American Chemical Society.* 1975;97(11):3264-3265.

8. Wilkes JS, Levisky JA, Wilson RA, Hussey CL. Dialkylimidazolium chloroaluminate melts: a new class of room-temperature ionic liquids for electrochemistry, spectroscopy and synthesis. *Inorganic Chemistry.* 1982;21(3):1263-1264.

9. Scheffler TB, Hussey CL, Seddon KR, Kear CM, Armitage PD. Molybdenum chloro complexes in room-temperature chloroaluminate ionic liquids: stabilization of hexachloromolybdate (2-) and hexachloromolybdate (3-). *Inorganic Chemistry.*

1983;22(15):2099-2100.

10. Scheffler TB, Hussey CL. Electrochemical study of tungsten chloro complex chemistry in the basic aluminum chloride-1-methyl-3-ethylimidazolium chloride ionic liquid. *Inorganic Chemistry.* 1984;23(13):1926-1932.

11. Sun IW, Ward EH, Hussey CL, Seddon KR, Turp JE. Electrochemistry and spectroelectrochemistry of the hexachloroiridate (III) and-(IV) complexes in the basic aluminum chloride-1-methyl-3-ethylimidazolium chloride room-temperature ionic liquid. *Inorganic Chemistry.* 1987;26(13):2140-2143.

12. Wilkes JS, Zaworotko MJ. Air and water stable 1-ethyl-3-methylimidazolium based ionic liquids. *Journal of the Chemical Society, Chemical Communications.* 1992(13):965-967.

13. Egorova KS, Ananikov VP. Toxicity of Ionic Liquids: Eco (cyto) activity as Complicated, but Unavoidable Parameter for Task‐Specific Optimization. *ChemSusChem.* 2014;7(2):336-360.

14. Visser AE, Swatloski RP, Reichert WM, et al. Task-specific ionic liquids for the extraction of metal ions from aqueous solutions. *Chemical Communications.* 2001(1):135-136.

15. Hayashi S, Hamaguchi H-o. Discovery of a magnetic ionic liquid [bmim] FeCl4. *Chemistry Letters.* 2004;33(12):1590-1591.

16. Okuno M, Hamaguchi H-o, Hayashi S. Magnetic manipulation of materials in a magnetic ionic liquid. *Applied physics letters.* 2006;89(13):132506.

17. Lin B, Cheng S, Qiu L, Yan F, Shang S, Lu J. Protic ionic liquid-based hybrid proton-conducting membranes for anhydrous proton exchange membrane application. *Chemistry of materials.* 2010;22(5):1807-1813.

18. Greaves TL, Drummond CJ. Protic ionic liquids: properties and applications. *Chemical reviews.* 2008;108(1):206-237.

19. Angell CA, Byrne N, Belieres J-P. Parallel developments in aprotic and protic ionic liquids: Physical chemistry and applications. *Accounts of chemical research.* 2007;40(11):1228-1236.

20. Ni B, Zhang Q, Headley AD. Functionalized chiral ionic liquid as recyclable organocatalyst for asymmetric Michael addition to nitrostyrenes. *Green Chemistry.* 2007;9(7):737-739.

21. Wasserscheid P, Keim W, Bolm C, Bösmann A. Chiral ionic liquids. Google Patents; 2005.

22. Ding J, Armstrong DW. Chiral ionic liquids: synthesis and applications. *Chirality.* 2005;17(5):281-292.

23. Pitula S. *Luminescent Ionic Liquids*, Universität zu Köln; 2009.

24. Nunez NO, Ocana M. An ionic liquid based synthesis method for uniform luminescent lanthanide fluoride nanoparticles. *Nanotechnology.* 2007;18(45):455606.

25. Costa RD, Orti E, Bolink HJ, Monti F, Accorsi G, Armaroli N. Luminescent Ionic Transition‐Metal Complexes for Light‐Emitting Electrochemical Cells. *Angewandte Chemie International Edition.* 2012;51(33):8178-8211.

26. Ohno H, Yoshizawa M. Ion conductive characteristics of ionic liquids prepared by neutralization of alkylimidazoles. *Solid State Ionics.* 2002;154:303-309.

27. Ohno H, Yoshizawa M, Ogihara W. Development of new class of ion conductive polymers based on ionic liquids. *Electrochimica Acta.* 2004;50(2-3):255-261.

28. Ohno H. Design of ion conductive polymers based on ionic liquids. Paper presented at: Macromolecular Symposia, 2007.

29. Welton T. Ionic liquids in catalysis. *Coordination chemistry reviews.* 2004;248(21-24):2459-2477.

30. Mehnert CP. Supported ionic liquid catalysis. *Chemistry-A European Journal.* 2005;11(1):50-56.

31. Liquids R-TI. Solvents for Synthesis and Catalysis Welton, Thomas. *Chemical Reviews (Washington, DC).* 1999;99(8):2071-2083.

32. Cull S, Holbrey J, Vargas‐Mora V, Seddon K, Lye G. Room‐temperature ionic liquids as replacements for organic solvents in multiphase bioprocess operations. *Biotechnology*

and bioengineering. 2000;69(2):227-233.

33. Huddleston JG, Willauer HD, Swatloski RP, Visser AE, Rogers RD. Room temperature ionic liquids as novel media for 'clean'liquid–liquid extraction. *Chemical Communications.* 1998(16):1765-1766.

34. Dai S, Ju Y, Barnes C. Solvent extraction of strontium nitrate by a crown ether using room-temperature ionic liquids. *Journal of the Chemical Society, Dalton Transactions.* 1999(8):1201-1202.

35. Wei D, Ivaska A. Applications of ionic liquids in electrochemical sensors. *Analytica Chimica Acta.* 2008;607(2):126-135.

36. Ji Q, Honma I, Paek SM, et al. Layer‐by‐layer films of graphene and ionic liquids for highly selective gas sensing. *Angewandte Chemie International Edition.* 2010;49(50):9737-9739.

37. Shiddiky MJ, Torriero AA. Application of ionic liquids in electrochemical sensing systems. *Biosensors and Bioelectronics.* 2011;26(5):1775-1787.

38. Armand M, Endres F, MacFarlane DR, Ohno H, Scrosati B. Ionic-liquid materials for the electrochemical challenges of the future. *Nature materials.* 2009;8(8):621.

39. Antonietti M, Kuang D, Smarsly B, Zhou Y. Ionic liquids for the convenient synthesis of functional nanoparticles and other inorganic nanostructures. *Angewandte Chemie International Edition.* 2004;43(38):4988-4992.

40. Watanabe M, Thomas ML, Zhang S, Ueno K, Yasuda T, Dokko K. Application of ionic liquids to energy storage and conversion materials and devices. *Chemical reviews.* 2017;117(10):7190-7239.

41. Rutten FJ, Tadesse H, Licence P. Rewritable imaging on the surface of frozen ionic liquids. *Angewandte Chemie International Edition.* 2007;46(22):4163-4165.

42. Mohmeyer N, Kuang D, Wang P, Schmidt H-W, Zakeeruddin SM, Grätzel M. An efficient organogelator for ionic liquids to prepare stable quasi-solid-state dye-sensitized solar cells. *Journal of Materials Chemistry.* 2006;16(29):2978-2983.

43. Tesfai A, El-Zahab B, Bwambok DK, et al. Controllable formation of ionic liquid

micro-and nanoparticles via a melt–emulsion–quench approach. *Nano letters.* 2008;8(3):897-901.

44. Warner IM, El-Zahab B, Siraj N. Perspectives on moving ionic liquid chemistry into the solid phase. *Analytical chemistry.* 2014;86(15):7184-7191.

45. Tesfai A, El-Zahab B, Kelley AT, et al. Magnetic and nonmagnetic nanoparticles from a group of uniform materials based on organic salts. *Acs Nano.* 2009;3(10):3244-3250.

46. de Rooy SL, Das S, Li M, et al. Ionically self-Assembled, multi-luminophore one-dimensional micro-and nanoscale aggregates of thiacarbocyanine GUMBOS. *The Journal of Physical Chemistry C.* 2012;116(14):8251-8260.

47. Cong M, Siraj N, Bhattarai N, et al. Ratiometric fluorescence detection of hydroxyl radical using cyanine-based binary nanoGUMBOS. *Sensors and Actuators B: Chemical.* 2018;257:993-1000.

48. Li M, Ganea GM, Lu C, et al. Lipophilic phosphonium–lanthanide compounds with magnetic, luminescent, and tumor targeting properties. *Journal of inorganic biochemistry.* 2012;107(1):40-46.

49. Magut PK, Das S, Fernand VE, et al. Tunable cytotoxicity of rhodamine 6G via anion variations. *Journal of the American Chemical Society.* 2013;135(42):15873-15879.

50. Brust M, Walker M, Bethell D, Schiffrin DJ, Whyman R. Synthesis of thiol-derivatised gold nanoparticles in a two-phase liquid–liquid system. *Journal of the Chemical Society, Chemical Communications.* 1994(7):801-802.

51. Salata OV. Applications of nanoparticles in biology and medicine. *Journal of nanobiotechnology.* 2004;2(1):3.

52. Gelperina S, Kisich K, Iseman MD, Heifets L. The potential advantages of nanoparticle drug delivery systems in chemotherapy of tuberculosis. *American journal of respiratory and critical care medicine.* 2005;172(12):1487-1490.

53. Singh R, Lillard Jr JW. Nanoparticle-based targeted drug delivery. *Experimental and molecular pathology.* 2009;86(3):215-223.

54. Chol S, Estman J. Enhancing thermal conductivity of fluids with nanoparticles.

ASME-Publications-Fed. 1995;231:99-106.

55. Shekibi Y, Gray-Weale A, MacFarlane DR, Hill AJ, Forsyth M. Nanoparticle enhanced conductivity in organic ionic plastic crystals: space charge versus strain induced defect Mechanism. *The Journal of Physical Chemistry C.* 2007;111(30):11463-11468.

56. Wessells CD, McDowell MT, Peddada SV, Pasta M, Huggins RA, Cui Y. Tunable reaction potentials in open framework nanoparticle battery electrodes for grid-scale energy storage. *Acs Nano.* 2012;6(2):1688-1694.

57. Sun J, Zheng G, Lee H-W, et al. Formation of stable phosphorus–carbon bond for enhanced performance in black phosphorus nanoparticle–graphite composite battery anodes. *Nano letters.* 2014;14(8):4573-4580.

58. Song J, Bazant MZ. Effects of nanoparticle geometry and size distribution on diffusion impedance of battery electrodes. *Journal of The Electrochemical Society.* 2013;160(1):A15-A24.

59. Corot C, Robert P, Idée J-M, Port M. Recent advances in iron oxide nanocrystal technology for medical imaging. *Advanced drug delivery reviews.* 2006;58(14):1471-1504.

60. Fang C, Zhang M. Multifunctional magnetic nanoparticles for medical imaging applications. *Journal of materials chemistry.* 2009;19(35):6258-6266.

61. Cormode DP, Jarzyna PA, Mulder WJ, Fayad ZA. Modified natural nanoparticles as contrast agents for medical imaging. *Advanced drug delivery reviews.* 2010;62(3):329-338.

62. Nath N, Chilkoti A. A colorimetric gold nanoparticle sensor to interrogate biomolecular interactions in real time on a surface. *Analytical chemistry.* 2002;74(3):504-509.

63. Ai K, Zhang B, Lu L. Europium‐based fluorescence nanoparticle sensor for rapid and ultrasensitive detection of an anthrax biomarker. *Angewandte Chemie.* 2009;121(2):310-314.

64. Mickelson W, Sussman A, Zettl A. Low-power, fast, selective nanoparticle-based hydrogen sulfide gas sensor. *Applied Physics Letters.* 2012;100(17):173110.

65. El-Sayed IH, Huang X, El-Sayed MA. Selective laser photo-thermal therapy of epithelial carcinoma using anti-EGFR antibody conjugated gold nanoparticles. *Cancer letters.* 2006;239(1):129-135.

66. Visaria RK, Griffin RJ, Williams BW, et al. Enhancement of tumor thermal therapy using gold nanoparticle–assisted tumor necrosis factor-α delivery. *Molecular cancer therapeutics.* 2006;5(4):1014-1020.

67. O'Neal DP, Hirsch LR, Halas NJ, Payne JD, West JL. Photo-thermal tumor ablation in mice using near infrared-absorbing nanoparticles. *Cancer letters.* 2004;209(2):171-176.

68. Ferrari M. Cancer nanotechnology: opportunities and challenges. *Nature Reviews Cancer.* 2005;5(3):161-171.

69. Bwambok DK, El-Zahab B, Challa SK, et al. Near-infrared fluorescent nanoGUMBOS for biomedical imaging. *Acs Nano.* 2009;3(12):3854-3860.

70. Jordan AN, Das S, Siraj N, et al. Anion-controlled morphologies and spectral features of cyanine-based nanoGUMBOS–an improved photosensitizer. *Nanoscale.* 2012;4(16):5031-5038.

71. Bhattarai N, Chen M, Pérez RL, et al. Enhanced chemotherapeutic toxicity of cyclodextrin templated size-tunable rhodamine 6G nanoGUMBOS. *Journal of Materials Chemistry B.* 2018.

72. Karam TE, Siraj N, Zhang Z, Ezzir AF, Warner IM, Haber LH. Ultrafast and nonlinear spectroscopy of brilliant green-based nanoGUMBOS with enhanced near-infrared emission. *The Journal of Chemical Physics.* 2017;147(14):144701.

73. Sarkar A, Kanakamedala K, Jagadish NN, et al. Electro-optical characterization of cyanine-based GUMBOS and nanoGUMBOS. *Electronic Materials Letters.* 2014;10(5):879-885.

74. Jordan AN, Siraj N, Das S, Warner IM. Tunable near-infrared emission of binary nano-and mesoscale GUMBOS. *RSC Advances.* 2014;4(54):28471-28480.

75. Sarkar A, Kanakamedala K, Rajathadripura M, et al. Electro-optical characterization of nanoGUMBOS. *Electronic Materials Letters.* 2014;10(4):775-781.

76. Dumke JC, El-Zahab B, Challa S, et al. Lanthanide-based luminescent nanoGUMBOS. *Langmuir.* 2010;26(19):15599-15603.

77. Kolic PE, Siraj N, Hamdan S, Regmi BP, Warner IM. Synthesis and Characterization of Porphyrin-Based GUMBOS and NanoGUMBOS as Improved Photosensitizers. *The Journal of Physical Chemistry C.* 2016;120(9):5155-5163.

78. Galpothdeniya WIS, Fronczek FR, Cong M, Bhattarai N, Siraj N, Warner IM. Tunable GUMBOS-based sensor array for label-free detection and discrimination of proteins. *Journal of Materials Chemistry B.* 2016;4(8):1414-1422.

79. Bhattarai N. Chemotherapeutic Applications of Rhodamine Based NanoGUMBOS. 2018.

80. Dumke JC, Qureshi A, Hamdan S, et al. In vitro activity studies of hyperthermal near-infrared nanoGUMBOS in MDA-MB-231 breast cancer cells. *Photochemical & Photobiological Sciences.* 2014;13(9):1270-1280.

81. Wright A, Li M, Ravula S, et al. Soft-and hard-templated organic salt nanoparticles with the Midas touch: gold-shelled nanoGUMBOS. *Journal of Materials Chemistry C.* 2014;2(42):8996-9003.

82. Harruff BA, Bunker CE. Spectral properties of AOT-protected CdS nanoparticles: quantum yield enhancement by photolysis. *Langmuir.* 2003;19(3):893-897.

83. Eastoe J, Gold S, Rogers SE, et al. Ionic liquid-in-oil microemulsions. *Journal of the American Chemical Society.* 2005;127(20):7302-7303.

84. Janata J, Josowicz M, Vanýsek P, DeVaney DM. Chemical sensors. *Analytical Chemistry.* 1998;70(12):179-208.

85. Hulanicki A, Glab S, Ingman F. Chemical sensors: definitions and classification. *Pure and Applied Chemistry.* 1991;63(9):1247-1250.

86. Banica F-G. *Chemical sensors and biosensors: fundamentals and applications*: John Wiley & Sons; 2012.

87. Wang J, Liu G, Jan MR. Ultrasensitive electrical biosensing of proteins and DNA: carbon-nanotube derived amplification of the recognition and transduction events. *Journal of the American Chemical Society.* 2004;126(10):3010-3011.

88. Spichiger-Keller UE. *Chemical sensors and biosensors for medical and biological applications*: John Wiley & Sons; 2008.

89. Gardner JW, Bartlett PN. A brief history of electronic noses. *Sensors and Actuators B: Chemical.* 1994;18(1-3):210-211.

90. Arshak K, Moore E, Lyons G, Harris J, Clifford S. A review of gas sensors employed in electronic nose applications. *Sensor review.* 2004;24(2):181-198.

91. Firestein S. How the olfactory system makes sense of scents. *Nature.* 2001;413(6852):211.

92. Mombaerts P. Genes and ligands for odorant, vomeronasal and taste receptors. *Nature Reviews Neuroscience.* 2004;5(4):263.

93. Malnic B, Hirono J, Sato T, Buck LB. Combinatorial receptor codes for odors. *Cell.* 1999;96(5):713-723.

94. Axel R. The molecular logic of smell. *Scientific American.* 1995;273(4):154-159.

95. Breer H, Wanner I, Strotmann J. Molecular genetics of mammalian olfaction. *Behavior genetics.* 1996;26(3):209-219.

96. Bowers WD, Bahrami F, Tran J. Chemical sensor array. Google Patents; 2001.

97. Jurs PC, Bakken G, McClelland H. Computational methods for the analysis of chemical sensor array data from volatile analytes. *Chemical Reviews.* 2000;100(7):2649-2678.

98. Shaffer RE, Rose-Pehrsson SL, McGill RA. A comparison study of chemical sensor array pattern recognition algorithms. *Analytica Chimica Acta.* 1999;384(3):305-317.

99. Lin H, Jang M, Suslick KS. Preoxidation for colorimetric sensor array detection of VOCs. *Journal of the American Chemical Society.* 2011;133(42):16786-16789.

100. Rakow NA, Suslick KS. A colorimetric sensor array for odour visualization. *Nature.* 2000;406(6797):710.

101. Zheng G, Patolsky F, Cui Y, Wang WU, Lieber CM. Multiplexed electrical detection of cancer markers with nanowire sensor arrays. *Nature biotechnology.* 2005;23(10):1294.

102. Petsko GA, Ringe D. *Protein structure and function*: New Science Press; 2004.

103. Cooper GM, Hausman RE. *The cell: Molecular approach*: Medicinska naklada; 2004.

104. Russell RB, Barton GJ. Multiple protein sequence alignment from tertiary structure comparison: assignment of global and residue confidence levels. *Proteins: Structure, Function, and Bioinformatics.* 1992;14(2):309-323.

105. Tennikova T, Bleha M, Švec F, Almazova T, Belenkii B. High-performance membrane chromatography of proteins, a novel method of protein separation. *Journal of Chromatography A.* 1991;555(1-2):97-107.

106. Fausnaugh J, Kennedy L, Regnier F. Comparison of hydrophobic-interaction and reversed-phase chromatography of proteins. *Journal of Chromatography A.* 1984;317:141-155.

107. Lemmo AV, Jorgenson JW. Two-dimensional protein separation by microcolumn size-exclusion chromatography-capillary zone electrophoresis. *Journal of Chromatography A.* 1993;633(1-2):213-220.

108. Stathopulos PB, Scholz GA, Hwang YM, Rumfeldt JA, Lepock JR, Meiering EM. Sonication of proteins causes formation of aggregates that resemble amyloid. *Protein Science.* 2004;13(11):3017-3027.

109. Andrews NC, Faller DV. A rapid micropreparation technique for extraction of DNA-binding proteins from limiting numbers of mammalian cells. *Nucleic acids research.* 1991;19(9):2499.

110. Singh N, Donovan G, Batey I, MacRitchie F. Use of sonication and size-exclusion high-performance liquid chromatography in the study of wheat flour proteins. I. Dissolution of total proteins in the absence of reducing agents. *Cereal Chem.* 1990;67(2):150-161.

111. Ünlü M, Morgan ME, Minden JS. Difference gel electrophoresis. A single gel method for detecting changes in protein extracts. *Electrophoresis.* 1997;18(11):2071-2077.

112. Hames BD. *Gel electrophoresis of proteins: a practical approach.* Vol 197: OUP Oxford; 1998.

113. Yeh M-K, Coombes A, Jenkins P, Davis S. A novel emulsification-solvent extraction technique for production of protein loaded biodegradable microparticles for vaccine and drug delivery. *Journal of Controlled Release.* 1995;33(3):437-445.

114. Want EJ, O'Maille G, Smith CA, et al. Solvent-dependent metabolite distribution, clustering, and protein extraction for serum profiling with mass spectrometry. *Analytical chemistry.* 2006;78(3):743-752.

115. Pei Y, Wang J, Wu K, Xuan X, Lu X. Ionic liquid-based aqueous two-phase extraction of selected proteins. *Separation and Purification Technology.* 2009;64(3):288-295.

116. Tian Y, Zhou Y, Elliott S, Aebersold R, Zhang H. Solid-phase extraction of N-linked glycopeptides. *Nature protocols.* 2007;2(2):334.

117. Figeys D, Ducret A, Aebersold R. Identification of proteins by capillary electrophoresis-tandem mass spectrometry evaluation of an on-line solid-phase extraction device. *Journal of Chromatography A.* 1997;763(1-2):295-306.

118. Figeys D, Ducret A, Yates III JR, Aebersold R. Protein identification by solid phase microextraction—capillary zone electrophoresis—microelectrospray—tandem mass spectrometry. *Nature biotechnology.* 1996;14(11):1579.

119. Hajizadeh S, Kettisen K, Gram M, Bülow L, Ye L. Composite imprinted macroporous hydrogels for haemoglobin purification from cell homogenate. *Journal of Chromatography A.* 2018;1534:22-31.

120. Chang TMS. Hemoglobin‐based red blood cell substitutes. *Artificial organs.* 2004;28(9):789-794.

121. Burtis CA, Bruns DE. *Tietz Fundamentals of Clinical Chemistry and Molecular Diagnostics-E-Book*: Elsevier Health Sciences; 2014.

122. Guilbault GG. *Practical fluorescence.* Vol 3: CRC Press; 1990.

123. Hermann A. Luminescent solar concentrators—a review. *Solar Energy.* 1982;29(4):323-329.

124. Velluz L, Legrand M, Grosjean M. *Optical circular dichroism*: Academic Press; 1965.

125. Kelly SM, Jess TJ, Price NC. How to study proteins by circular dichroism. *Biochimica et Biophysica Acta (BBA)-Proteins and Proteomics.* 2005;1751(2):119-139.

126. Bacsik Z, Mink J, Keresztury G. FTIR spectroscopy of the atmosphere. I. Principles and methods. *Applied Spectroscopy Reviews.* 2004;39(3):295-363.

127. Stuart B. *Infrared spectroscopy*: Wiley Online Library; 2005.

128. Bracewell RN, Bracewell RN. *The Fourier transform and its applications.* Vol 31999: McGraw-Hill New York; 1986.

129. Glauert AM, Goodhew PJ. *Practical methods in electron microscopy.* Vol 1: North-Holland Amsterdam; 1972.

130. Thomas G. Transmission electron microscopy of metals. 1962.

131. Fan G, Ellisman M. Digital imaging in transmission electron microscopy. *Journal of microscopy.* 2000;200(1):1-13.

132. Williams DB, Carter CB. The transmission electron microscope. *Transmission electron microscopy*: Springer; 1996: 3-17.

133. Silva Ferreira AC, Rodrigues P, Hogg T, Guedes de Pinho P. Influence of some technological parameters on the formation of dimethyl sulfide, 2-mercaptoethanol, methionol, and dimethyl sulfone in port wines. *Journal of Agricultural and Food Chemistry.* 2003;51(3):727-732.

134. Fish WW, Reynolds JA, Tanford C. Gel chromatography of proteins in denaturing solvents comparison between sodium dodecyl sulfate and guanidine hydrochloride as denaturants. *Journal of Biological Chemistry.* 1970;245(19):5166-5168.

135. Laemmli UK. Cleavage of structural proteins during the assembly of the head of bacteriophage T4. *nature.* 1970;227(5259):680.

136. Pearson K. LIII. On lines and planes of closest fit to systems of points in space. *The London, Edinburgh, and Dublin Philosophical Magazine and Journal of Science.* 1901;2(11):559-572.

137. Wold S, Esbensen K, Geladi P. Principal component analysis. *Chemometrics and*

intelligent laboratory systems. 1987;2(1-3):37-52.

138. Dunteman GH. *Principal components analysis*: Sage; 1989.

139. Jolliffe I. Principal component analysis. *International encyclopedia of statistical science*: Springer; 2011: 1094-1096.

140. Richardson M. Principal component analysis. *URL: http://people maths ox ac uk/richardsonm/SignalProcPCA pdf (last access: 35 2013) Aleš Hladnik Dr, Ass Prof, Chair of Information and Graphic Arts Technology, Faculty of Natural Sciences and Engineering, University of Ljubljana, Slovenia ales hladnik@ ntf uni-lj si.* 2009;6:16.

141. Rencher AC. Principal component analysis. *Methods of Multivariate Analysis, Second Edition.* 2002:380-407.

142. Fisher RA. The use of multiple measurements in taxonomic problems. *Annals of human genetics.* 1936;7(2):179-188.

143. McLachlan G. *Discriminant analysis and statistical pattern recognition.* Vol 544: John Wiley & Sons; 2004.

144. Wang H, Wang Z, Leng Y, Wu X, Li Q. PCA plus F-LDA: A new approach to face recognition. *International Journal of Pattern Recognition and Artificial Intelligence.* 2007;21(06):1059-1068.

145. Yang J, Yang J-y. Why can LDA be performed in PCA transformed space? *Pattern recognition.* 2003;36(2):563-566.

146. Belhumeur PN, Hespanha JP, Kriegman DJ. Eigenfaces vs. fisherfaces: Recognition using class specific linear projection. *IEEE Transactions on pattern analysis and machine intelligence.* 1997;19(7):711-720.

147. Yu H, Yang J. A direct LDA algorithm for high-dimensional data—with application to face recognition. *Pattern recognition.* 2001;34(10):2067-2070.

CHAPTER 2: RATIOMETIC FLUORESCENCE DETECTION OF HYDROXYL RADICALS USING CYANINE-BASED BINARY NANOGUMBOS

2.1 Introduction

Reactive oxygen species (ROS) are formed as byproducts of the metabolism of oxygen within the mitochondria of living cells. ROS generated by this process include superoxide anion ($O_2^{\bullet-}$), hydroxyl radical (•OH), singlet oxygen ($^1O_2$), and hydrogen peroxide (H_2O_2) [1] An imbalance between production and reduction of ROS causes oxidative stress. [2] Furthermore, overproduction of ROS produces significant damage within cells and eventually leads to many diseases including cardiovascular disease, neurological disorders, diabetes, and cancer. [3-8] Hydroxyl radicals (•OH) and hydroxide ions (OH^-) are formed as a result of a Fenton reaction, wherein reduced iron (Fe^{2+}) or copper (Cu^+) is oxidized by use of H_2O_2. [9, 10] Since the hydroxyl radical is considered the most reactive ROS, it has very high aggression toward other molecules [10, 11] and therefore a short life time.[12] For this reason, visual detection of hydroxyl radicals in cells is of utmost importance for examining health-related problems.

Several instrumental techniques such as electron spin resonance (ESR), [13, 14] ultraviolet-visible absorbance (UV-Vis), [14, 15] and fluorescence [11, 14-16] have been used to detect ROS. [17] Among these techniques, fluorescence spectroscopy offers several advantages including

---

This chapter previously appeared as Cong, M., Siraj, N., Bhattarai, N., Kolic, P. E., McCarter, K. S., Chhotaray, P. K., & Warner, I. M. (2018). "Ratiometric fluorescence detection of hydroxyl radical using cyanine-based binary nanoGUMBOS." *Sensors and Actuators B: Chemical*, 257, 993-1000, and is reprinted here by permission of Elsevier.

sensitivity, selectivity, rapid acquisition, and versatility. [11, 12, 15] However, there are limitations to development of a successful real-time fluorescent probe for ROS. For instance, sensitivity of the instrumentation, fluctuation of light-source intensity, temperature, sensor concentration variation, and other environmental factors can affect the reliability of a given probe. [18] A possible solution to this problem is to employ a ratiometric sensor, which could effectively eliminate the aforementioned artifacts through built-in correction from two emission intensities. [18-20] In this regard, a Förster resonance energy transfer (FRET) strategy can be employed to develop such a ratiometric sensor. However, in order to develop a FRET based ratiometric sensor, a certain degree of spectral overlap is required between the emission spectrum of the donor and the absorption spectrum of the acceptor. In addition, the donor and acceptor molecules must be in close proximity (typically 10-100 Å). [21]

Cyanine dyes belong to a family of fluorescent dyes that are widely used in industry, as well as in academic research. Depending on the particular modification of the molecular structure of these dyes, the absorbance and emission characteristics can be tuned from the ultraviolet (UV) to the infrared (IR) regions of the electromagnetic spectrum. [22, 23] Since cyanine dyes are fluorescent, they are frequently employed as fluorescent labels, particularly in the area of biomedical imaging. [3, 24-26] A few studies have reported cyanine dyes as ROS sensors. For example, Karton-Lifshin, et al. have synthesized a quinone-cyanine 7 probe, which behaved as a "turn-on" sensor for hydrogen peroxide. [27] More recently, Oushiki *et al.* have investigated

different ROS reactivity with various cyanine dyes. [28] In these studies, FRET was achieved by linking cyanine dyes with another dye through a complex series of organic reactions.

Our research group has been working on a relatively new class of materials defined as a group of uniform materials based on organic salts (GUMBOS). These materials are solid phase organic salts with a wider range of melting points (25 – 250 °C) than ionic liquids (ILs) (melting point <100 °C). However, similar to ILs, GUMBOS exhibit many attractive characteristics such as excellent thermal and photophysical properties. [29, 30] Furthermore, GUMBOS can also be fabricated into nanoscale materials, termed nanoGUMBOS. NanoGUMBOS can be constructed to possess various properties in a single nanoscale material, allowing easy development of multifunctional organic nanomaterials. [31-33] In recent years, the utility of nanoGUMBOS for a variety of biological applications including drug delivery, medical imaging, sensing, and cancer therapy has been reported. [33-35]

The tunable properties of GUMBOS/nanoGUMBOS enables design of materials for specific applications. [31] It has previously been observed that cyanine based nanoGUMBOS are capable of showing tunable photochemical activity. [29, 36, 37] Such outcomes prompted us to investigate cyanine based nanoGUMBOS as a fluorescent probe for detection of ROS species. [36] In this study, we have used 1,1'-diethyl-2,2'-cyanine bis(trifluoromethanesulfonyl)imide ([PIC][NTf2]) and 1,1'-diethyl-2,2'-carbocyanine bis(trifluoromethanesulfonyl)imide ([PC][NTf2]) to develop this nanoprobe. Thus. a ratiometric fluorescent nanoprobe using FRET

was designed and simply synthesized to form binary nanoGUMBOS. Furthermore, we have investigated the sensitivity of these cyanine based nanoGUMBOS towards different ROS and further used them to quantify hydroxyl radicals. Moreover, an *in vitro* application of hydroxyl radical detection inside cells has been demonstrated by using confocal fluorescence microscopy.

2.2 Materials and Methods

2.2.1 Materials

1,1'-diethyl-2,2'-cyanine (PIC) iodide, 1,1'-diethyl-2,2'-carbocyanine iodide, lithium bis(trifluoromethanesulfonyl)imide (NTF2), phosphate buffered saline (PBS), dimethyl sulfoxide, ethanol, ascorbic acid, copper sulfate, potassium superoxide, and N,N-Dimethylformamide, dimethyl sulfoxide (DMSO) were purchased from Sigma Aldrich (St. Louis, MO). Hydrogen peroxide (30%) and sodium nitrite were purchased from Fisher Scientific (Waltham, MA). Triply deionized distilled water (18.2 megaohm) was obtained from an Aries high purity water system (West Berlin, NJ).

Absorption spectroscopic properties of GUMBOS and nanoGUMBOS were studied using a Shimadzu UV-3101PC UV-Vis scanning spectrometer (Shimadzu, Columbia, MD). Fluorescence emission properties were studied using a Spex Fluorolog-3 spectrofluorimeter (model FL3-22TAU3; Jobin Yvon, Edison, NJ) with a slit width of 5 nm. All spectroscopic studies were performed using quartz cuvets (Starna Cells).

An aliquot (5 µL) of nanoGUMBOS aqueous solution was drop casted onto a carbon-coated copper grid (CF400-Cu, Electron Microscopy Sciences, Hatfield, PA) and air dried at room temperature. Electron micrographs were obtained for characterization of size and morphology using a transmission electron microscope (TEM). The sizes of these nanoGUMBOS were determined by measuring the average of 100 nanoparticles.

Superoxide anion ($O_2^{\cdot -}$) was derived by dissolving KO_2 in DMSO. Peroxynitrite (ONOO-) was chemically generated by reacting $NaNO_2$ with H_2O_2. Singlet oxygen $^1O_2$ was generated by reacting H_2O_2 with NaClO, while hydroxyl radicals were prepared in phosphate buffer (pH=7.4) via the reaction of cuprous sulfate and ascorbic acid, followed with introduction of hydrogen peroxide. Since the lifetimes of these hydroxyl radicals are relatively short, the concentration of Cu^{2+} added, which is directly related to hydroxyl radical concentration, is used to represent the concentration of hydroxyl radicals. [15, 19]

2.2.2 Synthesis of GUMBOS

Cyanine based GUMBOS were synthesized using an anion exchange method in a biphasic solvent system as outlined in previous studies. [31, 33] Briefly, 1,1'-diethyl-2,2'-cyanine iodide ([PIC][I]) or 1,1'-diethyl-2,2'-carbocyanine iodide ([PC][I]) was dissolved in dichloromethane (DCM) and mixed in a 1:1.1 mole ratio with a solution of lithium bis(perfluoroethylsulonyl) imide ([Li][NTf2]) that was previously dissolved using a minimum amount of water. This

mixture was then stirred at room temperature for 24 hours. After completion of this anion exchange reaction, the water soluble lithium iodide byproduct was removed by washing with deionized water. GUMBOS were isolated using rotary evaporation to remove the organic solvent. Finally, these GUMBOS were freeze dried to remove trace amounts of water. Formation of GUMBOS was confirmed using high resolution electrospray ionization mass spectrometry (Supplementary material).

2.2.3 Synthesis of nanoGUMBOS and sample preparation for ROS study

Binary nanoGUMBOS were formed using a reprecipitation method of two GUMBOS posessing the same counter-anion. As a typical synthetic procedure, 100 μL of 1mM [PIC][NTf2] and 10 μL of 1mM [PC][NTf2] in acetonitrile were added dropwise into 5 mL of water with ultra-sonication. The mixture was then sonicated for an additional 10 minutes and allowed to sit undisturbed for 20 minutes in order to attain stable nanoparticles. For ROS reactivity study, all spectra were recorded after incubation of nanoGUMBOS with the specific reactive oxygen or nitrogen species for 5 minutes at room temperature.

2.2.4 In vitro detection of hydroxyl radicals with confocal fluorescence microscopy

In vitro detection of hydroxyl radicals was tested using human breast adenocarcinoma (MDA-MB 231, ATCC no. HTB-26). For this experiment, nanoGUMBOS were prepared in cell media. MDA-MB 231 cells were obtained from American Tissue Culture Collection (ATCC,

Manassas, VA) and grown to 90% confluence as per the instructions. Five thousand (5000) cells were plated on a 35 mm glass bottom petri dish (10 mm micro cell; Ashland, MA, USA) with 3 mL of cell media and incubated for 24 h at 37 °C. After 24 h, the cell media was removed. Then, media containing nanoGUMBOS was added into the petri dish, and cells were incubated again for 30 minutes. Then, media was removed and cells were washed with fresh cell media to remove excess nanoGUMBOS. An aliquot of 1 mL H_2O_2 (200 μM) cell media solution was added for *in vitro* generation of hydroxyl radicals in cells. To another cell plate, 1 mL of cell media was added as a control group. These cells were incubated again for 15 mins. Finally, cell media was removed and cells washed with PBS buffer. All fluorescence images were captured using a HCX PL APOCS 40×1.25 OIL objective lens on the Leica DM IRE2 confocal fluorescence microscope (λ_{ex}=514 nm).

2.3 Results and Discussion

2.3.1 Characterization of GUMBOS and nanoGUMBOS

The formation of GUMBOS products was confirmed by use of electrospray ionization mass spectrometry (Figure 2.1) and the product yield was >95%. In positive ion mode, intense peaks with m/z values of 327.1869 and 353.2025 were observed, corresponding to molecular weights of $[PIC]^+$ and $[PC]^+$ cation, respectively. In the negative ion mode, a peak was observed at 279.9177 m/z which is the characteristic peak of $[NTf2]^-$ anion.

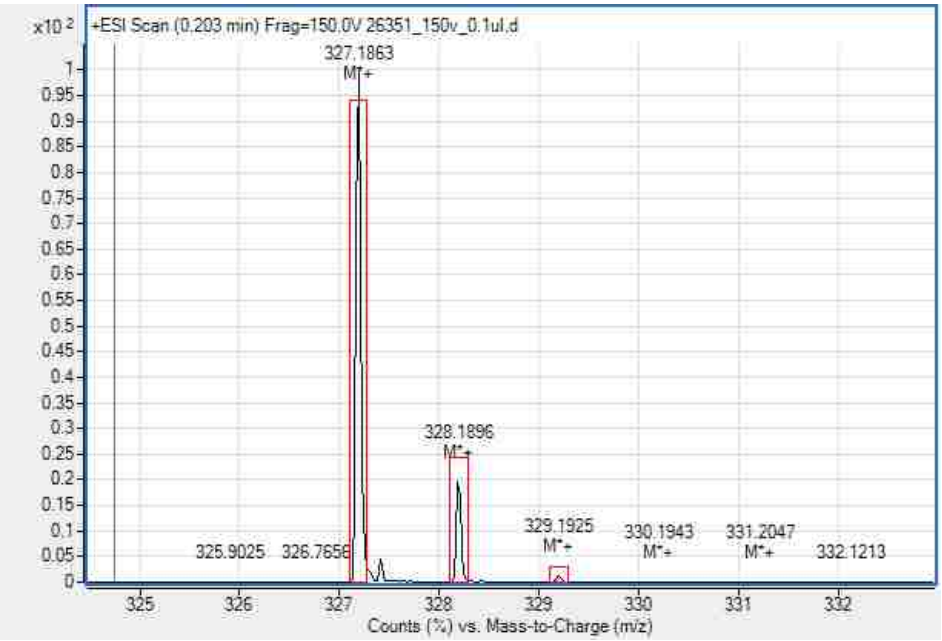

a

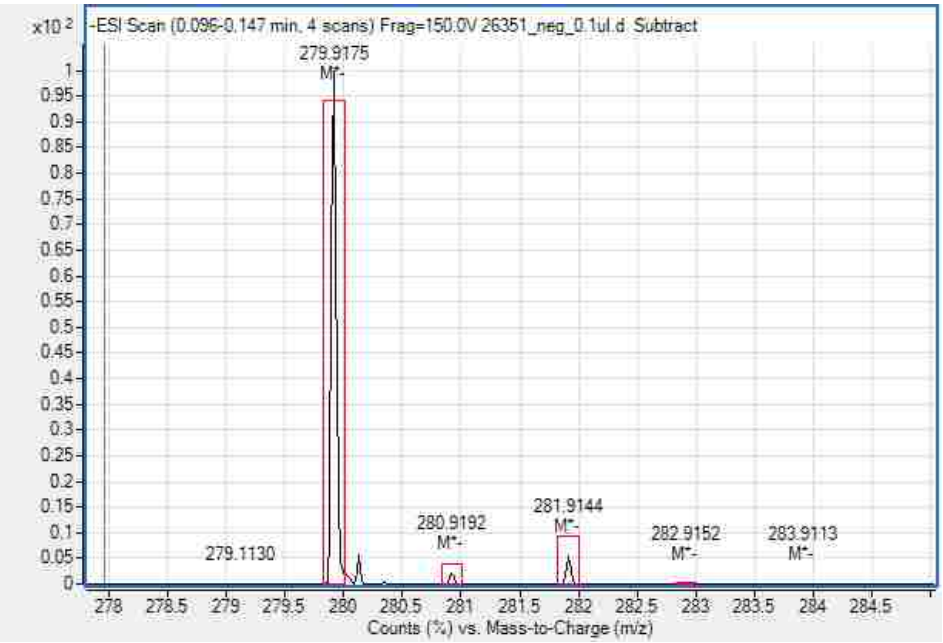

B

Figure 2. 1. High resolution electrospray ionization mass spectrometry for [PIC][NTf2] positive ion mode (a), negative ion mode (b); and [PC][NTf2] positive ion mode (c), negative ion mode (d). (figure cont'd.)

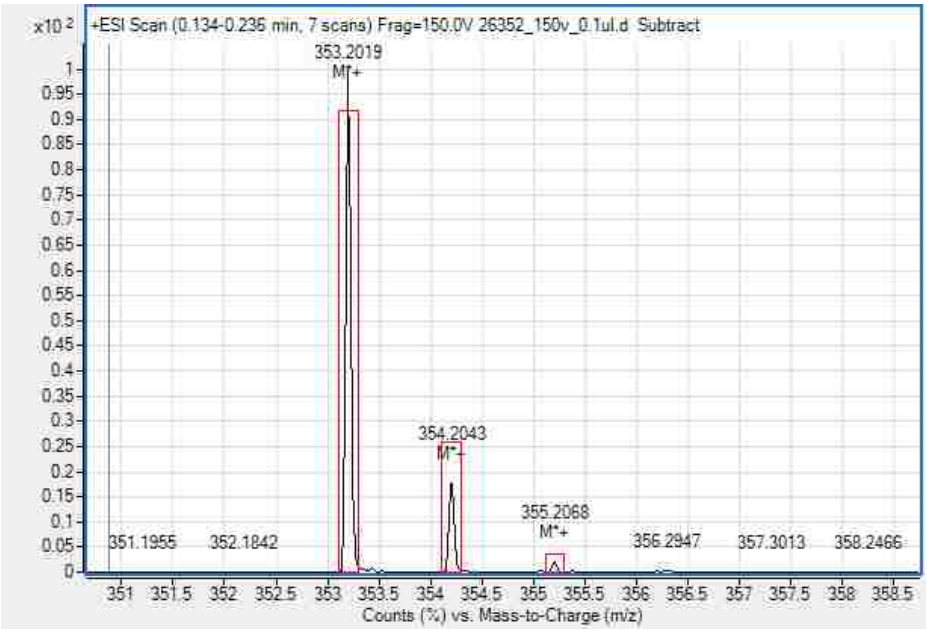
x10 2
+ESI Scan (0.134-0.236 min, 7 scans) Frag=150.0V 26352_150v_0.1ul.d Subtract
353.2019
M*+
354.2043
M*+
355.2068
M*+
351.1955
352.1842
356.2947
357.3013
358.2466
Counts (%) vs. Mass-to-Charge (m/z)

c

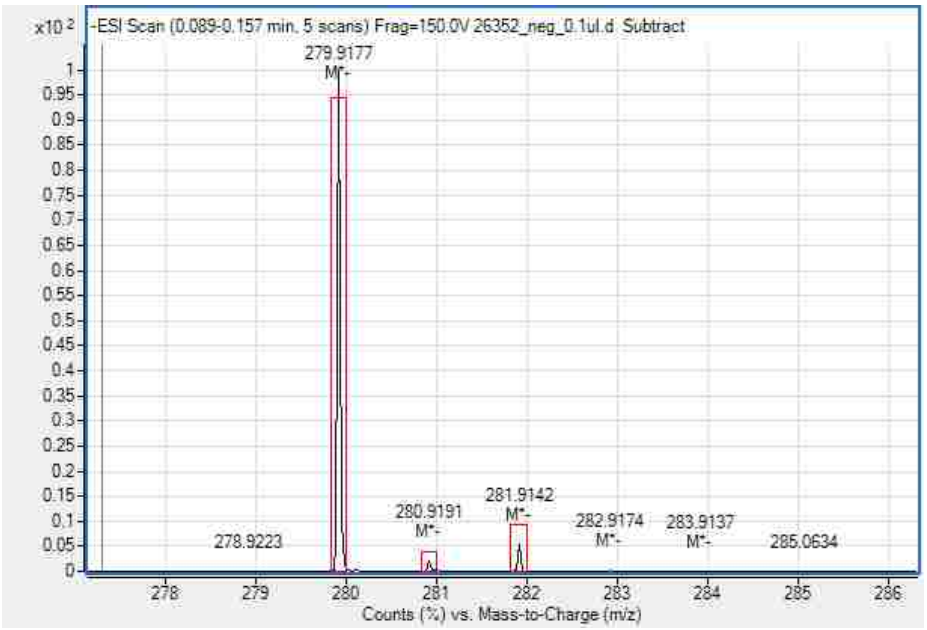
x10 2
-ESI Scan (0.089-0.157 min, 5 scans) Frag=150.0V 26352_neg_0.1ul.d Subtract
279.9177
M*-
280.9191
M*-
281.9142
M*-
282.9174
M*-
283.9137
M*-
278.9223
285.0634
Counts (%) vs. Mass-to-Charge (m/z)

d

TEM images of [PIC-PC][NTf2] nanoGUMBOS (Figure 2.2) exhibit nanodiamonds (NDs). These NDs possess a width of 111.4±15.1 nm and length of about 189.2±16.4 nm. In the literature, NDs have been demonstrated for better cellular uptake as compared to spherical nanoparticles. [38] As described by Chu *et al.*, sharp-shaped nanoparticles enter into the cell via endocytosis using the endosome as the entrance vehicle. Furthermore, NDs have a higher probability of breaking the endosomal membrane before the lysosome is formed, leading to a very low excretion rate and thus allowing these sharp-shaped nanoparticles to remain in the cytoplasm for an extended period of time. [38]

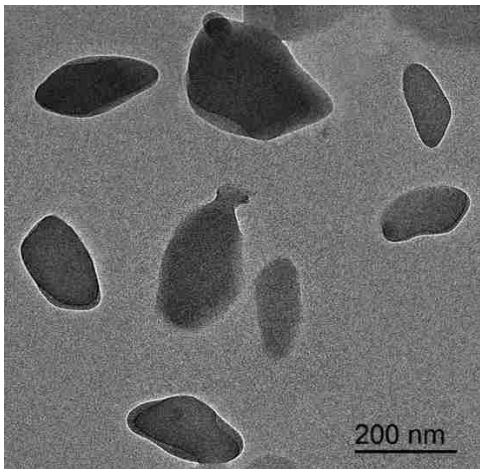

Figure 2. 2. TEM micrograph of [PIC-PC] [NTf2] nanoGUMBOS

2.3.2 Spectroscopic studies

Ultraviolet-visible (UV-vis) and fluorescence spectroscopies were used to study the spectral properties of GUMBOS and nanoGUMBOS. Normalized UV-vis spectra and fluorescence emission spectra of the two individual GUMBOS in acetonitrile are depicted in Figure 2.1. The

absorbance wavelength range of [PIC][NTf2] and [PC][NTf2] are repectively 400 – 580 nm and 500 – 650 nm. Absorbance maxima were observed at 521 nm and 602 nm for [PIC][NTf2] and [PC][NTf2], respectively (Figure 2.3a). As seen in Figure 2.3b, the fluorescence emission wavelengths of [PIC][NTf2] are in the range of 550 nm to 650 nm with emission maxima at 589 nm. The GUMBOS [PC][NTf2], has an emission profile from 610 nm to 750 nm with emission maxima at 616 nm. Based on the spectra given in Figure 2.3, significant overlap is observed between the emission spectrum of [PIC][NTf2] and the absorption spectrum of [PC][NTf2]. This observation suggests the possibility of employing the FRET phenomena between these two cyanine-based GUMBOS. In order to obtain efficient FRET, both GUMBOS were coupled together to produce binary nanoGUMBOS. The UV-Vis absorbance spectrum of [PIC-PC][NTf2] nanoGUMBOS in aqueous solution is shown in Figure 2.4a. These spectra exhibited two peak maxima which correspond to [PIC] and [PC] cations in the binary nanoGUMBOS, since NTf2 does not absorb UV-Visible light. It is observed from the fluorescence spectra that nano[PC][NTf2] alone is not fluorescent (Figure 2.4b). However, in the presence of [PIC][NTf2], two fluorescence emission peaks were observed when excited at 525 nm. The spectra for [PIC-PC][NTf2] nanoGUMBOS (10:1 molar ratio) displayed very good FRET results as depicted in Figure 2.4c.

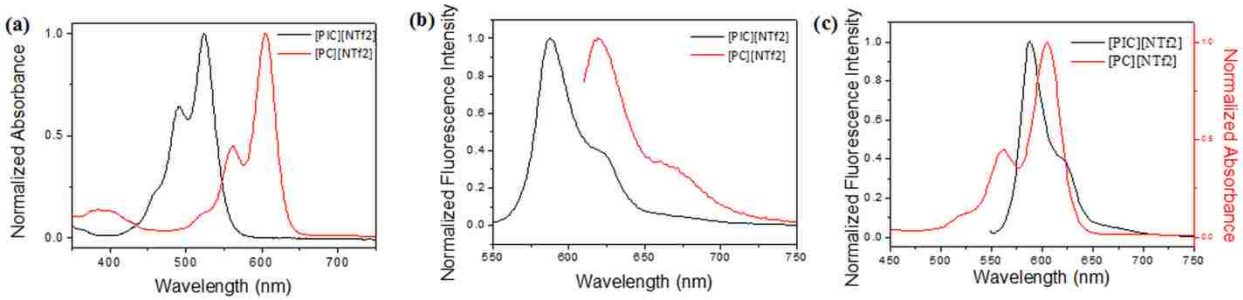

Figure 2. 3. (a) Normalized UV-Vis pectra of the individual GUMBOS [PIC][NTf2] and [PC][NTf2] (acetonitrile); (b) Normalized fluorescence emission spectra of [PIC][NTf2] and [PC][NTf2]; (c) Overlap spectra of [PC][NTf2] absorbance and [PIC][NTf2] fluorescence emission.

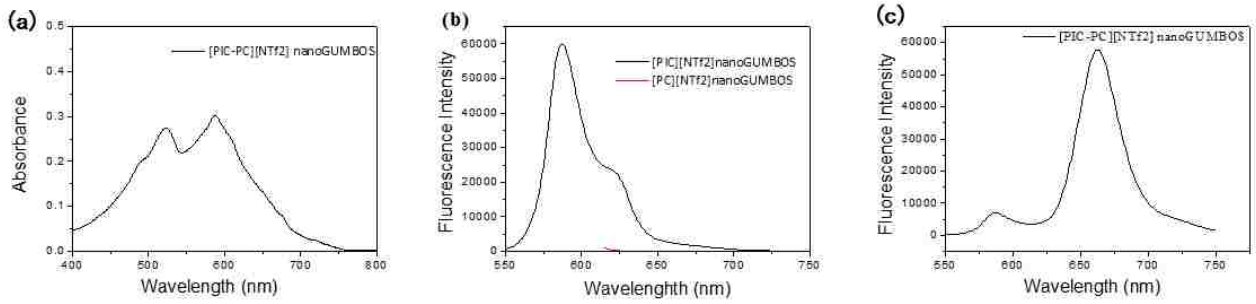

Figure 2. 4. (a) UV-Vis spectrum of [PIC-PC][NTf2] binary nanoGUMBOS in water; (b) Fluorescence spectrum of the individual nanoGUMBOS in water; (c) Fluorescence spectrum of [PIC-PC][NTf2] binary nanoGUMBOS in water, excited at 525 nm

The spectral overlap integral (J) for [PIC-PC][NTf2] binary nanoGUMBOS at a 10:1 molar ratio was calculated using the following equation:

$$J(\lambda) = \int_0^\infty \varepsilon(\lambda)\lambda^4 F_D(\lambda)d\lambda, \qquad (2.1)$$

where $F_D(\lambda)$ is the normalized emission spectrum of the donor, ε is the molar absorption coefficient of the acceptor and λ is wavelength. The energy transfer efficiency (E) was

determined using the following formula:

$$E = 1 - F_D'/F_D, \qquad (2.2)$$

where F_D' and F_D are the donor fluorescence intensities with and without an acceptor, respectively.

The spectral overlap integral for [PIC-PC][NTf2] binary nanoGUMBOS at a 10:1 molar ratio was calculated to be 5.123×10^{-14} M^{-1} cm^3, with an energy transfer efficiency as high as 88.73%. Examination of results revealed that there is significant overlap between the PIC-PC species. Hence, very high FRET efficiency is expected and was observed.

2.3.3 Reactivity evaluation for ROS

Reactivity of [PIC][NTf2] and [PC][NTf2] nanoGUMBOS, towards 50 μM concentration of different reactive species (superoxide anion ($O_2^{\bullet-}$), hydroxyl radicals (•OH), singlet oxygen ($^1O_2$), hydrogen peroxide (H_2O_2), and peroxynitrite ($ONOO^-$) were investigated separately (Figure 2.5). In this regard, we evaluated spectral changes using UV-Vis and fluorescence spectroscopies. Figure 2.5a and Figure 2.5b illustrates absorbance spectra of [PIC][NTf2] and [PC][NTf2] nanoGUMBOS, respectively (in water) in the absence and presence of ROS. As seen in Figures 2.3a and 2.3b, a significant decrease in absorbance intensity was observed for [PC][NTf2] in the presence of hydroxyl radicals, while no significant change in the absorption spectra was observed in the case of [PIC][NTf2] for the same analyte. In addition, the fluorescence spectra

obtained for [PIC][NTf2] nanoGUMBOS did not exhibit a significant change in the presence of ROS (Figure 2.5c); whereas, the fluorescence signal was very low for [PC][NTf2] nanoGUMBOS suspension. Moreover, there is a significant decrease in the intensity of [PC][NTf2] emission when it is exposed to hydroxyl radicals (Figure 2.5d). From these reactivity studies of the individual nanoGUMBOS towards ROS, it can be concluded that [PIC][NTf2] exhibit a lower sensitivity for reactive species as compared to [PC][NTf2]. More specifically, [PC][NTf2] displayed selectivity toward hydroxyl radicals in comparison to other reactive species.

The reduction potentials of cyanine based GUMBOS have been measured using cyclic voltammetry by Jordan *et al.*[36] The results showed that the reduction potential of [PC][NTf2] is lower (-1.04 V) than that of [PIC][NTf2] (-1.01V), suggesting much easier oxidation for [PC][NTf2] than the later. The above electrochemical data also validate our nanoGUMBOS reactivity observation towards reactive oxygen species. Furthermore, similar observations have been achieved by Harriman *et al.* [39] and Chen *et al.* [40] while investigating mechanism of long-chain cyanine compound oxidation. In these reports, oxidation of cyanine with long methine chain would lead to chain cleavage and loss of both the absorbance and fluorescence.

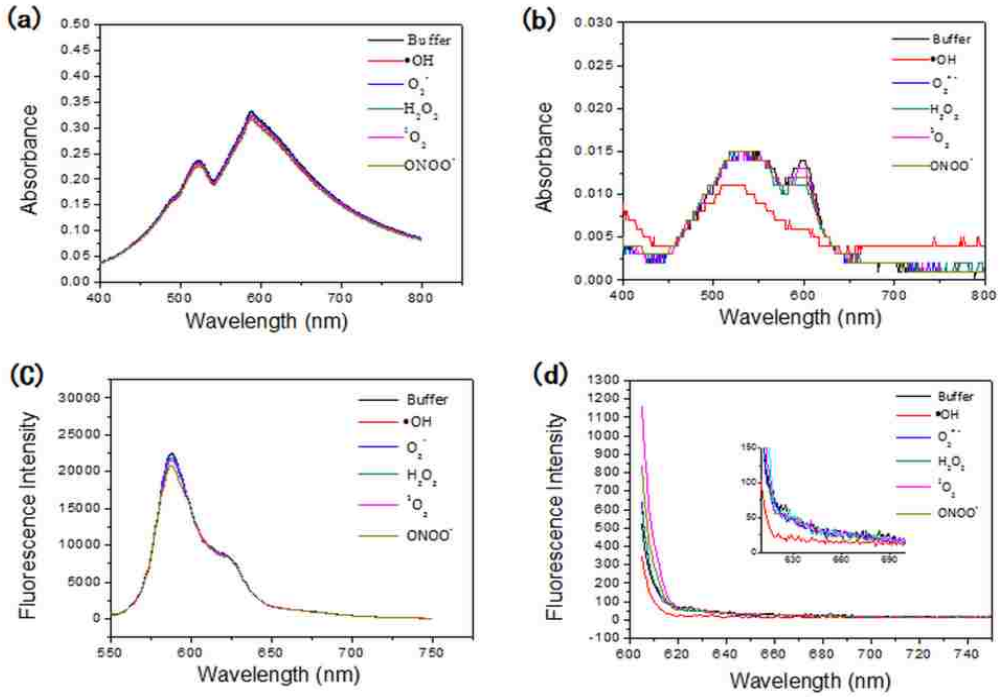

Figure 2. 5. (a) Absorbance spectra of the [PIC][NTf2] nanoGUMBOS with different ROS; (b) Absorbance spectra of the [PC][NTf2] nanoGUMBOS with different ROS; (c) Fluorescence spectra of [PIC][NTf2] nanoGUMBOS with different ROS, excited at 525 nm; (d) Fluorescence spectra of [PC][NTf2] nanoGUMBOS with different ROS excited at 595 nm.

2.3.4 Ratiometric Analysis of ROS with Binary [PIC-PC][NTf2] NanoGUMBOS

The fluorescence spectra of the binary ratiometric nanoprobe were examined using different ROS and results are depicted in Figure 2.6a. Nanoprobe mixing with hydroxyl radicals, shows the lowest emission intensity at 662 nm and highest intensity at 589 nm. All ROS, more or less, decrease [PC][NTf2] emission intensity at 662 nm, but not at 589 nm ($\lambda_{max.em}$ for [PIC][NTf2]). The peak intensity ratio was calculated at 662 nm (λ_{max} for [PC][NTf2]) and 589 nm ($\lambda_{max.em}$ for [PIC][NTf2]). The reactivity of this binary nanoGUMBOS probe was thus defined as

$$Reactivity = -\frac{I662/I589\,(with\ ROS) - I662/I589\,(with\ buffer)}{I662/I589\,(with\ buffer)}. \qquad (2.3)$$

As shown in Figure 2.6b, the binary [PIC-PC][NTf2] nanoprobe shows higher sensitivity towards hydroxyl radicals in comparison to other reactive oxygen species, with hydrogen peroxide being the least sensitive.

When comparing the reduction potentials of these reactive oxygen species (Table 2.1), hydroxyl radicals have the highest reduction potential, followed in order by superoxide, singlet oxygen, and hydrogen peroxide. [12] After combining the reduction potential values of ROS and oxidation potentials of nanoGUMBOS, it is found that the experimental results are in good agreement, i.e, the nanoprobe showed the highest reactivity toward hydroxyl radicals, followed by superoxide and singlet oxygen. Peroxynitrite, known as a versatile oxidant, shows exceptional behavior presumably due to some additional interactions with the nanoprobe. This observation is further corroborated using Figure 2.6a, where the first emission peak ($\lambda_{max.em}$ for [PIC][NTf2]) is significantly reduced only by peroxinitrite. This exceptional behaviour could also be attributed to the size and shape of both nanoprobe and peroxynitrite. The difference in methine chain length in PIC and PC results in different reduction potentials and further leads to different reactivity towards ROS, allowing measurement of a ratiometric fluorescence response to ROS. This measurement greatly adds to the selectivity of this binary nanoprobe and its ability to serve as a ratiometric sensor toward hydroxyl radicals.

Table 2. 1. Reduction potential of reactive species

Reactive Species	Reduction Potential (V)
Hydroxyl radical	2.33
Peroxynitrite	1.25
Superoxide	0.94
Singlet oxygen	0.65
Hydrogen peroxide	0.32

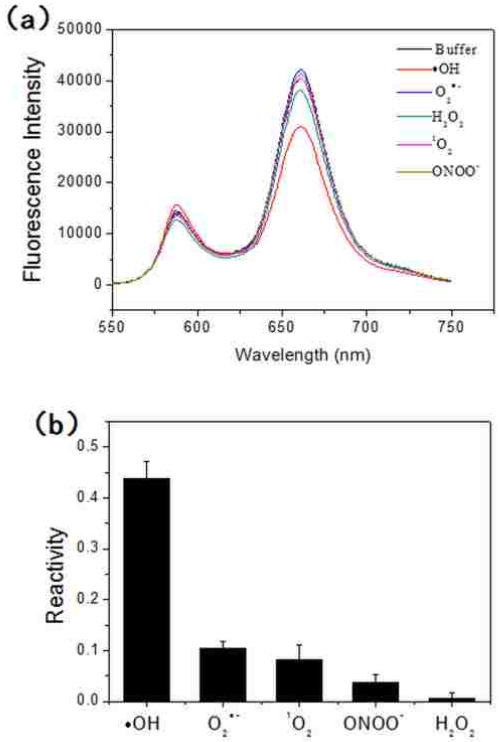

Figure 2. 6. (a) Fluorescence emission spectra of [PIC-PC][NTf2] nanoGUMBOS with different ROS; (b) Reactivity of the binary nanoprobe to different ROS.

The response of this binary nanoGUMBOS was also investigated in the presence of different hydroxyl radical concentrations. In this regard, the concentration of hydroxyl radical was increased from 0 to 25 µM and quenching in the fluorescence spectra was monitored. Results from this experiment are presented in Figure 2.7a. Examination of these results demonstrates micromolar level detection of hydroxyl radicals using binary nanoGUMBOS. A linear relationship was observed between the fluorescence intensity ratio (I_{662}/I_{589}) and hydroxyl radical concentration (Figure 2.7b), with a detection limit of 769 nM ($3\sigma/m$, wherein σ is the standard deviation of blank measurement, and m is the slope of the calibration plot). This relationship will aid in determining the approximate concentration of hydroxyl radicals in an unknown system. Thus, we may conclude that our system is very sensitive and selective towards hydroxyl radicals.

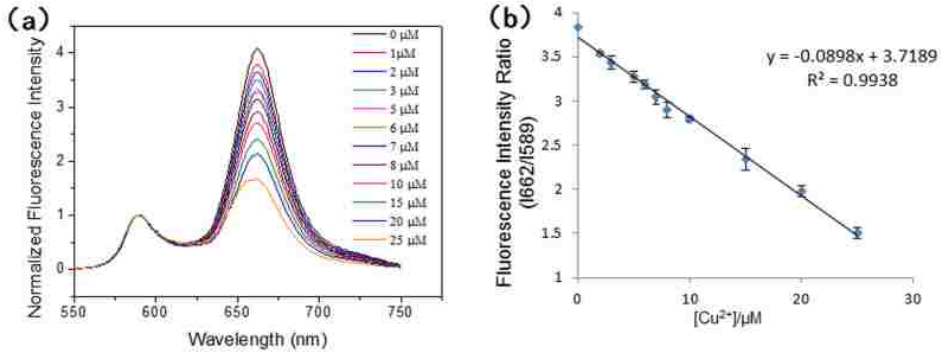

Figure 2. 7. (a) Fluorescence spectra of [PIC-PC][NTf2] nanoGUMBOS with different hydroxyl radical concentration (expressed as the concentration of $[Cu^{2+}]$); (b) Linear relationship between intensity ratio (I_{662}/I_{589}) and hydroxyl radical concentration (represented by $[Cu^{2+}]$)

In order to confirm that the observed change in ratiometric signal is due to the presence of hydroxyl radicals, a control experiment was also designed. All reagents (i.e. Cu^{2+} and hydrogen

peroxide) that were used to generate hydroxyl radicals, were tested individually with nanoGUMBOS. As shown in Figure 2.8, Cu^{2+} and hydrogen peroxide alone did not produce quenching in the fluorescence intensity at 662 nm. Only the hydroxyl radicals, generated after combining Cu^{2+} and hydrogen peroxide, produced a drastic decrease in the fluorescence signal of the nanoprobe.

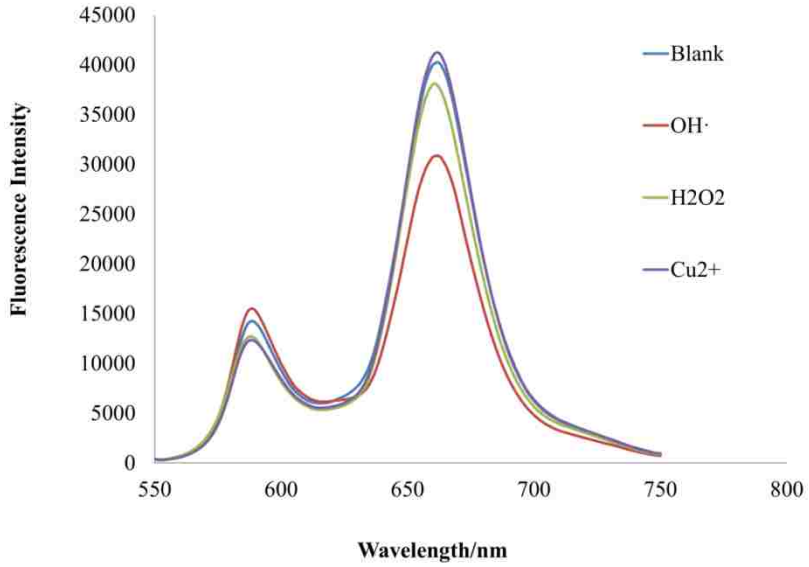

Figure 2. 8. Fluorescence spectra of [PIC-PC][NTf2] nanoGUMBOS with copper sulfate (Cu^{2+}), hydrogen peroxide (H_2O_2), and hydroxyl radicals (·OH) prepared with them.

2.3.5 In vitro detection of hydroxyl radicals

Due to the high selectivity and sensitivity of these binary nanoGUMBOS for hydroxyl radicals, we rationalize that such materials are suitable for detection of hydroxyl radicals in living cells and organisms. Thus, in vitro sensor properties were evaluated using live

hormone-independent human breast adenocarcinoma cells (MDA-MB-231). As reported, hydroxyl radicals are usually generated by the reaction of hydrogen peroxide with transition metals in the biological environment. [2] Thus, we have designed our experiment accordingly. In this regard, MDA-MB-231 cells were incubated with cyanine-based binary nanoGUMBOS and fluorescence images were collected by use of a confocal fluorescence microscope. Images are recorded in two different wavelength regions. One channel (Channel 1) collects the fluorescence signal from 568nm to 608nm, which corresponds to PIC emission, while another channel (Channel 2) collects the fluorescence signal from 613nm to 647nm, which corresponds to PC emission. As shown in Figure 2.9 a, before addition of hydrogen peroxide, Channel 1 provided weak fluorescence signals and Channel 2 produced significant fluorescence. However, when the cells are exposed to hydrogen peroxide, hydroxyl radicals are immediately generated in the cells. Consequently, we observed that fluorescence collected using Channel 1 was enhanced, while fluorescence collected using Channel 2 decreased significantly (Figure 2.9 b). Thus, in vitro studies are in excellent agreement with our solution-based studies, such that we conclude that these cyanine-based binary nanoGUMBOS can serve as ratiometric sensors for detection of hydroxyl radicals in living cells.

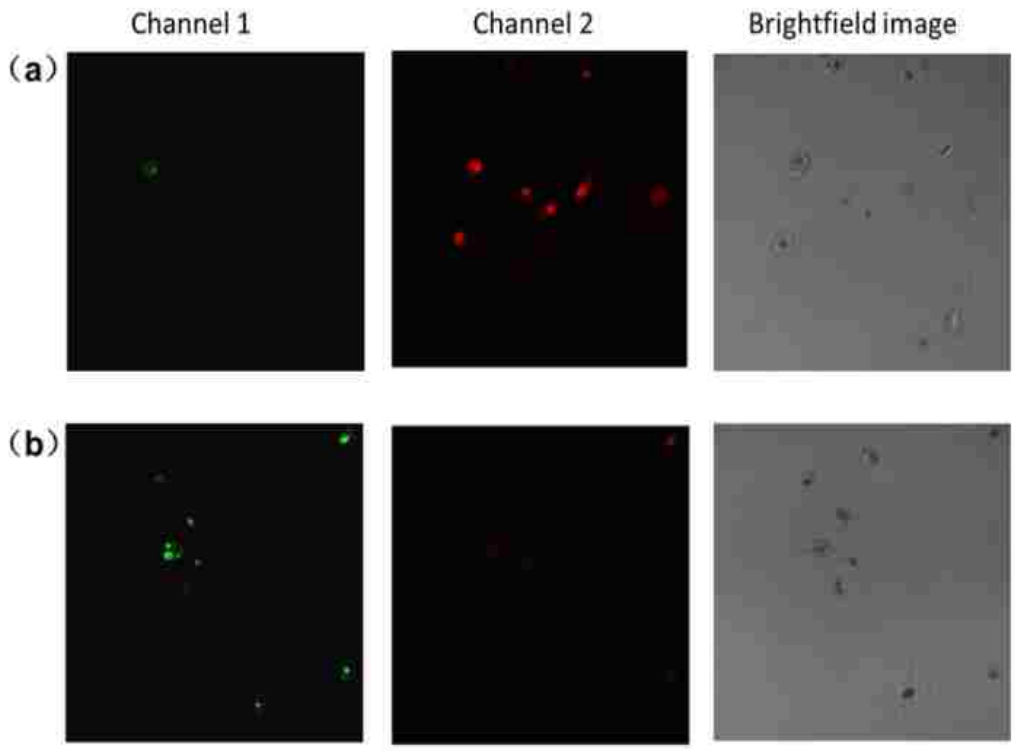

Figure 2. 9. Fluorescent imaging of binary nanoprobe response in live cells exposed to H_2O_2-induced oxidative stress: (a) before addition of H_2O_2 and (b) 15 mins after addition of H_2O_2

2.4 Conclusions

This study involves development of cyanine-based nanoGUMBOS as a simple fluorescence probes for ROS detection. Based on significant spectral overlap and differences in reactivity towards ROS, the two GUMBOS were combined to generate a ratiometric fluorescence response. We have successfully demonstrated that this binary nanoprobe displayed a higher sensitivity and selectivity for hydroxyl radicals over other reactive oxygen species. Moreover, the rapid sensing ability of our binary nanoGUMOS overcomes the restriction due to very short lifetime of

hydroxyl radicals. Based on experimental results, our binary nanoGUMBOS was investigated for *in vitro* application of detecting hydroxyl radicals in human breast adenocarcinoma cells. The results suggest a promising ratiometric probe for hydroxyl radicals detection. We believe that this novel nanoprobe should have a great future in studies aimed at understanding the role of hydroxyl radicals in cellular activity. Furthermore, this approach of investigating binary nanoprobes should serve as the basis for designing other cyanine-based fluorescent sensors for *in vitro* and *in vivo* imaging of ROS.

2.6 References

1. Naoi M, Maruyama W, Shamoto-Nagai M, Yi H, Akao Y, Tanaka M. Oxidative stress in mitochondria. *Molecular neurobiology.* 2005;31(1-3):81-93.

2. Sies H. Oxidative stress: introductory remarks. *Oxidative stress.* 1985:1-8.

3. Chapple I. Reactive oxygen species and antioxidants in inflammatory diseases. *Journal of clinical periodontology.* 1997;24(5):287-296.

4. Wiseman H, Halliwell B. Damage to DNA by reactive oxygen and nitrogen species: role in inflammatory disease and progression to cancer. *Biochemical Journal.* 1996;313(Pt 1):17.

5. Mohanty P, Hamouda W, Garg R, Aljada A, Ghanim H, Dandona P. Glucose challenge stimulates reactive oxygen species (ROS) generation by leucocytes. *The journal of clinical endocrinology & metabolism.* 2000;85(8):2970-2973.

6. Halliwell B. Reactive oxygen species in living systems: source, biochemistry, and role in human disease. *The American journal of medicine.* 1991;91(3):S14-S22.

7. Alfadda AA, Sallam RM. Reactive oxygen species in health and disease. *BioMed Research International.* 2012;2012.

8. Zamzami N, Marchetti P, Castedo M, et al. Sequential reduction of mitochondrial transmembrane potential and generation of reactive oxygen species in early programmed cell death. *Journal of Experimental Medicine.* 1995;182(2):367-377.

9. Imlay JA, Chin SM, Linn S. Toxic DNA damage by hydrogen peroxide through the Fenton reaction in vivo and in vitro. *Science.* 1988;240(4852):640.

10. Winterbourn CC. Toxicity of iron and hydrogen peroxide: the Fenton reaction. *Toxicology letters.* 1995;82:969-974.

11. Liu F, Du J, Song D, Xu M, Sun G. A sensitive fluorescent sensor for the detection of endogenous hydroxyl radicals in living cells and bacteria and direct imaging with respect to its ecotoxicity in living zebra fish. *Chemical Communications.* 2016;52(25):4636-4639.

12. King M, Kopelman R. Development of a hydroxyl radical ratiometric nanoprobe. *Sensors and Actuators B: Chemical.* 2003;90(1):76-81.

13. He W, Liu Y, Wamer WG, Yin J-J. Electron spin resonance spectroscopy for the study of nanomaterial-mediated generation of reactive oxygen species. *Journal of food and drug analysis.* 2014;22(1):49-63.

14. Kuznetsov AV, Kehrer I, Kozlov AV, et al. Mitochondrial ROS production under cellular stress: comparison of different detection methods. *Analytical and bioanalytical chemistry.* 2011;400(8):2383-2390.

15. Burns JM, Cooper WJ, Ferry JL, et al. Methods for reactive oxygen species (ROS) detection in aqueous environments. *Aquatic sciences.* 2012;74(4):683-734.

16. Koide Y, Kawaguchi M, Urano Y, et al. A reversible near-infrared fluorescence probe for reactive oxygen species based on Te–rhodamine. *Chemical Communications.* 2012;48(25):3091-3093.

17. Herman J, Zhang Y, Castranova V, Neal SL. Emerging technologies for optical spectral detection of reactive oxygen species. *Analytical and bioanalytical chemistry.* 2018:1-17.

18. Peng X, Wu Y, Fan J, Tian M, Han K. Colorimetric and ratiometric fluorescence sensing of fluoride: tuning selectivity in proton transfer. *The Journal of organic chemistry.* 2005;70(25):10524-10531.

19. Ganea GM, Kolic PE, El-Zahab B, Warner IM. Ratiometric Coumarin− Neutral Red (CONER) Nanoprobe for Detection of Hydroxyl Radicals. *Analytical chemistry.* 2011;83(7):2576-2581.

20. Das S, Bwambok D, El-Zahab B, et al. Nontemplated approach to tuning the spectral properties of cyanine-based fluorescent nanoGUMBOS. *Langmuir.* 2010;26(15):12867-12876.

21. Jares-Erijman EA, Jovin TM. FRET imaging. *Nature biotechnology.* 2003;21(11):1387-1395.

22. Ernst LA, Gupta RK, Mujumdar RB, Waggoner AS. Cyanine dye labeling reagents for sulfhydryl groups. *Cytometry.* 1989;10(1):3-10.

23. Strekowski L, Mason CJ, Lee H, Gupta R, Sowell J, Patonay G. Synthesis of water‐soluble near‐infrared cyanine dyes functionalized with [(succinimido) oxy] carbonyl group. *Journal of heterocyclic chemistry.* 2003;40(5):913-916.

24. Sims PJ, Waggoner AS, Wang C-H, Hoffman JF. Mechanism by which cyanine dyes measure membrane potential in red blood cells and phosphatidylcholine vesicles. *Biochemistry.* 1974;13(16):3315-3330.

25. Rye HS, Yue S, Wemmer DE, et al. Stable fluorescent complexes of double-stranded DNA with bis-intercalating asymmetric cyanine dyes: properties and applications. *Nucleic acids research.* 1992;20(11):2803-2812.

26. Heilemann M, Van De Linde S, Schüttpelz M, et al. Subdiffraction‐resolution fluorescence imaging with conventional fluorescent probes. *Angewandte Chemie International Edition.* 2008;47(33):6172-6176.

27. Karton-Lifshin N, Segal E, Omer L, Portnoy M, Satchi-Fainaro R, Shabat D. A unique paradigm for a Turn-ON near-infrared cyanine-based probe: noninvasive intravital optical imaging of hydrogen peroxide. *Journal of the American Chemical Society.* 2011;133(28):10960-10965.

28. Oushiki D, Kojima H, Terai T, et al. Development and application of a near-infrared fluorescence probe for oxidative stress based on differential reactivity of linked cyanine dyes. *Journal of the American Chemical Society.* 2010;132(8):2795-2801.

29. Kolic PE, Siraj N, Cong M, et al. Improving energy relay dyes for dye-sensitized solar cells by use of a group of uniform materials based on organic salts (GUMBOS). *RSC Advances.* 2016;6(97):95273-95282.

30. Bwambok DK, El-Zahab B, Challa SK, et al. Near Infrared Fluorescent NanoGUMBOS for Biomedical Imaging. *Acs Nano.* 2009;3(12):3854.

31. Warner IM, El-Zahab B, Siraj N. Perspectives on moving ionic liquid chemistry into the solid phase. *Analytical chemistry.* 2014;86(15):7184-7191.

32. Bwambok DK, El-Zahab B, Challa SK, et al. Near-infrared fluorescent nanoGUMBOS for biomedical imaging. *Acs Nano.* 2009;3(12):3854-3860.

33. Magut PK, Das S, Fernand VE, et al. Tunable cytotoxicity of rhodamine 6G via anion variations. *Journal of the American Chemical Society.* 2013;135(42):15873-15879.

34. Lu C, Das S, Magut PK, Li M, El-Zahab B, Warner IM. Irradiation induced fluorescence enhancement in PEGylated cyanine-based NIR nano-and mesoscale GUMBOS. *Langmuir.* 2012;28(40):14415-14423.

35. Cole MR, Hobden JA, Warner IM. Recycling antibiotics into GUMBOS: A new combination strategy to combat multi-drug-resistant bacteria. *Molecules.* 2015;20(4):6466-6487.

36. Jordan AN, Siraj N, Das S, Warner IM. Tunable near-infrared emission of binary nano-and mesoscale GUMBOS. *RSC Advances.* 2014;4(54):28471-28480.

37. Jordan AN, Das S, Siraj N, et al. Anion-controlled morphologies and spectral features of cyanine-based nanoGUMBOS–an improved photosensitizer. *Nanoscale.* 2012;4(16):5031-5038.

38. Chu Z, Zhang S, Zhang B, et al. Unambiguous observation of shape effects on cellular fate of nanoparticles. *Scientific reports.* 2014;4.

39. Harriman A, Shoute LC, Neta P. Radiation chemistry of cyanine dyes: oxidation and reduction of merocyanine 540. *The Journal of Physical Chemistry.* 1991;95(6):2415-2420.

40. Chen P, Li J, Qian Z, Zheng D, Okasaki T, Hayami M. Study on the photooxidation of a

near-infrared-absorbing benzothiazolone cyanine dye. *Dyes and pigments*. 1998;37(3):213-222.

CHAPTER 3: IMIDAZOLIUM-DYSPROSIUM-BASED NANOGUMBOS FOR ISOLATION OF HEMOGLOBIN

3.1 Introduction

Proteins are an important group of biomolecules that play essential roles in structure, function, and regulation of cells, tissues, and organs of humans. However, due to the typical complexity of the biological environment, protein purification from biological matrices is often a challenging process and thus is a crucial issue in bioscience separations. In this study, we focus on isolation of hemoglobin (Hb), which is a protein with four heme groups and is abundantly present in human red blood cells. Each heme group contains a ferrous cation that is responsible for oxygen transportation. [1, 2] Hemoglobin's oxygen transportation properties make it potentially useful for production of blood substitutes for blood transfusions in extreme situations, particularly for persons with rare types of blood. [3-6] Therefore, as a prerequisite step for such investigations, isolation of Hb has drawn considerable attention over the last decade.

Over the past ten years, several studies on ionic liquid-based liquid-liquid extractions of Hb have been conducted, where the designated ionic liquid (IL) showed good Hb extraction. [7-9] Ionic liquids (ILs) are defined as low melting organic salts that possess useful properties such as biocompatibility, thermal stability, low vapor pressure, considerable ionic conductivities, broad electrochemical window, as well as good solubility and miscibility. [10] Due to these unique properties, ILs have attracted wide recognition as novel green solvents in chemistry, [11-14]

particularly for extraction of analytes. [15-17] In addition, the application of ILs in liquid-liquid extraction systems addresses several issues regarding toxicity of organic solvents. [15, 18, 19] However, problems associated with liquid-liquid extractions, such as incomplete phase separation and disposal of large amounts of solvents, make this method less favorable in practice. [7, 20] In this regard, solid-phase extraction (SPE) overcomes many of the problems noted above. [21-24] In recent years, interest in magnetic solid-phase extraction (MSPE), especially extractions based on magnetic nanomaterials, has increased in order to reduce the time-consuming separation process and provide increased surface area interactions. However, conventional extractions using magnetic nanoparticles are generally based on surface functionalization of magnetic nanoparticles using affinity ligands to increase the selectivity and efficacy of the extraction procedure. [25-31] Frequently, the preparation of these types of nanomaterials with surface functionalization requires tedious synthetic methods in combination with time-consuming purifications.

Similar to ILs, GUMBOS (***g***roups of ***u***niform ***m***aterial ***b***ased on ***o***rganic ***s***alts) are solid phase organic salts that are typically composed of bulky incompatible counter-ions, and thus with a higher range of melting points (25 °C - 250 °C) than ILs (melting point <100 °C). [32] For a wide range of potential applications, properties of GUMBOS such as hydrophobicity, melting point, viscosity, and toxicity can be tuned by simply altering either the cation or anion. In this regard, a variety of GUMBOS have been synthetized in our laboratory with numerous properties

such as fluorescence, magnetic, sensory, and tumor-targeting. [32-36] Multifunctional nanomaterials, prepared from GUMBOS (nanoGUMBOS), have been reported as early as 2008 [35, 37-41] with tunable properties similar to ILs. Thus, GUMBOS may represent very good solid-phase extraction substrates.

Interactions between the ferrous atom in the heme group of Hb and the imidazolium cation present in ILs has been studied for many years. [7, 21, 42, 43] Based on the literature, it is well established that the ferrous atom in the heme group has six coordinating positions, within an octahedral geometry. When the nitrogen atoms in the heme ring occupy four of these positions, one of the two coordinating positions on the vertical axis is occupied by a histidine amino acid, with the other vertical position vacant for coordination with external molecules such as oxygen. This vacant coordinating site can coordinate or interact with other species, such as the imidazolium cation.[7, 21, 42, 43] For this reason, by combining the advantages of MSPE, as well as the properties of imidazolium ILs, a novel magnetic lanthanide-based GUMBOS $[C_{16}mim]_5[Dy(SCN)_8]$ was synthesized using a simple synthetic route. In this GUMBOS material, the magnetic property is produced by use of the cation Dy^{3+} that is paramagnetic at room temperature due to a $4f^9$ electron orbital configuration. NanoGUMBOS can then be fabricated from such a material using a simple reprecipitation method. Such nanoscale MSPE adsorbents exhibit high extraction capacities, as well as efficient and selective adsorption towards Hb. The adsorbed protein can then be desorbed using 1% (m/v) sodium dodecyl sulfate (SDS) aqueous

solution. In this manuscript, we demonstrate application of these magnetic nanoGUMBOS for selective Hb isolation from human whole blood.

3.2 Experimental

3.2.1 Chemicals and apparatus

Potassium thiocyanate, dysprosium(III) oxide, perchloric acid (70%), sodium dodecyl sulfate, and TRIS were obtained from Alfa Aesar (Ward Hill, MA) and used without further purification. Human whole blood was obtained from VWR (Batavia, IL). Lysozyme (Lys) from chicken egg white, transferrin (Trans) (human minimum 98%), Albumin from human serum (HSA) (approx. 99%), cytochrome c (Cyt-c), bovine hemoglobin (Hb), and ammonium persulfate were purchased from Sigma Aldrich (St. Louis, MO). Glycine, glycerol, bromophenol blue, 30% acrylamide stock, TEMED, and 10× running buffer were obtained from Bio-Rad Laboratories (Hercules, California). All solvents used in the preparation process were of analytical reagent grade or better. Deionized water (18 MΩ cm^{-1}) was obtained using an Aries high purity water system (West Berlin, NJ).

3.2.2 Instrumentation and methods

Fourier transform infrared (FT-IR) spectra of designated materials were recorded using a Bruker Tensor 27 spectrometer equipped with a PIKE MIRacle single-bounce attenuated total

reflectance (ATR) cell. Spectra were collected over the 4000–650 cm^{-1} region using 256 scans with a resolution of 2 cm^{-1}. An aliquot (5 μL) of nanoGUMBOS aqueous solution was drop casted onto a carbon-coated copper grid (CF400-Cu, Electron Microscopy Sciences, Hatfield, PA) and air dried at room temperature. Electron micrographs were acquired for characterization of size and morphology using a JEOL JEM-1400 transmission electron microscope (TEM). Circular dichroism spectra were recorded using a Jasco J-815 Circular Dichroism (CD) Spectropolarimeter, operating at a scanning speed of 50 nm/min.

3.2.3 Synthesis of dysprosium-based GUMBOS

$[C_{16}mim]SCN$ was synthesized by reacting $[C_{16}mim]Br$ (1 equiv.) with KSCN (2 equiv.) in ethanol for 48 hours. $Dy(ClO_4)_3 \cdot 6H_2O$ was obtained by dissolving Dy_2O_3 in 50% $HClO_4$ aqueous solution with water-bath heating (70 °C), followed by removal of water through freeze drying. Synthesis of $[C_{16}mim]_5Dy[SCN]_8$ was achieved by reacting $[C_{16}mim]SCN$ (5 equiv.), KSCN (3 equiv.) and $Dy(ClO_4)_3 \cdot 6H_2O$ (1 equiv.) in anhydrous ethanol at room temperature for 24 hours. Byproducts were removed using filtration and ethanol was removed using rotary evaporation. In order to completely eliminate $KClO_4$ byproduct, the residue was redissolved in dry dichloromethane (DCM), left overnight at 4 °C, and then filtered. DCM was removed using rotary evaporation and the product was further dried under vacuum for 24 hours.

3.2.4 Synthesis of nanoGUMBOS

A 32mM $[C_{16}mim]_5Dy[SCN]_8$ methanol stock solution was prepared. A small amount of stock solution was dropped into 10 mL DI water with probe sonication (vibration amplitude 20%) for 5 min. The aqueous solution was left undisturbed for 20 mins. Water was removed under vacuum over 24 hours to obtain nanoparticle pellets. These nanoparticle pellets were resuspended easily in water simply by employing a 1-minute bath sonication.

3.2.5 Protein adsorption studies

To avoid protein denaturation, 0.6 mg of the $[C_{16}mim]_5[Dy(SCN)_8]$ nanoparticle pellets were resuspended into 1mL protein solution while employing a sonication bath for 5 s. This solution was then allowed to cool for 10s in an ice bath. This two-step process was repeated for 3 min. The sample was then shaken vigorously in an oscillator at room temperature for 5 min to facilitate protein adsorption. A magnetic field was applied to the sample in order to separate the proteins adsorbed onto the solid nanoparticles from the aqueous solution. Finally, the concentrations of proteins in the aqueous supernatant were determined by comparing absorption measurements using the characteristic wavelengths (406 nm for Hb and Cyt-c, 280 for HSA, Lys, and Trans) and employing standard calibration curves for each protein obtained using a Shimadzu UV-3101PC UV-Vis scanning spectrometer (Shimadzu, Columbia, MD). All protein adsorption studies were performed in 0.1 M TRIS-HCl buffer at different values of pH.

Elution of the extracted protein was performed by shaking the mixture with 6 mL of SDS aqueous solution for 20 min. The supernatant was then collected for CD study and SDS-PAGE separation using an external magnetic field.

Scheme 3.1 is a representation of the preparation and application of $[C_{16}mim]_5[Dy(SCN)_8]$ nanoGUMBOS for Hb isolation.

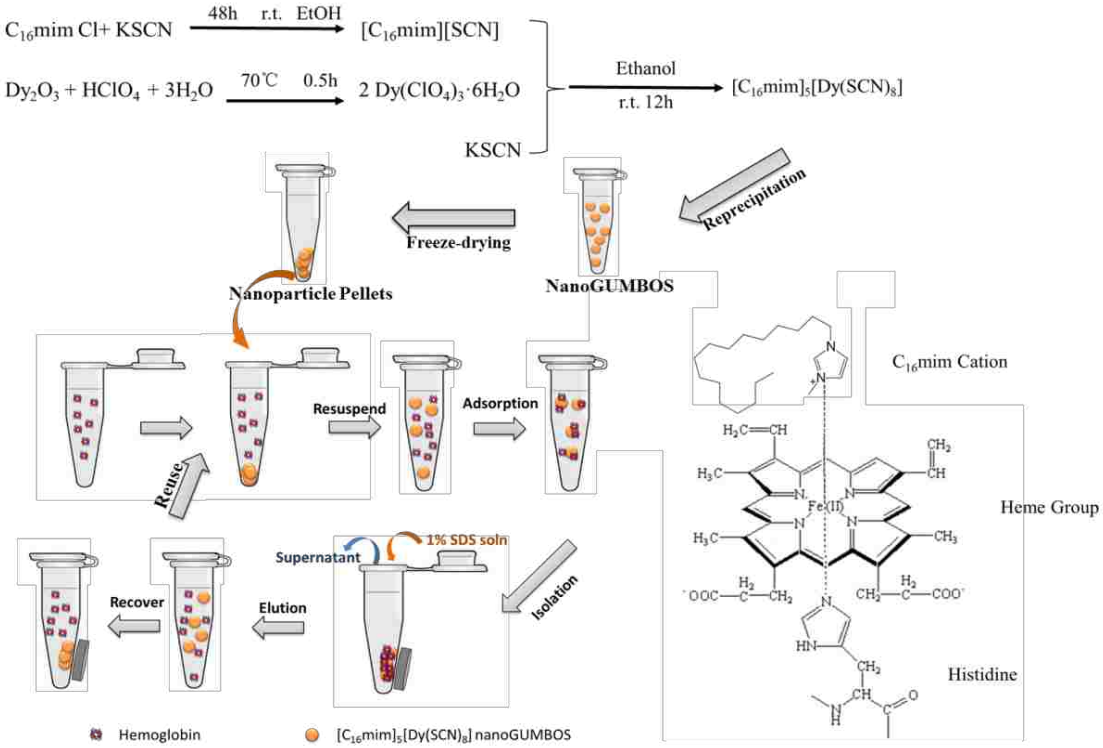

Scheme 3. 1. Preparation of $[C_{16}mim]_5[Dy(SCN)_8]$ nanoGUMBOS and application to Hb isolation

3.3 Results and Discussion

3.3.1 Fabrication and characterization of imidazolium magnetic nanoGUMBOS

Formation of intermediates and final GUMBOS were confirmed by using FT-IR (Figure 3.1) and the product yield was determined to be more than 90%. The characteristic signals of the thiocyanate (S-C≡N) stretching vibration at 2055 cm^{-1}, C-H stretching vibration of alkane chain between 3000-2840 cm^{-1}, the imidazolium ring C-N stretching vibration at 1162 cm^{-1}, and C-H stretching at 3147 and 3106 $cm^{-1}$are displayed in Figure 3.1a, suggesting imidazolium and thiocyanate in the final product. Disappearance of the ClO_4^- stretching bands at 1050 cm^{-1} and 945 cm^{-1} further confirms that the $KClO_4$ byproduct was successfully removed.

The magnetic moment of Dy^{3+} has been reported to be 10.48 μB, which is approximately twice the value of iron (III). [44] Figure 3.1b is a representation of how this new material can be easily and quickly separated from the liquid phase in the presence of an external magnet due to the magnetic property of $[C_{16}mim]_5[Dy(SCN)_8]$ GUMBOS gained by use of dysprosium.

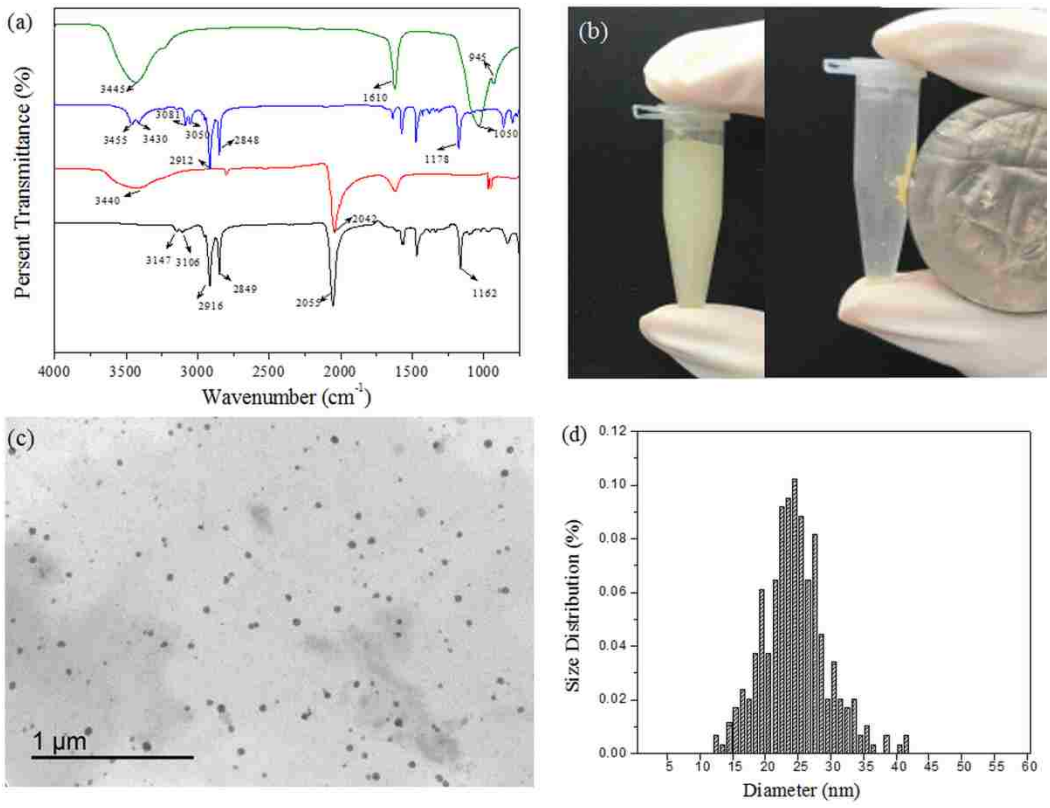

Figure 3. 1. (a) FT-IR spectra of $Dy(ClO_4)_3$ (green line), $[C_{16}mim]Cl$ (blue line), KSCN (red line) and $[C_{16}mim]_5[Dy(SCN)_8]$ (black line); (b) Response of nanoGUMBOS dispersed in water to a neodymium magnet; (c) TEM image of prepared nanoGUMBOS; (d) Size distribution of $[C_{16}mim]_5[Dy(SCN)_8$ nanoGUBMOS as determined by DLS.

Figure 3.1c is a display of a representative TEM image of the resuspended $[C_{16}mim]_5[Dy(SCN)_8]$ nanoparticles, demonstrating that quasi-spherical nanoparticles are generated. As shown in Figure 3.1d, these nanoGUMBOS represent an average size of 24 ± 5 nm with a relatively narrow size distribution for measurement of 200 representative nanoparticles. We note that the high surface-to-volume ratio of nanomaterials is beneficial to improving protein extraction efficiency.

3.3.2 Protein adsorption performance

Time-dependent Hb adsorption was conducted using the synthesized nanoGUMBOS. Results are depicted in Figure 3.2. The absorption of supernatant was recorded from 1.5 min to 15 min, where 1.5 min is the time when we can barely observe any red color from Hb in the supernatant. As shown in Figure 3.2 a, as time reached 5 min, there is negligible absorption of Hb at 406 nm. The extraction efficiency was evaluated and depicted in Figure 3.2 b, which suggested that 5 min is a sufficient extraction time with 95.4% extraction efficiency.

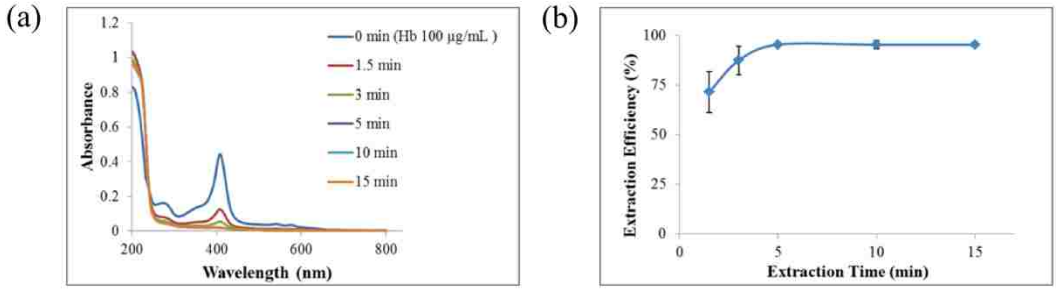

Figure 3. 2. Time-dependent study: (a) UV-Vis spectra of surpernatant solution after extraction using $[C_{16}mim]_5[Dy(SCN)_8]$ nanoGUMBOS, with extraction time of 1.5 min-15 min; (b) extraction efficiency calculated using data from (a).

In addition to Hb, other proteins with different molecular weights and isoelectric points (pI values) were chosen to evaluate the selective protein adsorption performance of the $[C_{16}mim]_5[Dy(SCN)_8]$ nanoGUMBOS. According to the pI values of these proteins (Table 3.1), human serum albumin (HSA) and transferrin (Trans) represent acidic proteins, while lysozyme (Lys) and cytochrome c (Cyt-c) are alkaline proteins. The adsorption properties of these

nanoGUMBOS were studied over a pH value range of 5 to 9.5 using 0.1 M TRIS-HCl buffer. As illustrated in Figure 3.3, the adsorption efficiency of the nanoparticles was much higher for Hb than for the other proteins examined. As discussed earlier, this is attributed to interactions between the ferrous atom in the heme group of Hb and the nitrogen atom in the imidazolium ring. These results are presented in Figure 3.3 and it is observed that adsorption of proteins is pH-dependent. The maximum adsorption efficiency for Hb was achieved at pH 7, while the maximum adsorption efficiencies for Trans, HSA, Cyt-c and Lys were achieved at pH 5, 5, 9, and 9.5, respectively. Analysis of these results shows that the highest adsorption efficiencies were obtained at pH values close to the pI values of these proteins (Table 3.1). This indicates that when the pH value is close to the pI value, the protein is more likely to be adsorbed by $[C_{16}mim]_5[Dy(SCN)_8]$ nanoGUMBOS.. When the value of pH is higher or lower than the pI, proteins are negatively or positively charged, respectively. Conversely, when the value of pH is equal to the pI, proteins are deemed to be in their most hydrophobic state. Since nanoGUMBOS are hydrophobic, proteins are more likely to be adsorbed when they are in their most hydrophobic state. In this regard, hydrophobic interactions are likely a contributor to the success of this approach.

Table 3. 1. Adsorption efficiency of proteins using $[C_{16}mim]_5[Dy(SCN)_8]$ nanoGUMBOS

Tested Protein	Isoelectric point (pI value)	Molecular Weight (kDa)	Maximum adsorption efficiency	pH that maximum adsorption efficiency was achieved	Adsorption efficiency at pH 7
Trans	5.2	80	6.8%	5	2.3%
HSA	5.3	66.5	10.0%	5	2.7%
Hb	6.9	64.5	95.4%	7	95.4%
Cyt-c	10.7	12	12.8%	9.5	4.4%
Lys	11.3	14.3	7.9%	9	1.8%

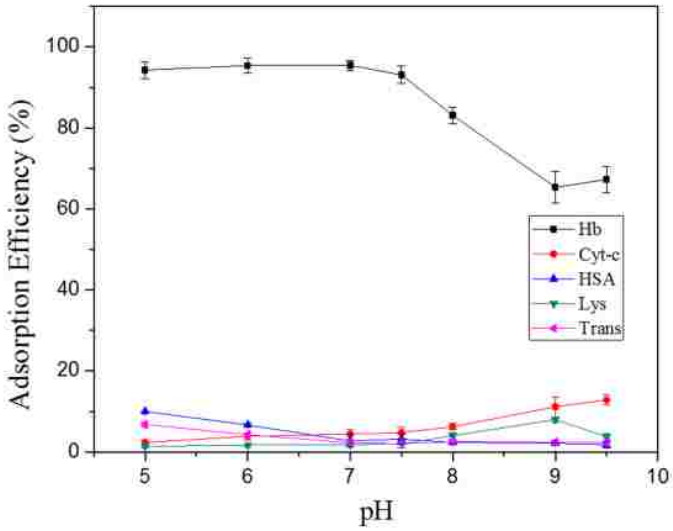

Figure 3. 3. Values of pH dependent extraction efficiencies of major blood proteins using $[C_{16}mim]_5[Dy(SCN)_8]$ nanoGUMBOS. One mL solutions of Hb, HSA, Cyt-c, Lys and Trans with a concentration of 100 µg/mL; tested with 0.6 mg/mL of nanoGUMBOS.

The adsorption of Hb over a concentration range of 10-850 µg/mL was studied at room temperature and the resultant adsorption isotherm is shown in Figure 3.4. TRIS buffer (pH 7.0)

was used for control of neutral Hb. The observed adsorption capacity shows a linear relationship with Hb concentration in the range of 10-400 μg/mL. As the Hb concentration increased to 800 μg/mL, the adsorption capacity approached 840.2 μg/mg and then reached a plateau. The adsorption capacity of $[C_{16}mim]_5[Dy(SCN)_8]$ nanoGUMBOS with difference sizes are compared in Table 3.2. A negative trend was observed between particle size and the adsorption capacity, which is attributed to the decrease of surface area/volume ratio. Table 3.3 compares the current results presented in this work with results from reported Hb adsorption capacities from the literature. [7, 21, 26, 31, 42, 45-48] It is clear that $[C_{16}mim]_5[Dy(SCN)_8]$ nanoGUMBOS offer a favorable adsorption capacity of approximately 840 μg/mL. In comparison with magnetic Hb nanoadsorbents with higher adsorption capacity, such nanoGUMBOS provide an advantage of better selectivity and much simpler preparation. [26, 31]

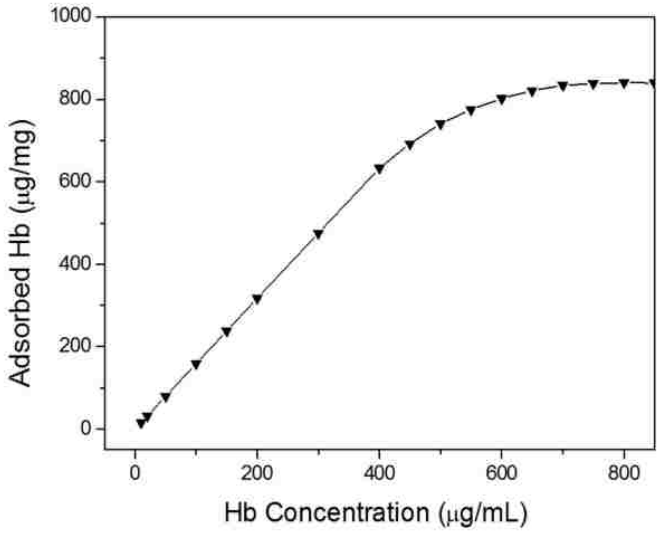

Figure 3. 4. Adsorption isotherm for Hb using $[C_{16}mim]_5[Dy(SCN)_8]$ nanoGUMBOS at room temperature and pH 7.0

Table 3. 2. A comparison of Hb sorption capacity using $[C_{16}mim]_5[Dy(SCN)_8]$ nanoGUMBOS with different sizes

Diameter (nm)	**Surface area/Volume (nm^{-1})**	**Adsorption Capacity ($\mu g\ mg^{-1}$)**
24 ± 5	0.25	840.2
33 ± 8	0.18	822.6
53 ± 11	0.11	657

Table 3. 3. A comparison of Hb sorption capacity using ILs-based materials

Materials	**Adsorption Capacity (μg mg^{-1})**	**Reference**
Bovine hemoglobin magnetic molecularly imprinted polymers	10.5	[48]
PS-CH_2-mimCl	23.6	[42]
PVC-NmimCl	26.5	[46]
SPEEK-Bmim	31.6	[21]
PPimPF_6/TiO_2	122.3	[45]
Cu^{2+}-IDA-poly (methacrylate-divinylbenzene)-Fe_3O_4	168.2	[47]
Poly(C_{12}vim)Br	205.4	[7]
Cu^{2+}-EDTA-Fe_3O_4 Particles	1250	[31]
Fe_3O_4 NPs@SiO_2@IL	2150	[26]
$[C_{16}mim]_5[Dy(SCN)_8]$	840.2	This Work

3.3.3 Elution of adsorbed Hb from $[C_{16}mim]_5[Dy(SCN)_8]$ nanoGUMBOS

Elution of Hb from the adsorbent is required for further investigations and applications of the protein. SDS solution was chosen as the eluent due to favorable dissolution of proteins through disruption of the interactions between Hb and nanoGUMBOS. The Hb elution efficiency was investigated over an SDS concentration range of 0.05%-2% (m/v) in order to avoid extreme denaturation of the protein. Analysis of the elution profile presented in Figure 3.5 indicates that 1% SDS solution produces an elution efficiency of approximately 87%.

In order to evaluate whether the adsorption and elution process would produce a

conformational change to the protein, circular dichroism (CD) spectra of Hb in 1) aqueous solution, 2) Hb in 1% SDS solution and 3) Hb eluted by 1% SDS solution using nanoGUMBOS were compared (Figure 3.6). Evaluation of the results presented in Figure 3.6 demonstrated that the CD spectrum of the native Hb in 1% SDS overlaps with the CD spectrum of Hb after adsorption and subsequent elution. This suggests that there is no conformational change during the adsorption process. When these two spectra were compared with the spectrum of native Hb in aqueous solution, the presence of SDS in the solution shifted the spectrum slightly to the left. Due to this slight change in CD spectrum, the secondary structure of Hb was evaluated by calculating the α-helix content. The calculation method employed in this manuscript has been previously described by Perez-Iratxeta, et al. [49] Hb in 1% SDS contains the same α-helix content as Hb after adsorption and elution, which is 28.9%. In contrast, native Hb in aqueous solution contains 36.3% α-helix. These results suggest that while adsorption does not change the secondary structure of Hb, the Hb conformation slightly changes when dissolved in 1% SDS solution, but remains predominantly α-helix.

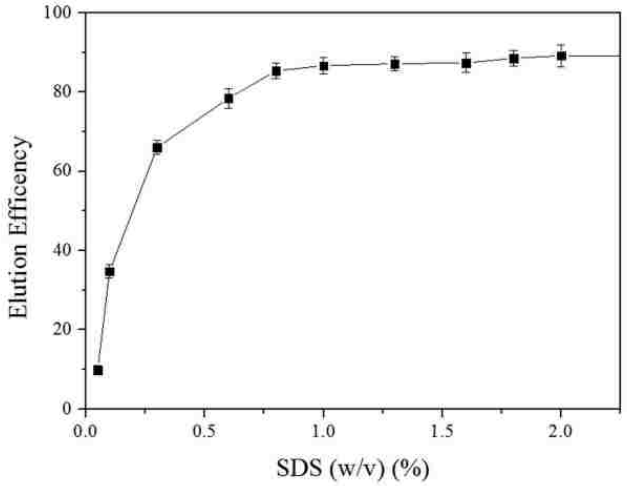

Figure 3. 5. Elution efficiency study of Hb in presence of different SDS concentrations.

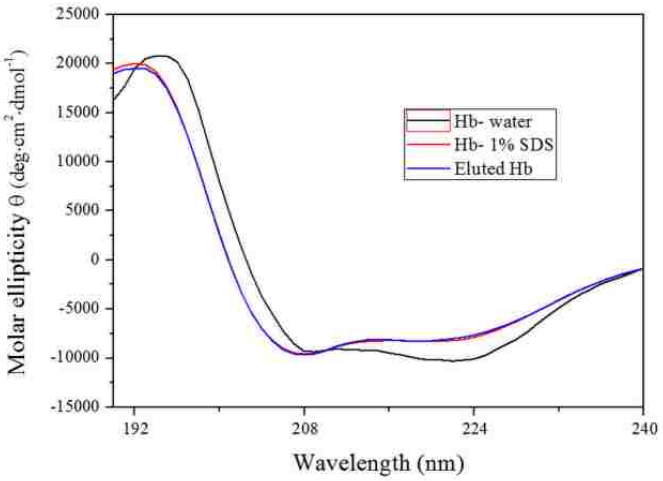

Figure 3. 6. CD spectra of native Hb dissolved in water, Hb dissolved in 1% SDS-PAGE and Hb recovered from $[C_{16}mim]_5[Dy(SCN)_8]$ nanoGUMBOS.

3.3.4 Isolation of Hb from whole blood

Due to the high selectivity and efficiency of nanoGUMBOS for Hb isolation, we hypothesize that such materials are also suitable for selective isolation of Hb from complex biological matrices. Thus, the performance of $[C_{16}mim]_5[Dy(SCN)_8]$ nanoGUMBOS in isolating Hb from practical matrices was evaluated using human whole blood. The blood sample was diluted 200-fold with TRIS buffer (pH 7.0) before performing extraction. To corroborate the selective extraction of Hb from whole blood, the solution was collected after elution in order to perform standard sodium dodecyl sulfate polyacrylamide gel electrophoresis (SDS-PAGE) analysis (Figure 3.7). The results obtained demonstrated that only a few protein bands are visible for 200-fold diluted human whole blood (lane b), while the Albumin band at 66.5 kDa and Hb band at 14.3 kDa can be clearly observed. After performance of the adsorption procedure, the Hb band at 14.3 kDa is noted to be significantly weaker while other protein bands remain (lane c). Lane e was loaded with the solution obtained after elution and a single Hb band was observed. This result reinforces the observed good recovery of Hb from $[C_{16}mim]_5[Dy(SCN)_8]$ nanoGUMBOS using 1% SDS solution. This single band is identical to that for standard Hb solution used in lane d. Thus, whole blood studies are in excellent agreement with our solution-based studies, such that we conclude that these $[C_{16}mim]_5[Dy(SCN)_8]$ nanoGUMBOS can serve as effective magnetic nanosubstrate for selective isolation of Hb from whole blood samples.

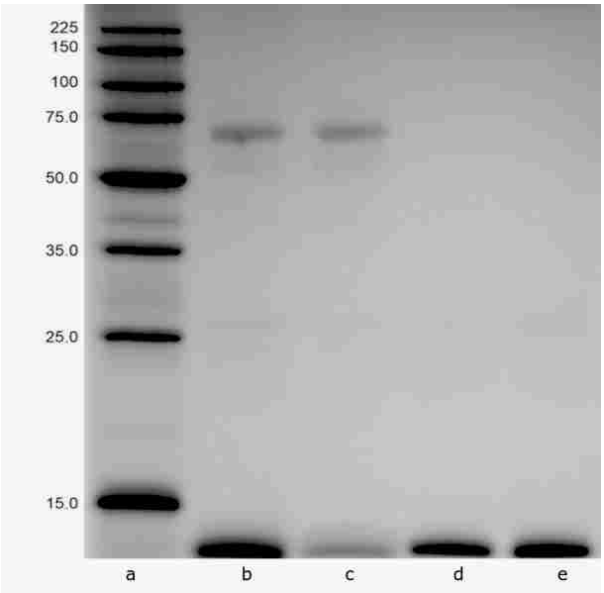

Figure 3. 7. SDS-PAGE results: Lane a: standard protein molecular weight marker; lane b: 200-fold diluted human whole blood; lane c: 200-fold diluted human whole blood after extraction using $[C_{16}mim]_5[Dy(SCN)_8]$ nanoGUMBOS; lane d: 600 µg/mL Hb solution; lane e: Hb recovered from the $[C_{16}mim]_5[Dy(SCN)_8]$ nanoGUMBOS using 1% SDS solution.

3.4 Conclusion

This study involved development of imidazolium-dysprosium-based nanoGUMBOS as magnetic solid phase adsorbents for selective isolation of Hb. These novel $[C_{16}mim]_5[Dy(SCN)_8]$ nanoGUMBOS were easily synthesized to a size of approximately 24 nm through a simple reprecipitation method. Coordination of imidazolium with the ferrous cation in Hb is believed to be the major driving force for selective adsorption of Hb, while hydrophobic interaction also plays a minor role. It has been successfully demonstrated that $[C_{16}mim]_5[Dy(SCN)_8]$ nanoGUMBOS display a significantly higher selectivity for adsorption of Hb over other blood

proteins used in this study. Moreover, in comparison with previously reported Hb adsorbents, these nanoparticles provide a favorable adsorption capacity and efficiency. The adsorbed protein may be successfully recovered by using 1% SDS solution to achieve an elution efficiency of 87%. The recovered Hb remains in a predominantly α-helix structure, suggesting that its tridimensional conformation is essentially intact after extraction. Based on experimental results in prepared solutions, our $[C_{16}mim]_5[Dy(SCN)_8]$ nanoGUMBOS were investigated for practical isolation of Hb isolation from human whole blood. Evaluation of results obtained suggests a promising magnetic nanoadsorbent for isolation of Hb from complex biological samples. Thus, we believe that this novel nanoadsorbent is a promising technique for selective isolation of proteins.

3.6 References

1. Antonini E, Brunori M. *Hemoglobin and Myoglobin*: Elsevier; 1971.

2. Bunn HF, Forget BG. *Hemoglobin--molecular, genetic, and clinical aspects*: WB Saunders Co.; 1986.

3. Hajizadeh S, Kettisen K, Gram M, Bülow L, Ye L. Composite imprinted macroporous hydrogels for haemoglobin purification from cell homogenate. *Journal of Chromatography A.* 2018;1534:22-31.

4. Chen J-Y, Scerbo M, Kramer G. A review of blood substitutes: examining the history, clinical trial results, and ethics of hemoglobin-based oxygen carriers. *Clinics.* 2009;64(8):803-813.

5. Chang TMS. Hemoglobin‐based red blood cell substitutes. *Artificial organs.* 2004;28(9):789-794.

6. Kim HW, Greenburg AG. Artificial oxygen carriers as red blood cell substitutes: a selected review and current status. *Artificial organs.* 2004;28(9):813-828.

7. Wang X-F, Zhang Y, Shu Y, Chen X-W, Wang J-H. Ionic liquid poly (3-n-dodecyl-1-vinylimidazolium) bromide as an adsorbent for the sorption of hemoglobin. *RSC Advances.* 2015;5(40):31496-31501.

8. Du Z, Yu YL, Wang JH. Extraction of Proteins from Biological Fluids by Use of an Ionic Liquid/Aqueous Two‐Phase System. *Chemistry-A European Journal.* 2007;13(7):2130-2137.

9. Shu Y, Cheng D, Chen X, Wang J. A reverse microemulsion of water/AOT/1-butyl-3-methylimidazolium hexafluorophosphate for selective extraction of hemoglobin. *Separation and Purification Technology.* 2008;64(2):154-159.

10. Marsh K, Boxall J, Lichtenthaler R. Room temperature ionic liquids and their mixtures—a review. *Fluid Phase Equilibria.* 2004;219(1):93-98.

11. Pandey S. Analytical applications of room-temperature ionic liquids: A review of recent efforts. *Analytica Chimica Acta.* 2006;556(1):38-45.

12. Rogers RD, Seddon KR. Ionic liquids--solvents of the future? *Science.* 2003;302(5646):792-793.

13. Plechkova NV, Seddon KR. Applications of ionic liquids in the chemical industry. *Chemical Society Reviews.* 2008;37(1):123-150.

14. Wasserscheid P, Keim W. Ionic liquids—new “solutions” for transition metal catalysis. *Angewandte Chemie International Edition.* 2000;39(21):3772-3789.

15. Huddleston JG, Willauer HD, Swatloski RP, Visser AE, Rogers RD. Room temperature ionic liquids as novel media for ‘clean’liquid–liquid extraction. *Chemical Communications.* 1998(16):1765-1766.

16. Clark KD, Nacham O, Yu H, et al. Extraction of DNA by magnetic ionic liquids: tunable solvents for rapid and selective DNA analysis. *Analytical chemistry.* 2015;87(3):1552-1559.

17. Riaño S, Binnemans K. Extraction and separation of neodymium and dysprosium from

used NdFeB magnets: an application of ionic liquids in solvent extraction towards the recycling of magnets. *Green Chemistry.* 2015;17(5):2931-2942.

18. Fan Y, Liu S, Xie Q. Rapid determination of phthalate esters in alcoholic beverages by conventional ionic liquid dispersive liquid–liquid microextraction coupled with high performance liquid chromatography. *Talanta.* 2014;119:291-298.

19. Olkiewicz M, Caporgno MP, Font J, et al. A novel recovery process for lipids from microalgæ for biodiesel production using a hydrated phosphonium ionic liquid. *Green Chemistry.* 2015;17(5):2813-2824.

20. Ding X, Wang Y, Wang Y, et al. Preparation of magnetic chitosan and graphene oxide-functional guanidinium ionic liquid composite for the solid-phase extraction of protein. *Analytica chimica acta.* 2015;861:36-46.

21. Zhao G, Chen S, Yue J, He R-h. Imidazolium-modified sulfonated polyetheretherketone for selective isolation of hemoglobin. *Analytical Methods.* 2013;5(20):5425-5430.

22. Tamayo F, Turiel E, Martín-Esteban A. Molecularly imprinted polymers for solid-phase extraction and solid-phase microextraction: recent developments and future trends. *Journal of Chromatography A.* 2007;1152(1-2):32-40.

23. Tuzen M, Saygi KO, Soylak M. Solid phase extraction of heavy metal ions in environmental samples on multiwalled carbon nanotubes. *Journal of Hazardous Materials.* 2008;152(2):632-639.

24. Haixia Z, Pengling Z. Solid phase extraction. *Chinese Journal of Analytical Chemistry.* 2000;28(9):1172-1180.

25. Ma Y, Xie J, Jin J, et al. Development of a magnetic solid‐phase extraction coupled with high‐performance liquid chromatography method for the analysis of polyaromatic hydrocarbons. *Journal of separation science.* 2015;38(14):2517-2525.

26. Wei Y, Li Y, Tian A, Fan Y, Wang X. Ionic liquid modified magnetic microspheres for isolation of heme protein with high binding capacity. *Journal of Materials Chemistry B.* 2013;1(15):2066-2071.

27. Wierucka M, Biziuk M. Application of magnetic nanoparticles for magnetic solid-phase extraction in preparing biological, environmental and food samples. *TrAC Trends in*

Analytical Chemistry. 2014;59:50-58.

28. Su X, Li X, Li J, et al. Synthesis and characterization of core–shell magnetic molecularly imprinted polymers for solid-phase extraction and determination of Rhodamine B in food. *Food chemistry.* 2015;171:292-297.

29. Huo S-H, Yan X-P. Facile magnetization of metal–organic framework MIL-101 for magnetic solid-phase extraction of polycyclic aromatic hydrocarbons in environmental water samples. *Analyst.* 2012;137(15):3445-3451.

30. Xiao D, Yuan D, He H, et al. Mixed hemimicelle solid-phase extraction based on magnetic carbon nanotubes and ionic liquids for the determination of flavonoids. *Carbon.* 2014;72:274-286.

31. Ding C, Ma X, Yao X, Jia L. Facile synthesis of copper (II)-decorated magnetic particles for selective removal of hemoglobin from blood samples. *Journal of Chromatography A.* 2015;1424:18-26.

32. Warner IM, El-Zahab B, Siraj N. Perspectives on moving ionic liquid chemistry into the solid phase. *Analytical chemistry.* 2014;86(15):7184-7191.

33. Galpothdeniya WIS, Fronczek FR, Cong M, Bhattarai N, Siraj N, Warner IM. Tunable GUMBOS-based sensor array for label-free detection and discrimination of proteins. *Journal of Materials Chemistry B.* 2016;4(8):1414-1422.

34. Kolic PE, Siraj N, Cong M, et al. Improving energy relay dyes for dye-sensitized solar cells by use of a group of uniform materials based on organic salts (GUMBOS). *RSC Advances.* 2016;6(97):95273-95282.

35. Magut PK, Das S, Fernand VE, et al. Tunable cytotoxicity of rhodamine 6G via anion variations. *Journal of the American Chemical Society.* 2013;135(42):15873-15879.

36. Li M, Ganea GM, Lu C, et al. Lipophilic phosphonium–lanthanide compounds with magnetic, luminescent, and tumor targeting properties. *Journal of inorganic biochemistry.* 2012;107(1):40-46.

37. Dumke JC, El-Zahab B, Challa S, et al. Lanthanide-based luminescent nanoGUMBOS. *Langmuir.* 2010;26(19):15599-15603.

38. Tesfai A, El-Zahab B, Kelley AT, et al. Magnetic and nonmagnetic nanoparticles from a group of uniform materials based on organic salts. *Acs Nano.* 2009;3(10):3244-3250.

39. Cong M, Siraj N, Bhattarai N, et al. Ratiometric fluorescence detection of hydroxyl radical using cyanine-based binary nanoGUMBOS. *Sensors and Actuators B: Chemical.* 2018;257:993-1000.

40. Hamdan S, Moore L, Lejeune J, et al. Ionic liquid crosslinkers for chiral imprinted nanoGUMBOS. *Journal of colloid and interface science.* 2016;463:29-36.

41. Kolic PE, Siraj N, Hamdan S, Regmi BP, Warner IM. Synthesis and Characterization of Porphyrin-Based GUMBOS and NanoGUMBOS as Improved Photosensitizers. *The Journal of Physical Chemistry C.* 2016;120(9):5155-5163.

42. Zhao G, Chen S, Chen X-W, He R-H. Selective isolation of hemoglobin by use of imidazolium-modified polystyrene as extractant. *Analytical and bioanalytical chemistry.* 2013;405(15):5353-5358.

43. Wang Y, Yang C, Sun Y, Qiu F, Xiang Y, Fu G. Synthesis of thermo‐responsive bovine hemoglobin imprinted nanoparticles by combining ionic liquid immobilization with aqueous precipitation polymerization. *Journal of separation science.* 2017.

44. Joseph A, Żyła G, Thomas VI, Nair PR, Padmanabhan A, Mathew S. Paramagnetic ionic liquids for advanced applications: A review. *Journal of Molecular Liquids.* 2016;218:319-331.

45. Meng H, Chen X-W, Wang J-H. One-pot synthesis of N, N-bis [2-methylbutyl] imidazolium hexafluorophosphate–TiO2 nanocomposites and application for protein isolation. *Journal of Materials Chemistry.* 2011;21(38):14857-14863.

46. Shu Y, Chen X-W, Wang J-H. Ionic liquid–polyvinyl chloride ionomer for highly selective isolation of basic proteins. *Talanta.* 2010;81(1-2):637-642.

47. Ma ZY, Guan YP, Liu XQ, Liu HZ. Preparation and characterization of micron‐sized non‐porous magnetic polymer microspheres with immobilized metal affinity ligands by modified suspension polymerization. *Journal of Applied Polymer Science.* 2005;96(6):2174-2180.

48. Kan X, Zhao Q, Shao D, Geng Z, Wang Z, Zhu J-J. Preparation and recognition

properties of bovine hemoglobin magnetic molecularly imprinted polymers. *The Journal of Physical Chemistry B.* 2010;114(11):3999-4004.

49. Perez-Iratxeta C, Andrade-Navarro MA. K2D2: estimation of protein secondary structure from circular dichroism spectra. *BMC structural biology.* 2008;8(1):25.

CHAPTER 4: PROTEIN DISCRIMINATION USING A FLUORESCENCE BASED SENSOR ARRAY OF THIACARBOCYANINE-GUMBOS

4.1 Introduction

Highly sensitive and precise sensing of multiple proteins simultaneously is of great interest for clinical diagnosis and proteomic research. Currently, enzyme-linked immunosorbent assay (ELISA) is the most widely used protein sensing technique. [1-3] The sensing mechanism of ELISA is based on specific binding interactions between each antibody and its targeting protein. [4] This allows ELISA to be an effective sensor with excellent specificity and sensitivity; [5, 6] however, only a few proteins can be detected by use of this method. In addition, the high cost and low stability of antibodies limit the application of ELISA in protein sensing.

Alternatively, cross-reactive sensor arrays, known as "electronic noses", have been employed for high-throughput detection and discrimination of proteins. [7-12] In this approach, receptors (sensing elements) are not responsive to one specific protein as in the traditional "lock-and-key" method, but rather are partially selective. In other words, certain receptors in a sensor array can respond to multiple proteins while multiple receptors can interact with a certain protein. By integrating multiple sensing elements, a distinct response pattern will form for each protein and can be used as a fingerprint for discrimination and identification. [13, 14] Diverse receptor systems have been applied for array sensing of protein, such as functionalized gold nanoparticles, [7, 15-17] fluorescent polymers, [8, 18] carbon nanotubes, [17, 19-21] and porphyrins. [22, 23]

Among these sensing materials, the fluorescence technique has been a method of choice due to its high sensitivity. However, application of this technology is hampered by complicated design and synthesis.

Herein, we demonstrate a fluorescence-based sensor array using a ***g***roup of ***u***niform ***m***aterials ***b***ased on ***o***rganic ***s***alts (GUMBOS) for sensitive and accurate protein discrimination. The concept of GUMBOS was first introduced by the Warner research group in 2008, as solid phase organic salts with tunable properties similar to ionic liquids (ILs), but with a wider range of melting points (25°C to 250°C) than ILs (melting point <100°C). [24] The GUMBOS employed in this work consist of a series of fluorescent thiacarbocyanine (TC) cations bearing different methine chain lengths (Figure 4.7). TC-dyes belong to a dye family called polymethine dyes (PD). The alternating π-electrons along the methine chain of PD allow high polarizability, which provides strong attractive dispersion forces between molecules. [25] Thus, the structures of TC dyes allow extended and stable aggregation. [26] Their association enthalpies have been found to be much higher than other aromatic compounds. [27] It was also found that aggregation of PD is highly depended on the composition of the surrounding environment. [28-36] In particular, researches on noncovalent interactions between cyanine dyes and biomolecules are of great interest. [28, 36-38] These interactions vary the aggregation of dyes and hence remarkably alter their photophysical and photochemical properties. Due to favorable properties mentioned above, TC dyes have great potential to be used for fluorescence protein sensing. Notably, the

bis(trifluoromethylsulfonyl)imide ($[NTf2]^-$) and bis[(pentafluoroethyl)sulfonyl]imide ($[BETI]^-$) anions were selected to increase hydrophobicity of the GUMBOS and facilitate aggregation at low concentrations.

The six TC-based sensor elements utilized in this sensor array, exhibit different aggregation behaviors when mixed with the seven proteins, giving various fluorescence responses. The resulting responses exhibit cross-reactive patterns, which can be analyzed to discriminate proteins at a low concentration. The fluorescence sensor array developed in this study shows great potential for development of highly sensitive diagnostic applications.

4.2 Experimental

4.2.1 Materials and instrumentation

The thiacarbocyanine (TC) dyes, 3,3'-diethylthiacyanine iodide ([TC0][I]), 3,3' -diethylthiacarbocyanine iodide ([TC1][I]), and 3,3'-diethylthiadicarbocyanine iodide ([TC2][I]), were purchased from Sigma Aldrich (St. Louis, MO). Lysozyme (Lys) from chicken egg white, human transferrin (Trans) (> 98%), albumin from human serum (HSA) (approx. 99%), cytochrome c (Cyt-c), Immunoglobulin G from human serum (IgG), fibrinogen from human plasma (Fib), human hemoglobin (Hb), ammonium persulfate, sodium phosphate dibasic and sodium phosphate monobasic were all purchased from Sigma Aldrich. Lithium bis(trifluoromethane)sulfonamide (Li[NTf2]) salt and lithium

bis(pentafluoroethanesulfonyl)imide (Li[BETI]) salt were obtained from TCI Portland, Oregon. Artificial urine, HPLC grade ethanol and dichloromethane were acquired from VWR (Batavia, IL). Triple deionized ultrapure water (18.2 M Ω cm) was obtained using an Aries high purity water system (West Berlin, NJ). All reagents were used without further purification.

Ultraviolet-visible (UV-vis) absorption properties were studied using a Shimadzu UV-3101PC UV-Vis scanning spectrometer (Shimadzu, Columbia, MD). Fluorescence emission spectra were recorded uisng a Spex Fluorolog-3 spectrofluorimeter (model FL3-22TAU3; Jobin Yvon, Edison, NJ) with a slit width of 5 nm. All spectroscopic studies were performed using quartz cuvettes (Starna Cells).

The starting materials, intermediates and final product in solid state were deposited on an ATR cell in a Bruker Tensor 27 instrument (Billerica, MA) to obtain their FTIR spectra. Transmission electron images were obtained for characterization of size and morphology using a JEOL JEM-1400 Transmission Electron Microscope (München, Germany).

4.2.2 Preparation and Characterization of TC-GUMBOS

The TC-GUMBOS were synthesized using an ion exchange reaction between TC iodides and Li[NTf2] (or Li[BETI]) at a molar ratio of 1 to 1.1. The reactions were performed in a biphasic mixture of DCM and water while stirring for 24 h at room temperature. Residual lithium iodide byproducts were washed several times with DI water. DCM was removed using rotary

evaporation. Finally, the GUMBOS were dried under vacuum. The resultant TC-GUMBOS were characterized using high resolution electrospray ionization mass spectrometry.

4.2.3 Preparation of Protein Solutions

Protein samples were prepared in 10 mM sodium phosphate buffer (pH=7.4). Stock solutions of 200 μg/mL were first prepared and diluted to concentrations ranging from 0.1 to 20 μg/mL.

4.2.4 Sensing Process

TC-GUMBOS aggregates were prepared using a reprecipitation method.[39, 40] Briefly, 50 μL of 0.5 mM ethanolic TC-GUMBOS solution was dropped into a 5 mL protein solution and sonicated on ice for 3 min. After the sensor-protein solution was allowed to stabilize for 15 min, the spectral properties were characterized using UV-vis and fluorescence spectrophotometry.

In this study, the relative emission intensity change ($^{I}/_{I_0} - 1$) is considered as a sensor response. Here, I and I_0 represent emission intensity of TC-GUMBOS in buffer with and without proteins, respectively. For each analyte, six replicate samples were analyzed.

4.3 Results and Discussion

4.3.1 TC-GUMBOS Sensors

Preparation of TC-GUMBOS is a one-step ion exchange reaction, which is very simple in comparison with traditional covalent modification reactions. The formation of TC-based GUMBOS was confirmed by high resolution electrospray ionization mass spectrometry (Figure 4.1 – Figure 4.6). In positive ion mode, intense peaks with m/z of 339.099, 365.11 and 391.13 m/z were observed, corresponding to the molecular weights of $[TC0]^+$, $[TC1]^+$ and $[TC2]^+$ cations, respectively. In negative ion mode, peaks were observed at 279.92 and 379.91 m/z which are the characteristic peaks of the $[NTf2]^-$ and $[BETI]^-$ anions, respectively. The chemical structures of these TC GUMBOS are shown in Figure 4.7.

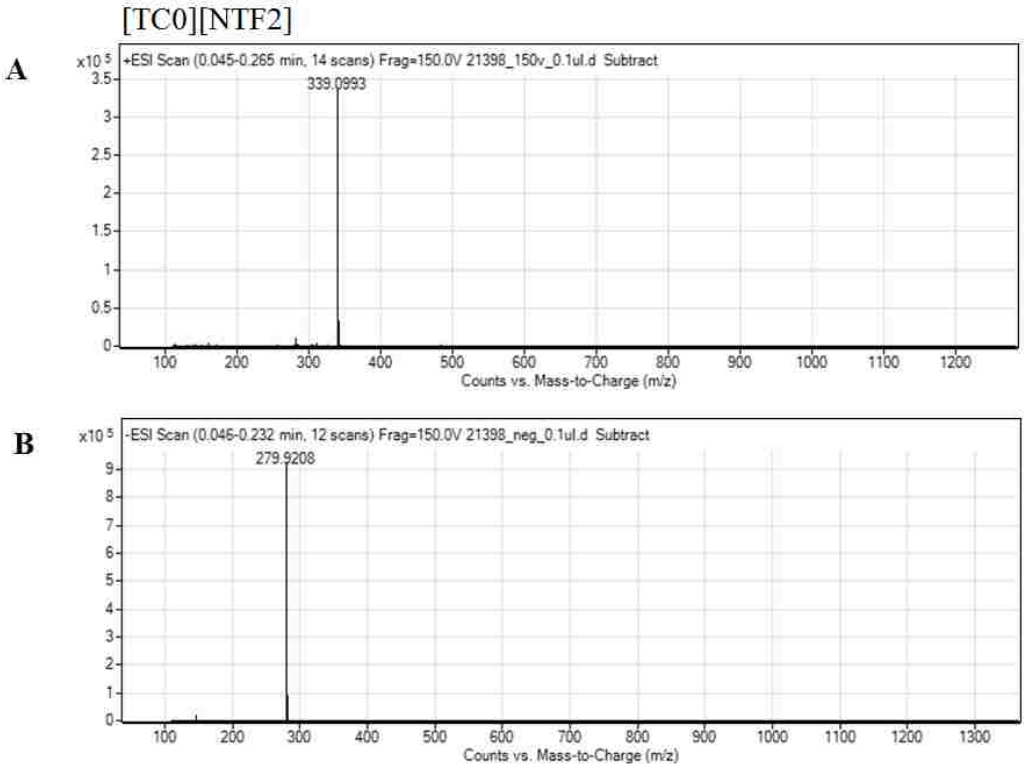

Figure 4. 1. High resolution electrospray ionization mass spectrometry for [TC0][NTf2] positive ion mode (A), negative ion mode (B).

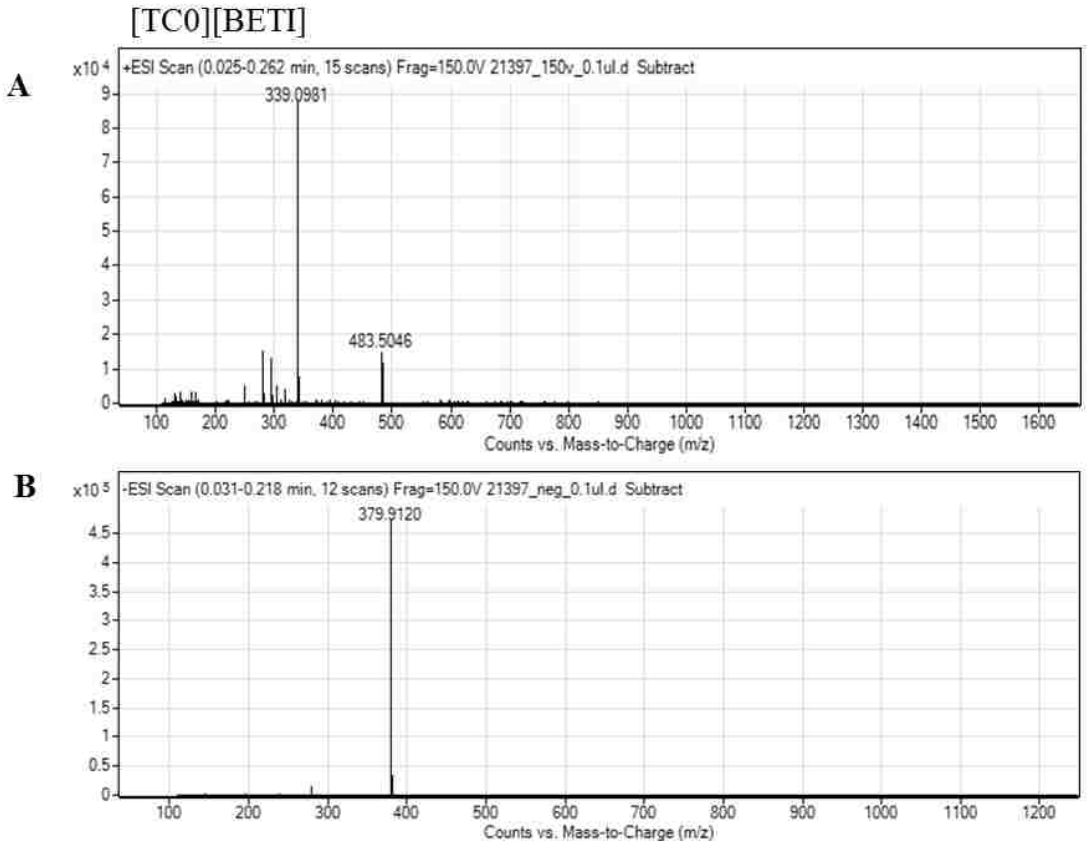

Figure 4. 2. High resolution electrospray ionization mass spectrometry for [TC0][BETI] positive ion mode (A), negative ion mode (B).

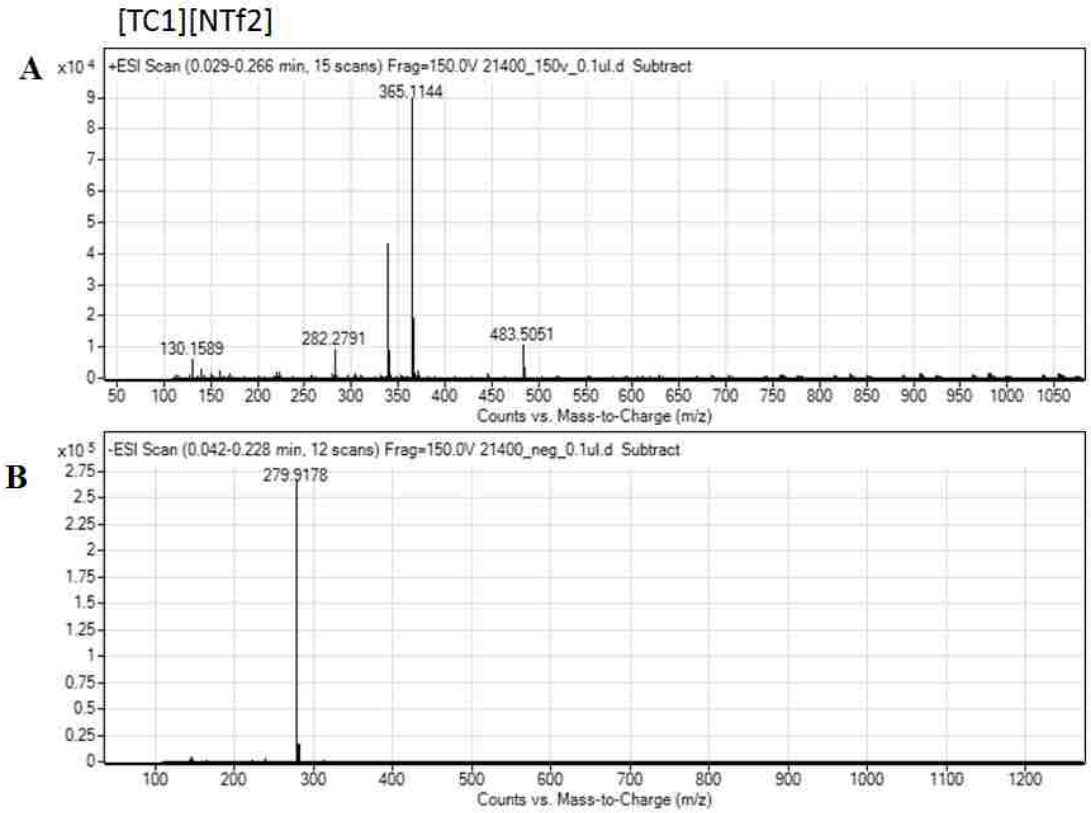

Figure 4. 3. High resolution electrospray ionization mass spectrometry for [TC1][NTf2] positive ion mode (A), negative ion mode (B).

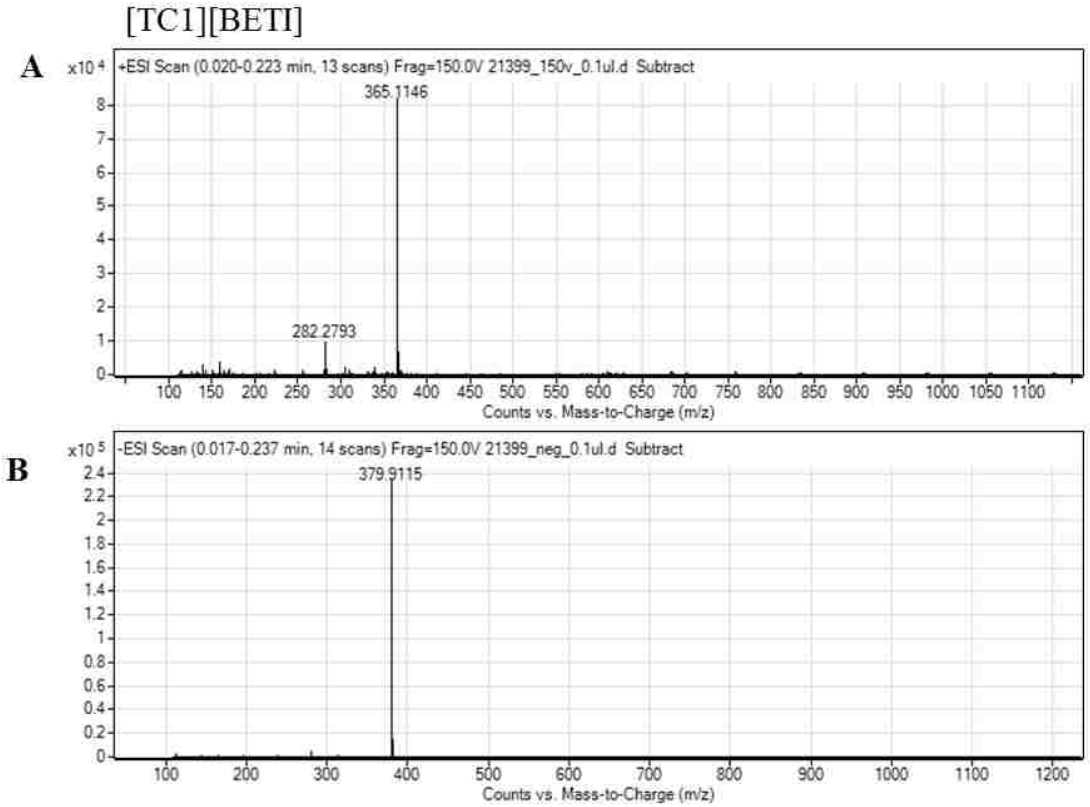

Figure 4. 4. High resolution electrospray ionization mass spectrometry for [TC1][BETI] positive ion mode (A), negative ion mode (B).

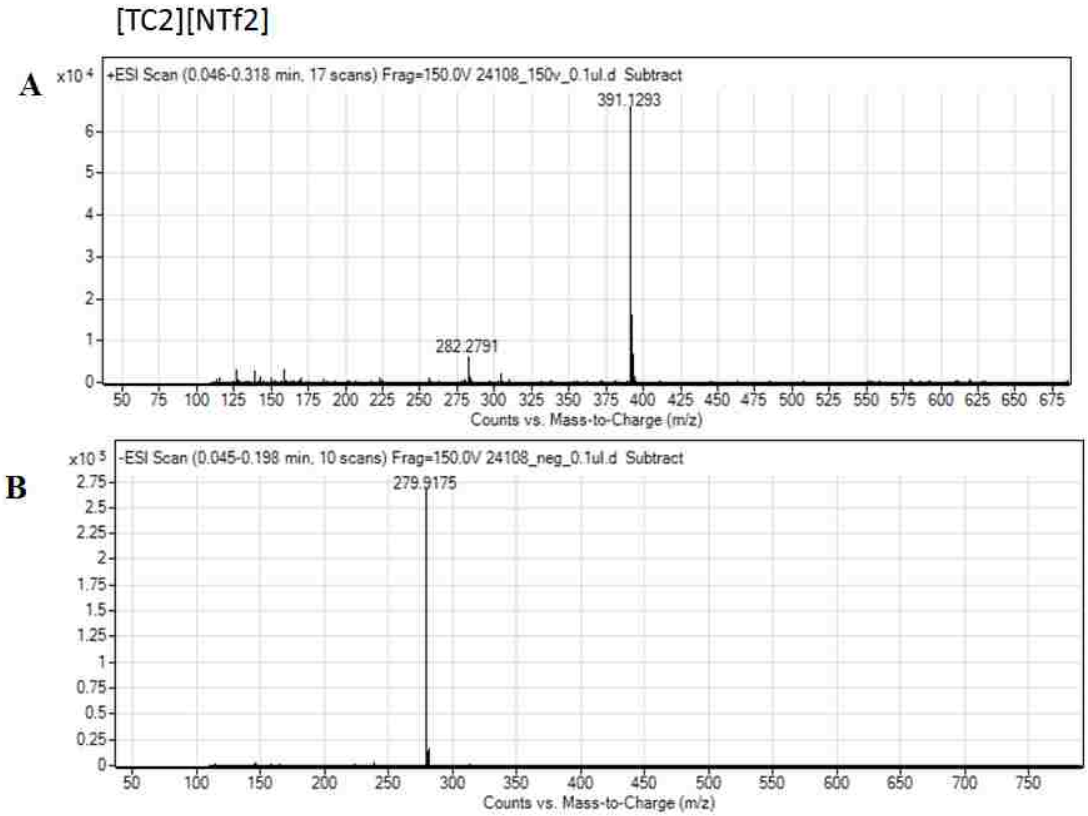

Figure 4. 5. High resolution electrospray ionization mass spectrometry for [TC2][NTf2] positive ion mode (A), negative ion mode (B).

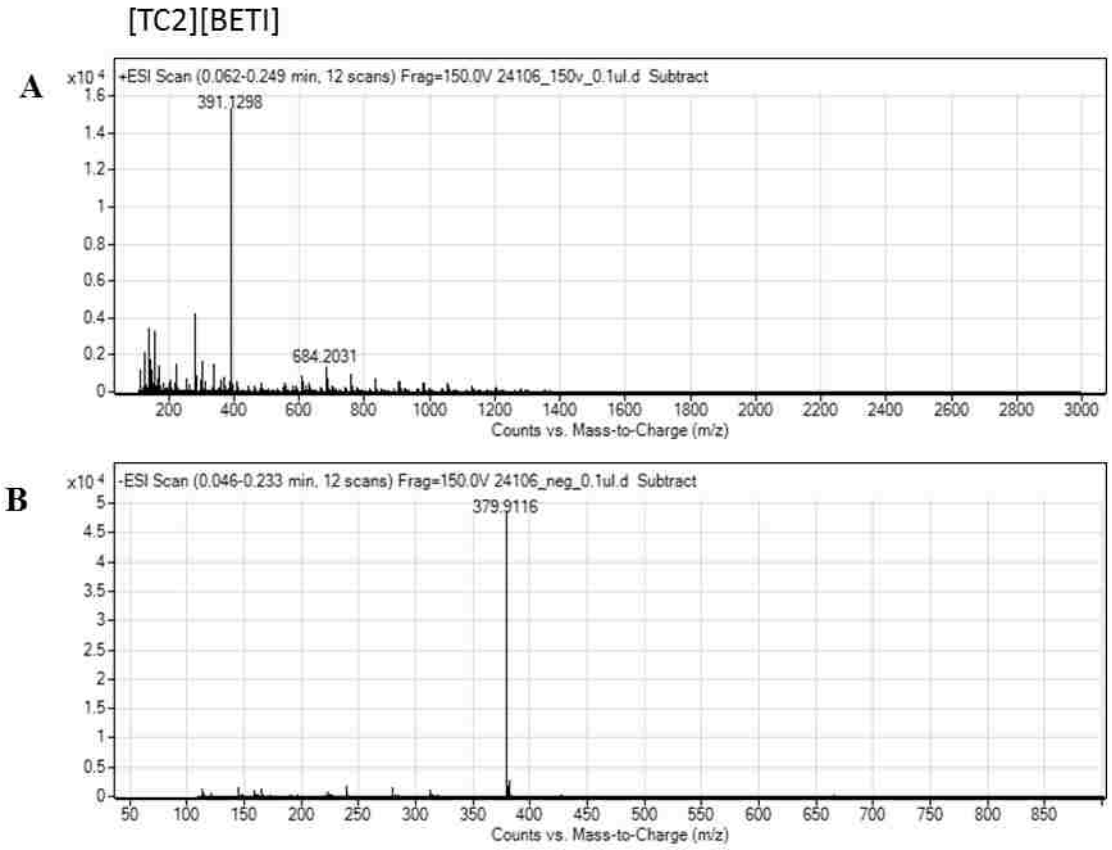

Figure 4. 6. High resolution electrospray ionization mass spectrometry for [TC2][BETI] positive ion mode (A), negative ion mode (B).

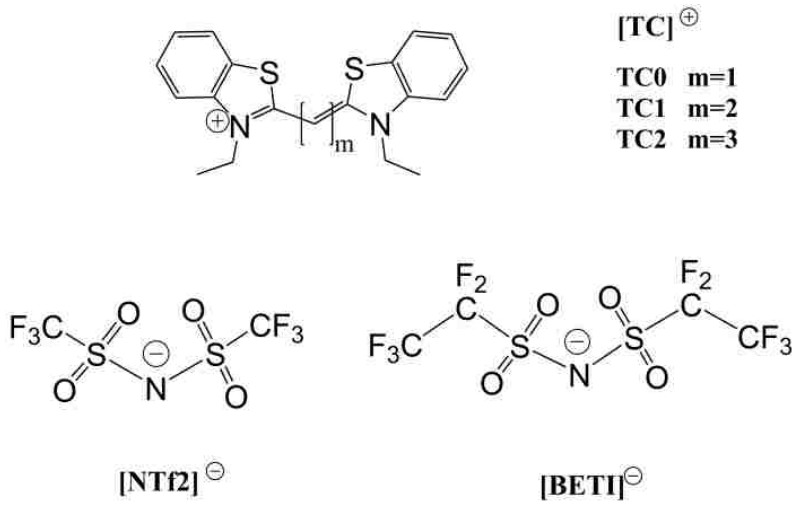

Figure 4. 7. Chemical structures of TC-GMBOS prepared in this study

The relative hydrophobicities of all GUMBOS used in this study were estimated using octanol/water partition coefficient ($K_{O/W}$). The logarithm of $K_{O/W}$ is listed in Table 4.1. As inferred by these log $K_{O/W}$ values, hydrophobicities of these TC GUMBOS increase in the order of [TC2][NTf2] < [TC1][NTf2] < [TC1][BETI] < [TC2][BETI] < [TC0][NTf2] < [TC0][BETI].

Table 4. 1. Molecular weight (MW), yield and log $K_{O/W}$ of TC-GUMBOS

GUMBOS	MW	Yield	Log $K_{O/W}$
[TC0][NTf2]	619.65	98.3%	1.72
[TC0][BETI]	719.66	99.0%	2.04
[TC1][NTf2]	645.69	98.6%	1.59
[TC1][BETI]	745.7	99.3%	1.63
[TC2][NTf2]	671.73	98.8%	1.53
[TC2][BETI]	771.74	99.1%	1.85

These TC-GUMBOS were first dissolved in ethanol, then dispersed into phosphate buffer (pH=7.4) with sonication and allowed to stabilize for 15 min. TEM images were obtained for these aggregations (Figure 4.8). Rod-like [TC0][NTf2] and [TC0][BETI] aggregates with sizes of around (8.13±0.51)×(0.42±0.15) μm and (6.92±0.38)×(1.01±0.10) μm, respectively. TEM images of [TC1][NTf2] and [TC1][BETI] aggregates showed spherical morphologies. The average diameter of [TC1][BETI] aggregates was measured to be 291.3±44.3 nm, while size is not measured for [TC1][NTf2] aggregation due to the blur edge contrast. In the case of [TC2][NTf2] and [TC2][BETI], wire-like morphologies were observed with size of (2.80± 0.38)×(0.12±0.03) μm and (1.88±0.54)×(0.06±0.01) μm, respectively.

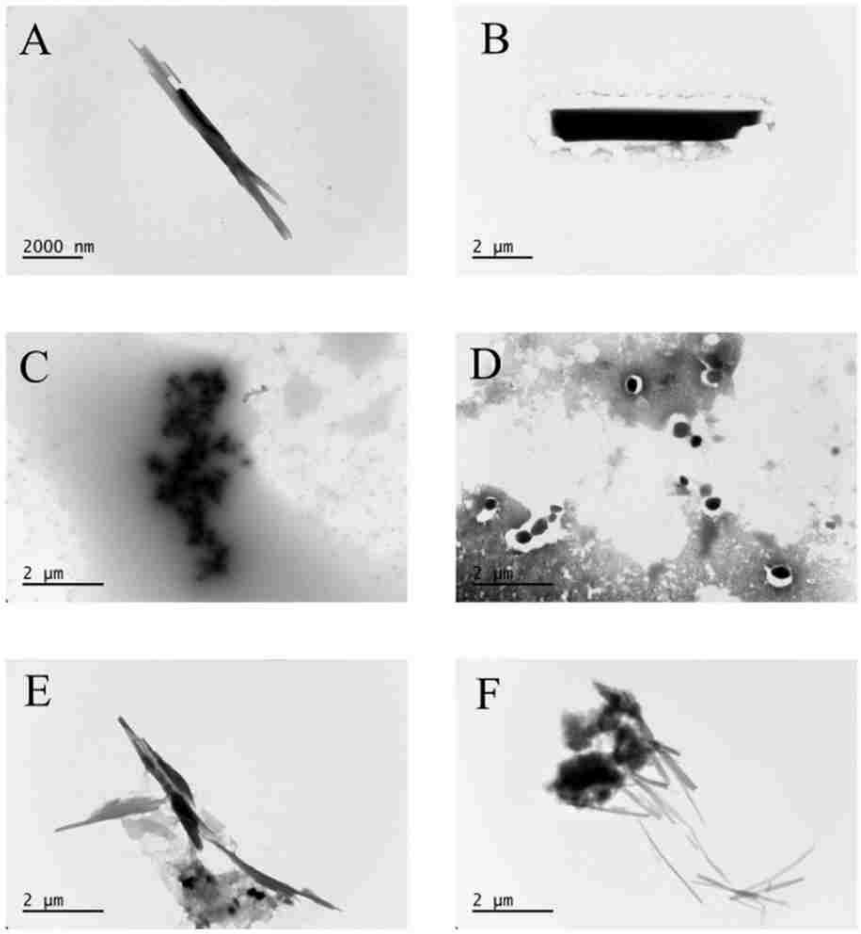

Figure 4. 8. TEM micrograph of TC-GUMBOS aggregation: (A) [TC0][NTf2], (B) [TC0][BETI], (C) [TC1][NTf2], (D) [TC1][BETI], (E) [TC2][NTf2], (F) [TC2][BETI].

4.3.2 Spectral Properties of TC-based GUMBOS

$[NTf2]^-$ and $[BETI]^-$ are non-fluorescent anions that do not absorb light at wavelengths longer than 210 nm. Thus, the spectral properties of these GUMBOS are attributed to the TC cations. Due to the hydrophobicity of the synthesized TC-GUMBOS, ethanol was selected as a solvent for this study. Absorption and emission spectra for all six TC-GUBMOS were recorded at a concentration of 5 µM in ethanol. As shown in Figure 4.9a, the maximum absorbance

wavelengths for $[TC0]^+$, $[TC1]^+$ and $[TC2]^+$ are 423, 555 and 655 nm, respectively, regardless of the anions. However, the alteration of anion has altered the molar absorptivity, to some extent. Figure 4.9b depicts fluorescence emission spectra of these synthesized materials. The excitation wavelengths are their corresponding maximum absorption wavelengths. Emission maxima for $[TC0]^+$, $[TC1]^+$ and $[TC2]^+$ were recorded at 483, 572 and 672 nm, respectively.

As fluorescence sensors, photostability is an important characteristic of interest. Photostabilities of the synthesized TC-GUMBOS were monitored over a 3600 second time period using fluorescence kinetic measurements (Figure 4.10). $[TC0]^+$, $[TC1]^+$ and $[TC2]^+$ were exited at 423, 550 and 645 nm, respectively. Emission was monitored at 483 nm for $[TC0]^+$, 572 nm for $[TC1]^+$ and 672 nm for $[TC2]^+$. These six GUMBOS were found to be extremely photostable over this experiment period with negligible photodegradation observed.

Absorbance spectra of TC-GUMBOS aggregations in phosphate buffer (pH=7.4) are displayed in Figure 4.11. In comparison with their ethanol solutions, [TC0]-GUMBOS buffer dispersions exhibit same absorption maxima at 423 nm, while relatively higher shoulders at 402 nm attributed to H-aggregation are observed (Figure 4.11a). Absorption spectra for [TC1][NTf2] and [TC1][BETI] buffer dispersions show second peaks at 615 nm and 650nm, respectively, representative of J-aggregation (Figure 4.11b). In the case of [TC2][NTf2] and [TC2][BETI], absorption spectra of these aggregates exhibit blue-shifted peaks centered at higher energy and attributed to H-aggregation (Figure 4.11c). Buffer dispersion of TC0-GUMBOS, TC1-GUMBOS

and TC2-GUMBOS were excited at 423, 541, and 645 nm, respectively. Emission spectra of these compounds are depicted in Figure 4.11d, showing emission maxima at 476, 488, 565, and 665 nm for [TC0][NTf2], [TC0][BETI], TC1-GUMBOS and TC2-GUMBOS, respectively.

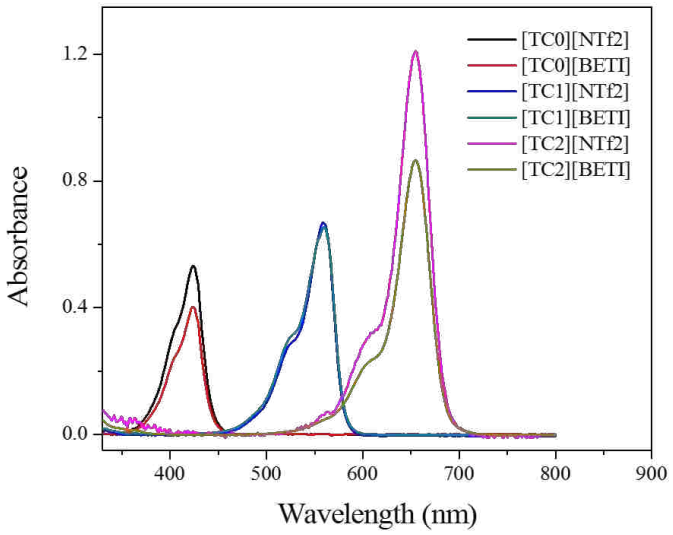

A

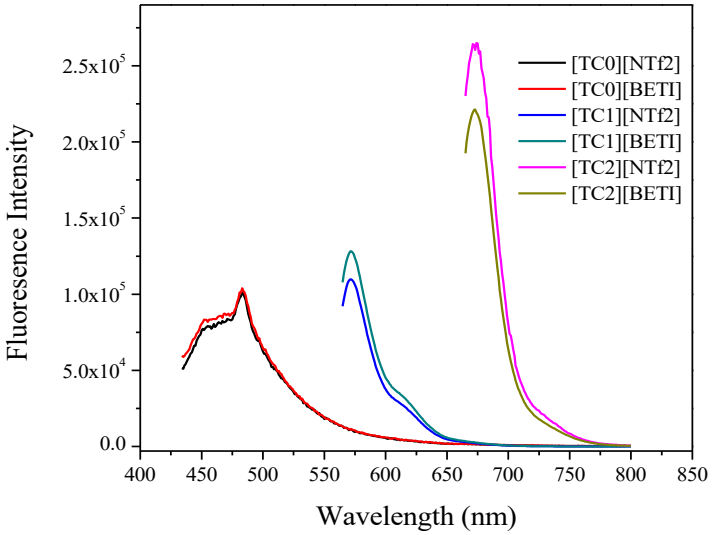

B

Figure 4. 9. UV-Vis (A) and fluorescence (B) spectra of TC-GUMBOS in ethanol at a concnetration of 5 μM.

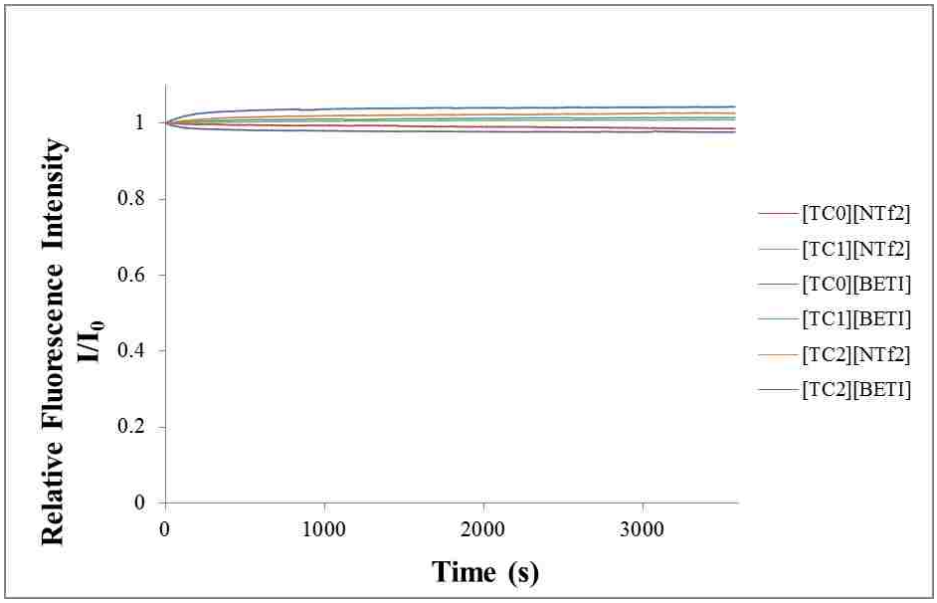

Figure 4. 10. Photostability of GUMBOS monitored for 3600 s using fluorescence spectroscopy

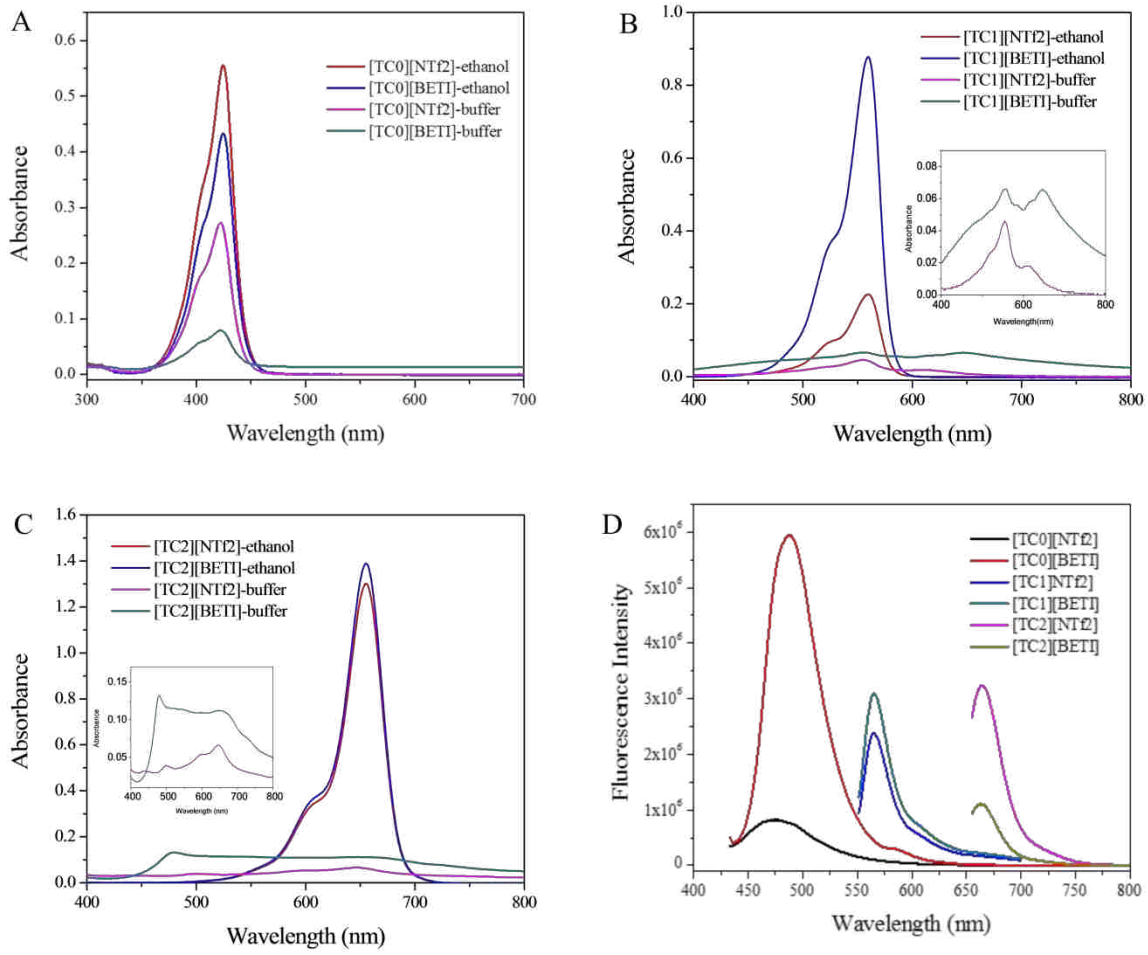

Figure 4. 11. UV-Vis spectra of 5 μM (A) [TC0]-GUMBOS, (B) [TC1]-GUMBOS and (C) [TC2]-GUMBOS suspended in phosphate buffer (pH=7.4), and their 5 μM ethanol solution, respectively; D is the fluorescence spectra of 5 μM TC-GUMBOS suspended in buffer via reprecipitation method.

4.3.3 Discrimination of Proteins Using TC-GUMBOS

Seven proteins that have diverse molecular weight (MW), metal/non-metal containing properties, and isoelectric points (pI) were selected as sensing targets (Table 4.2). Among the seven selected proteins, HSA, IgG, Trans and Fib are the top four abundant proteins in human

serum,[41] while Hb, Cyt-c and Lys are non-serum proteins.

Table 4. 2. Pysical properties of selected proteins.

Proteins	pI value	MW (kDa)
Human Serum Albumin (HSA)	5.3	66.5
Transferrin (Trans)	5.6	80
Fibrinogen (Fib)	5.6	340
Hemoglobin (Hb)	6.9	64.5
Immunoglobulin G (IgG)	7.5-7.8	150
Cytochrome-C (Cyt-c)	10.7	12
Lysozyme (Lys)	11.3	14.3

Figure 4.12 is a comparison of the sensor response in the presence of different proteins at 0.5 μg/mL. As shown in Figure 4.12, for the same sensor, the presence of different proteins varied the fluorescence response. In contrast, in the presence of the same protein, the fluorescence response depends on different TC-GUMBOS sensors. The distinct response patterns suggest the feasibility of protein discrimination using this method.

In order to further validate the ability of this sensor array to discriminate proteins, the pattern responses were then subjected to multivariate statistical analyses, specifically, principal component analysis (PCA) and linear discriminant analysis (LDA). Both PCA and LDA are statistical techniques commonly used for dimensionality reduction. PCA is “unsupervised”, as it ignores class labels, while LDA is a “supervised” technique and computes the linear discrimination factors that maximize the separation between multiple classes. [42, 43] A method combining PCA and LDA was used here. This PCA-plus-LDA method has been verified as effective and capable of addressing computational difficulties caused by high-dimensionality and

avoid over-fitting. [44-47] In this method, we first transformed our fluorescence responses ($^{I}/_{I_0} - 1$) into principal component scores.

For seven proteins at 0.5 μg/mL, the first three principal components created by PCA accounted for 99.32% of the overall variability given by the 252 observations. Then the first three principal components were used as input variables of LDA. These patterns were finally transformed to canonical score plots, which were visible as well clustered groups (Figure 4.13). The classification accuracy was calculated to be 100%. If not specified, the following LDAs were conducted after PCA and using the first three principal components as input variables.

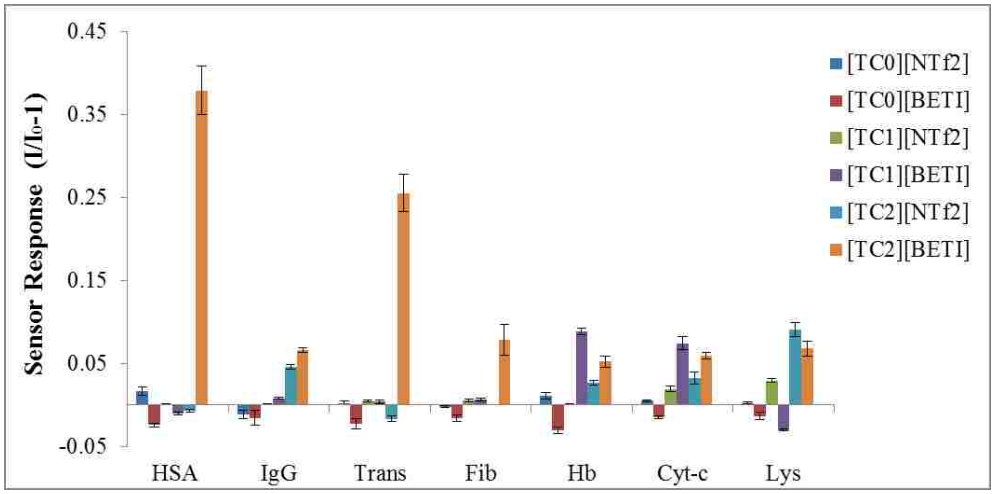

Figure 4. 12. Array-based sensing of seven proteins at 0.5 μg/mL in pH 7.4 phosphate buffer. Error bars represent standard deviations of six replicate samples. $[TC0]^+$, $[TC1]^+$ and $[TC2]^+$ aggregates were excited at 423, 541, and 645 nm, respectively. Their corresponding emission intensities were recorded at 488, 565, and 665 nm.

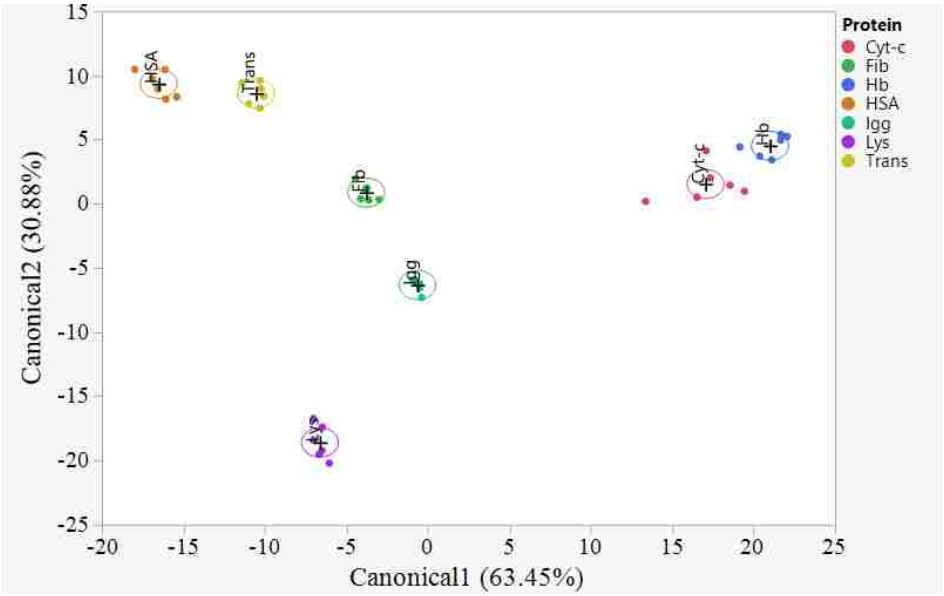

Figure 4. 13. Canonical score plot for the response patterns as obtained from PCA-plus-LDA for seven proteins at 0.5 µg/mL.

Lower protein concentrations were tested to evaluate the ability of this sensor array to discriminate proteins at trace levels. The sensor responses obtained from seven proteins at 0.1 µg/mL were used to perform pattern analysis and PCA-plus-LDA. As shown in Figure 4.14a, the relative deviations of the responses become lager at such a low protein concentration. Figure 4.14b depicts successful clustere of these proteins into groups, while Hb and Cyt-c have overlapped confidence ellipses. The discriminant scores suggest that one Hb sample is misclassified as Cyt-c, and three Cyt-c samples are misclassified as Hb. This resulted in a 9.5% misclassification. The reason for this phenomenon is probably due to the similarity of these two proteins, as they both contain heme groups.

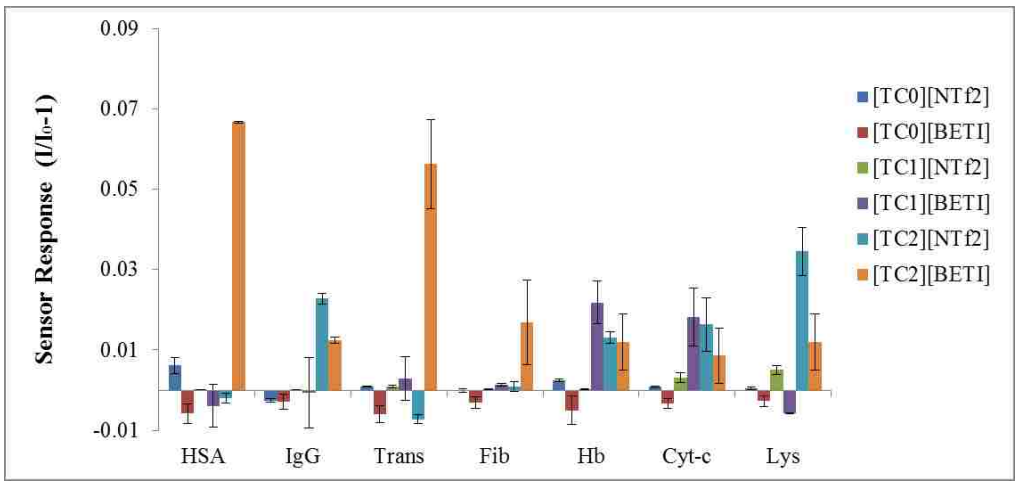

A

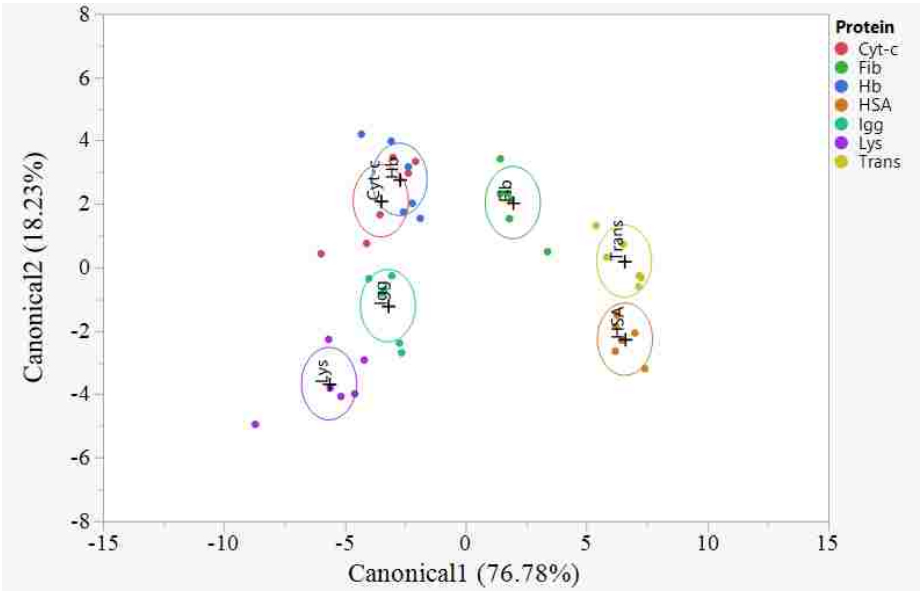

B

Figure 4. 14. Array-based sensing of seven potiens at 0.1 µg/mL: (A) response pattern obtained from the six sensor elements; (B) canonical score plot obtained using LDA with 95% confidence ellipses.

In order to study the sensor response with respect to protein concentration, different protein concentrations (0.1 - 20 µg/mL) were tested using this sensor array (Figure 4.15). The

compounds, [TC1][NTf2] and [TC2][BETI], exhibited positive responses toward all seven proteins. In contrast, [TC0][NTf2] exhibited negative responses toward IgG; [TC0][BETI] exhibited negative responses toward all seven proteins; The compound [TC1][BETI] showed negative responses toward HSA and Lys; [TC2][NTf2] showed negative responses toward HSA and Trans. These features remained consistent over a protein concentration range of 0.1 - 20 μg/mL and were enhanced with higher concentrations. As illustrated in Figure 4.16, for each protein, the tested nine concentrations were grouped into nine isolated clusters in LDA plots. Discriminant accuracies were calculated to be 100% for HSA, Trans, Hb, Cyt-c, IgG, and Lys. Since an 8 μg/mL Fib sample was misclassified as a 10 μg/mL sample, the discriminant accuracy for Fib was 98.15%. This suggests the feasibility of this sensor array for protein quantification. Since the first discriminant canonicals (Canonical 1) produced over 99% variance, it is reasonable to use Canonical 1 for protein quantification. A linear relationship between Canonical 1 and protein concentrations was observed and illustrated in Figure 4.16 b, d, f, h, j, l, and n.

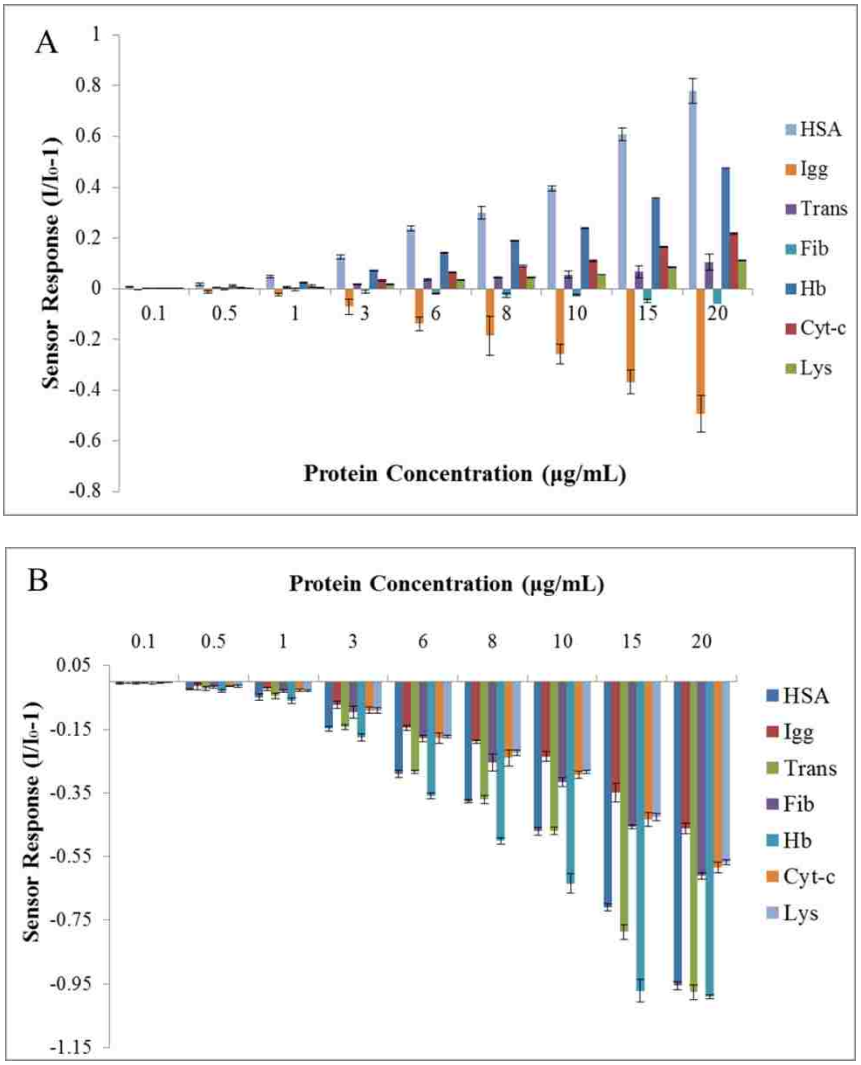

Figure 4. 15. Sensing responses toward seven proteins at 9 concentrations (0.1 - 20 µg/mL): (A) [TC0][NTf2]; (B) [TC0][BETI]; (C) [TC1][NTf2]; (D) [TC1][BETI]; (E) [TC2][NTf2]; (F) [TC2][BETI]. (figure cont'd)

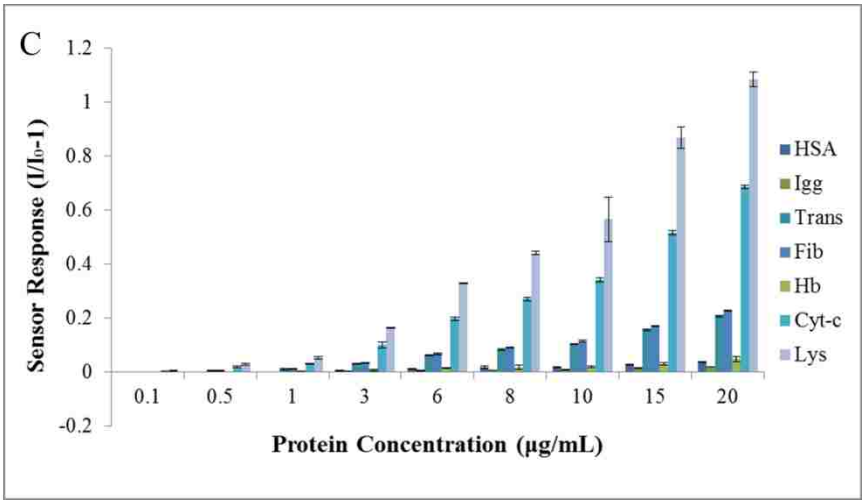
C
1.2
1
0.8
0.6
0.4
0.2
0
-0.2
Sensor Response (I/I0-1)
0.1
0.5
1
3
6
8
10
15
20
Protein Concentration (µg/mL)
HSA
Igg
Trans
Fib
Hb
Cyt-c
Lys

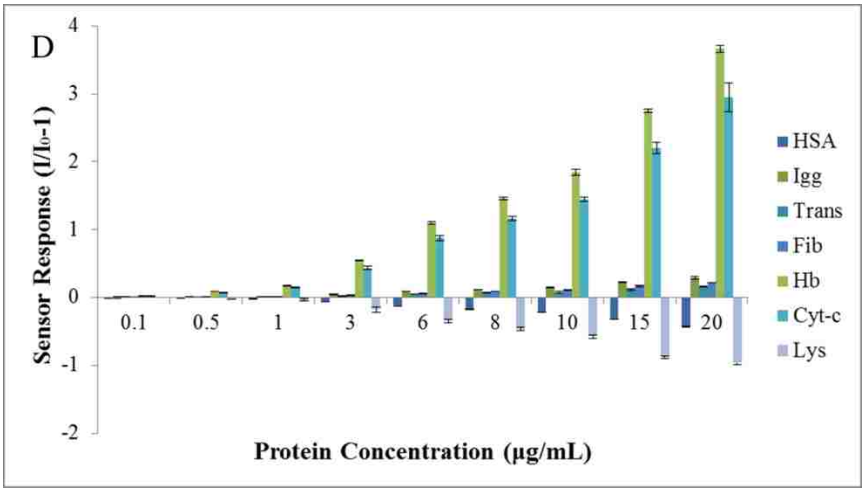
D
4
3
2
1
0
-1
-2
Sensor Response (I/I0-1)
0.1
0.5
1
3
6
8
10
15
20
Protein Concentration (µg/mL)
HSA
Igg
Trans
Fib
Hb
Cyt-c
Lys

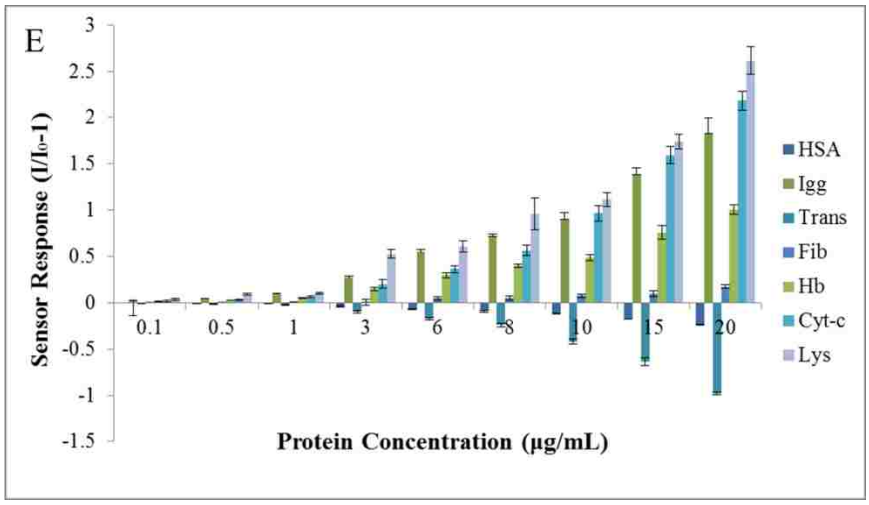
E
3
2.5
2
1.5
1
0.5
0
-0.5
-1
-1.5
Sensor Response (I/I0-1)
0.1
0.5
1
3
6
8
10
15
20
Protein Concentration (µg/mL)
HSA
Igg
Trans
Fib
Hb
Cyt-c
Lys

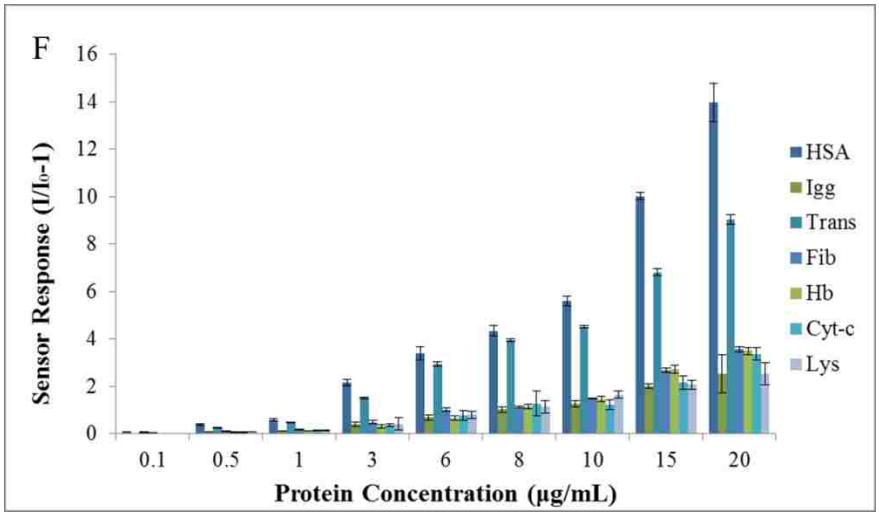
F
Sensor Response (I/I0-1)
16
14
12
10
8
6
4
2
0
0.1
0.5
1
3
6
8
10
15
20
Protein Concentration (µg/mL)
HSA
Igg
Trans
Fib
Hb
Cyt-c
Lys

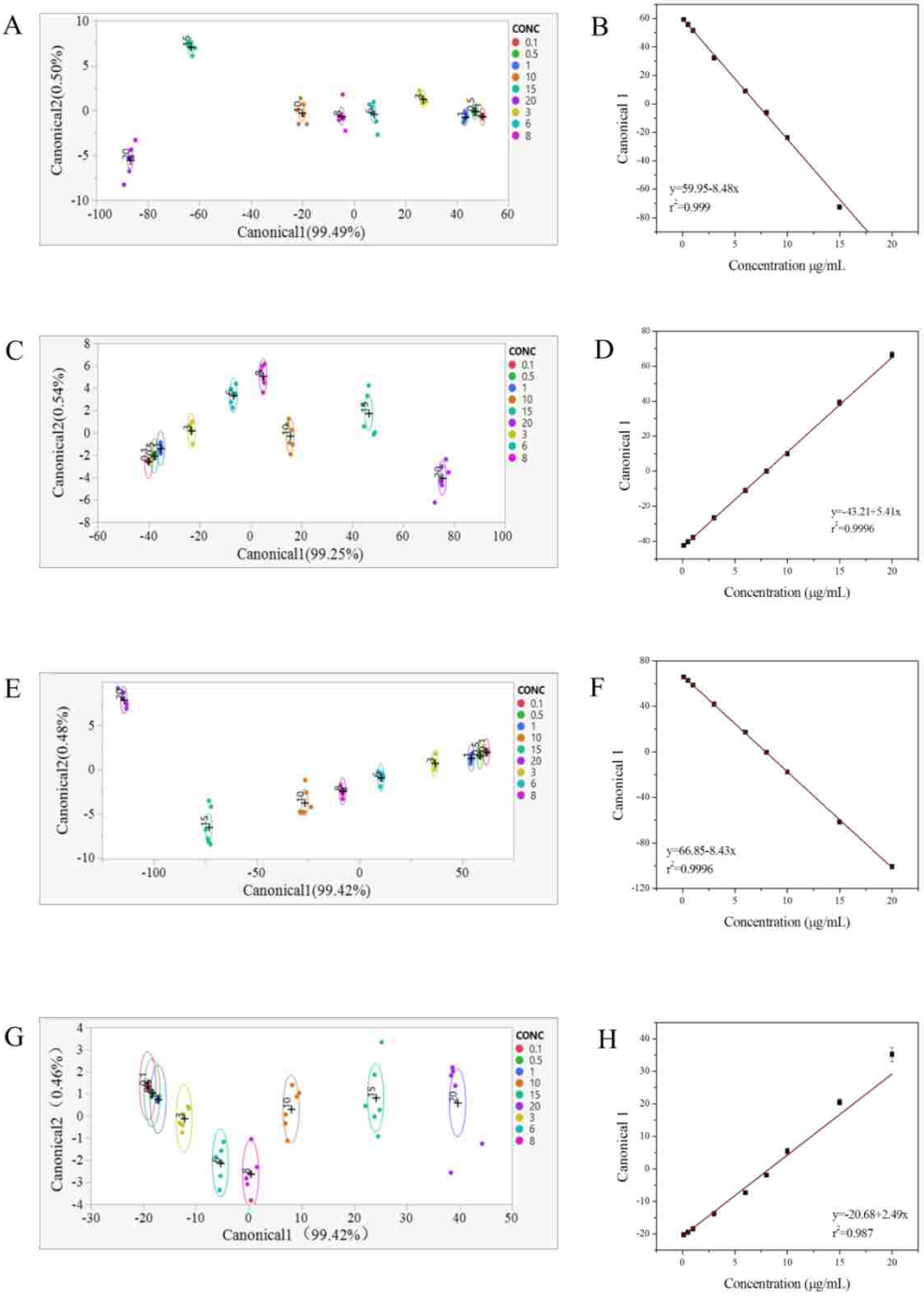

Figure 4. 16. Canonical score plot for fluorescence responses patterns obtained with the sensor array against different concentrations of (A) HSA, (C) Trans, (E) Hb, (G) Cyt-c, (I) IgG, (K) Lys, and (M) Fib; Plot of the first discriminant canonical vs. protein concentrations (0.1, 0.5, 1, 3, 6, 8, 10, 15 and 20 μg/mL): (B) HSA, (D) Trans, (F) Hb, (H) Cyt-c, (J) IgG, (L) Lys, (N) Fib. (figure cont'd)

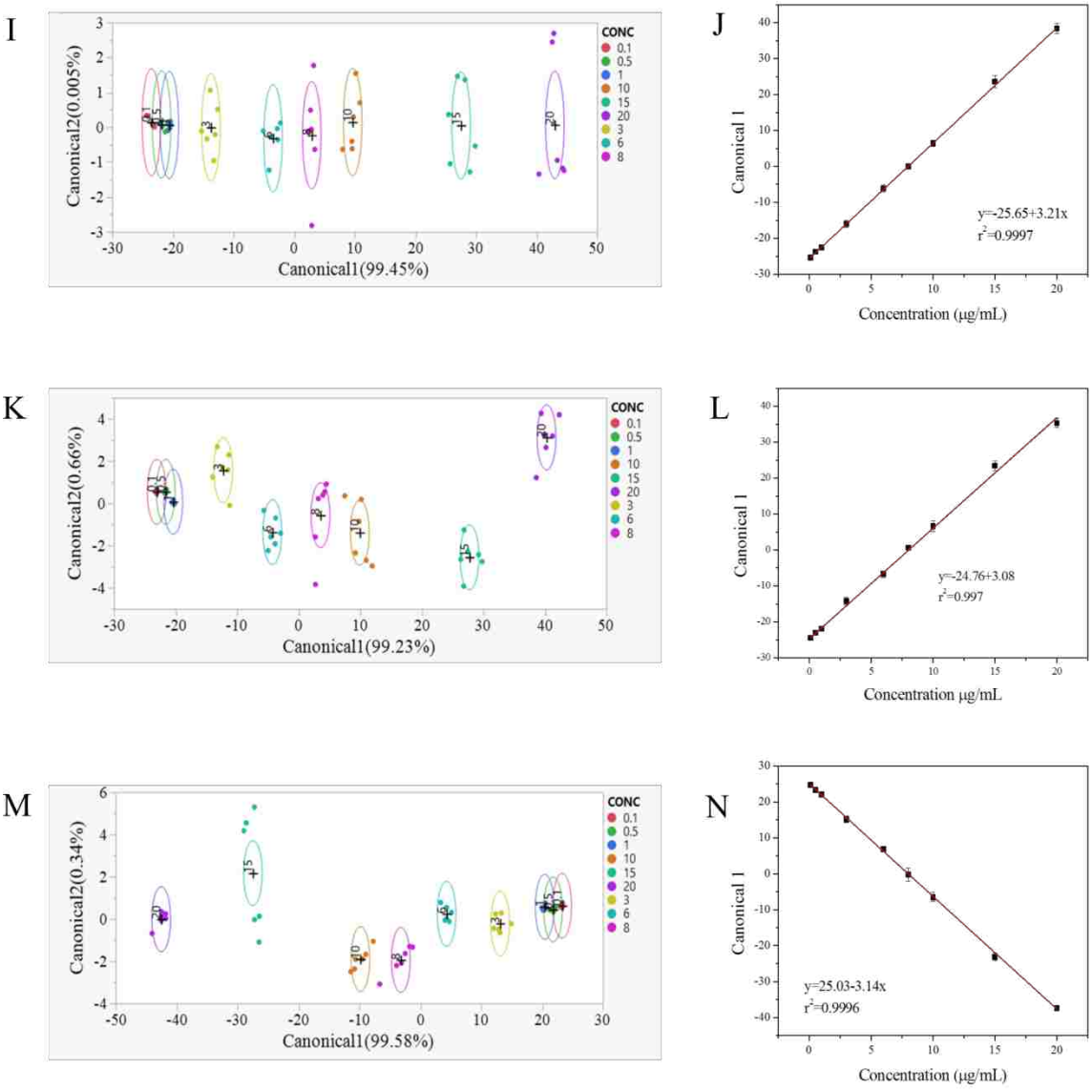

In order to evaluate the ability of this sensor array to discriminate proteins regardless of protein concentration, sensor array responses toward HSA and Hb over a range of 0.1 - 20 μg/mL were used to perform new PCA-plus-LDA. The 648 observations (2 proteins × 9 protein concentrations × 6 sensor elements × 6 replicates) involved in this experiment were first used to conduct PCA. The first two principal components accounted for 98.9% of the variance, and were

used as input variables for LDA (Figure 4.17). The discriminant scores showed 94.5% discriminant accuracy, attributing to misclassification of the six 0.1 µg/mL HSA samples. Furthermore, in order to investigate the feasibility of this sensor array for discrimination of similar protein mixtures, we conducted experiments using HSA and Hb using various weight ratios (100% HSA, 80% HSA + 20% Hb, 60% HSA + 40% Hb, 40% HSA + 60% Hb, 20% HSA + 80% Hb, and 100% Hb).The total concentration was 5 µg/mL. As illustrated in the LDA plot, Figure 4.18, HSA and Hb mixtures with various ratios were well discriminated with a discriminant accuracy of 100%.

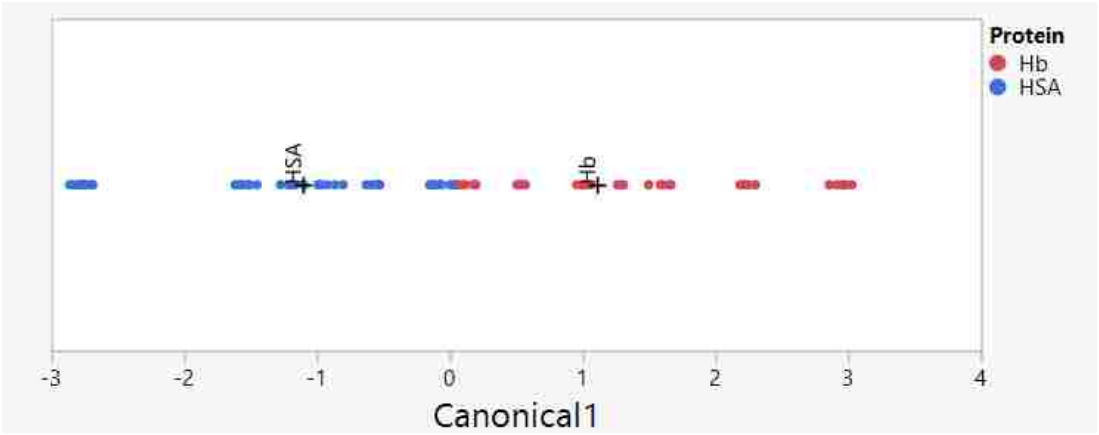

Figure 4. 17. Canonical score plot fof discrimination of HSA and Hb at nine concentrations over a range of 0.1 - 20 µg/mL.

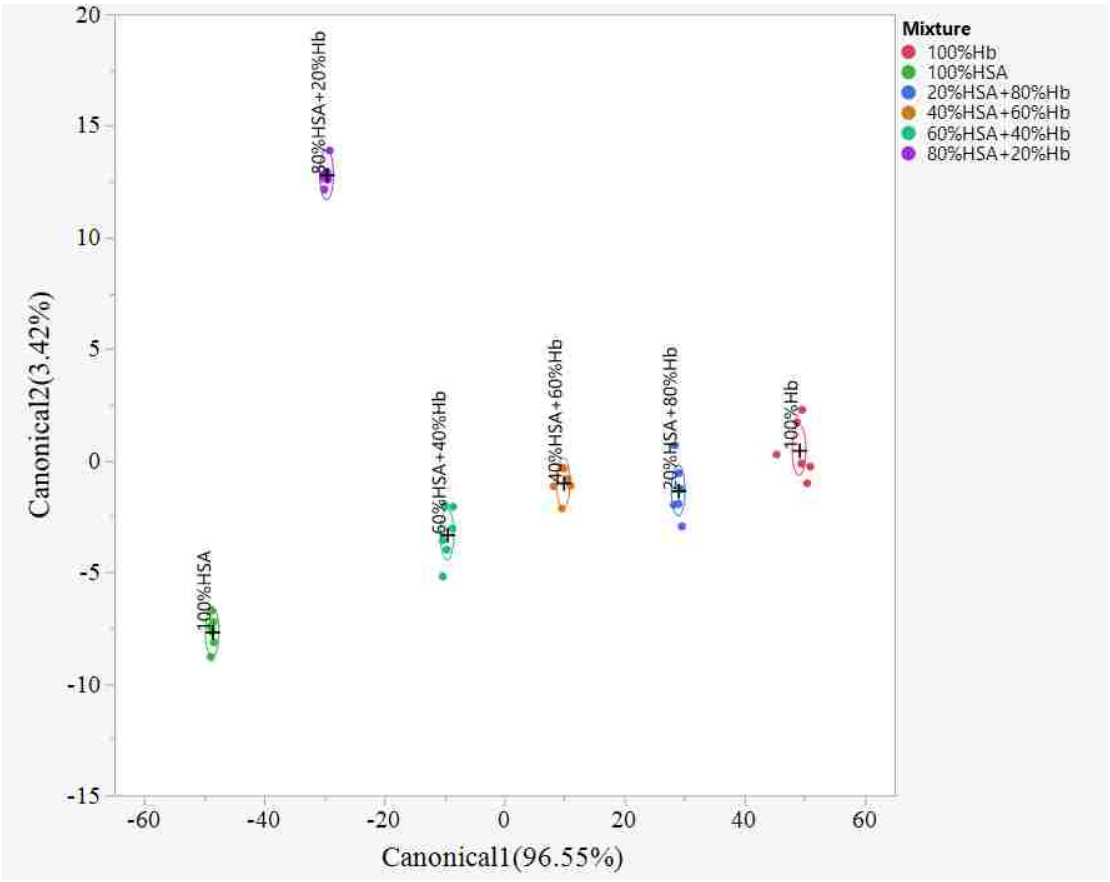

Figure 4. 18. Canonical score plot for discrimination of HSA, Hb, and their mixtures at 5 μg/mL.

4.3.4 Discussion of the possible sensing mechanism

Spectral properties of PD are highly dependent on the surrounding media. [48, 49] In recent decades, studies of noncovalent interactions between PD and biomolecules have produced great interest. [37, 50-54] We hypothesize that noncovalent interactions occur in the sensing process between TC-GUMBOS and the tested proteins, which results in variation of aggregation type, rotational/stretching motion, etc. Among these effects, we believe that formation of differenttypes of aggregaties is the major driving force for emission change. The absorption and

emission spectra of the six sensor elements with different proteins are depicted in Figure 4.19. It is well known that H-aggregation of polymethine dyes causes non-radiative decay, which will lead to decreased emission. [55, 56] As an example, the [TC2][BETI] sensor element gave positive responses toward all seven proteins. As observed inFigure 4.19k, in the presence of proteins, the intensity of H-aggregation absorption at 476 nm decreased and the monomer absorption peak at 655 nm amplified. The fluorescence spectra (Figure 4.19l) showed increased fluorescence emission of [TC2][BETI] as proteins were introduced into the system. Conversely, fluorescence emission of [TC0][BETI] decreased as proteins were incorporated (Figure 4.19d). This is attributed to the formation of H-aggregation in the presence of proteins, which is verified using absorption spectra as shown in Figure 4.19c, where blue-shifted peaks were observed as proteins were introduced. In addition, H-aggregates exhibit a red shift of the emission spectrum and remarkably lower fluorescence intensity (Figure 4.19d). Similarly, the sensing phenomenon of [TC0][NTf2], [TC1][BETI] and [TC2][NTf2] can be explained using such theory (Figure 4.19a, b, g-j).

The [TC1][NTf2] GUMBOS showed positive responses toward all seven proteins; however, this phenomenon cannot be explained using the decay of H-aggregation. The absorption spectra (Figure 4.19e) shows that [TC1][NTf2] does not form H-aggregates. Instead, a red-shifted peak was observed at 610 nm, which is attributed to the absorption of J-aggregates. In the presence of proteins, both the absorption peak of the monomer at 555 nm and the shoulder peak of

J-aggregates increased. The emission spectra confirmed formation of J-aggregates with a red-shifted emission peak at 638 nm. Interestingly, emission intensity of the monomer increased with addition of proteins as well. This is probably due to formation of a dye monomer-protein complex, which would restrict intramolecular rotational motion. The intramolecular rotational motions of the flexible polymethine chain in TC dyes would lead to rapid non-radiative decay. [37, 57] As a result, noncovalent interactions (e.g. hydrogen bonding, hydrophobic interaction, and electrostatic attraction) with proteins are very likely to stabilize TC dyes and restrict the non-radiative decay caused by rotation and twist, and hence increase the quantum yield of these TC dyes. [58] Thus, we hypothesize that the slightly red-shifted monomer absorption peak (Figure 4.19e) is also due to noncovalent interactions between dye monomer and protein.

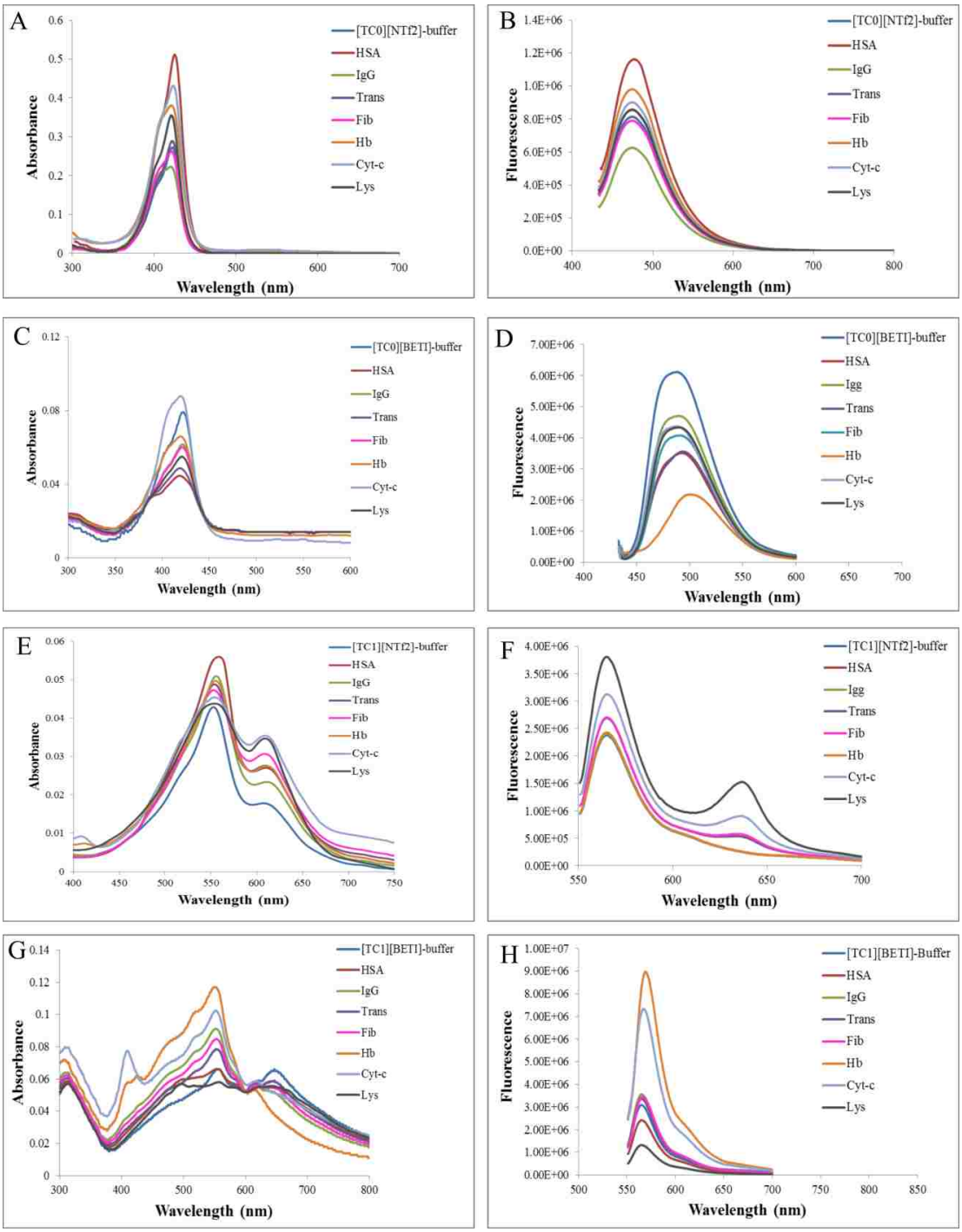

Figure 4. 19. Absorption and emission spectral of TC-GUMBOS suspended in buffer with different proteins at 10 µg/mL. Absorption spectra: (A) [TC0][NTf2]; (C) [TC0][BETI]; (E) [TC1][NTf2]; (G) [TC1][BETI]; (I) [TC2][NTf2]; (K) [TC2][BETI]. Emission spectra: (B) [TC0][NTf2]; (D) [TC0][BETI]; (F) [TC1][NTf2]; (H) [TC1][BETI]; (J) [TC2][NTf2]; (L) [TC2][BETI]. (figure cont'd)

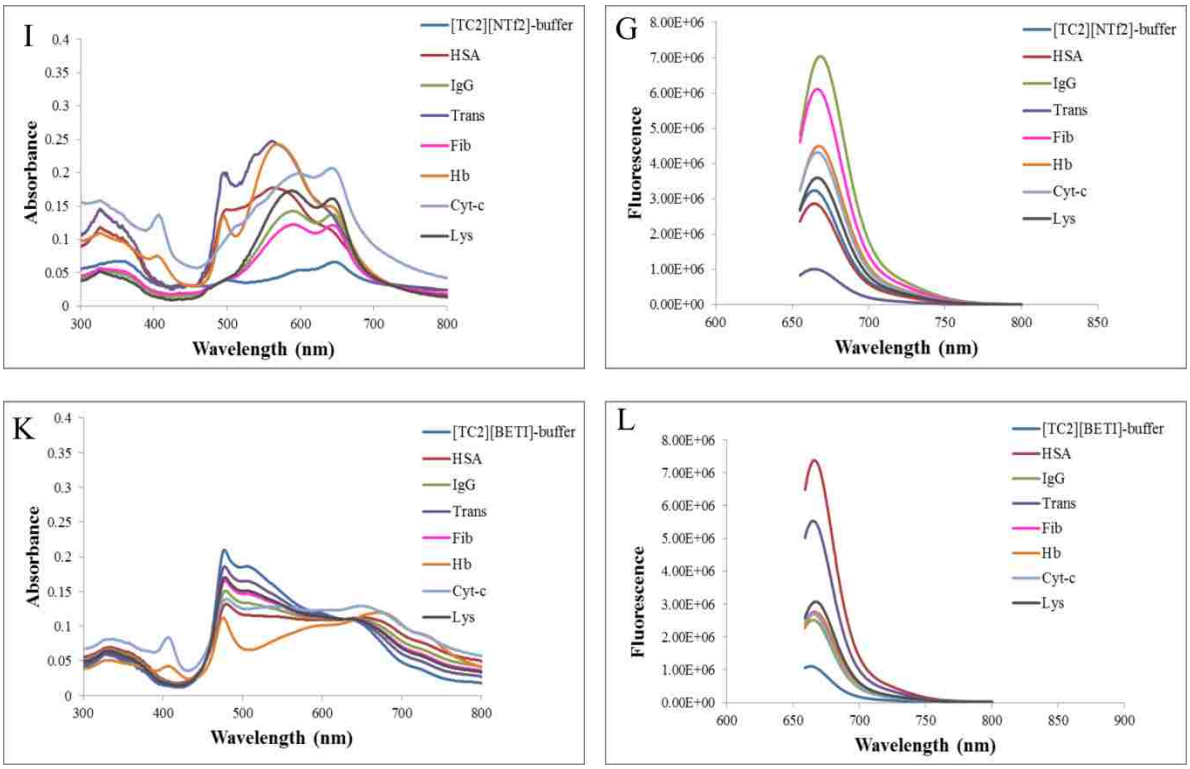

4.3.5 Protein discrimination in urine

In order to further explore the application of this sensor array to more complex real samples, artificial urine that contains various organic and inorganic salts was used as media for discrimination of the seven proteins at 5 μg/mL. As shown in Figure 4.20, a three-dimensional canonical score plot indicates that this sensor array is suitable for discrimination of the seven proteins in urine sample, providing seven different clusters without overlap. Discriminant accuracy was calculated to be 100%. These results indicate that this fluorescence sensor array is able to discriminate proteins in urine at low concentrations.

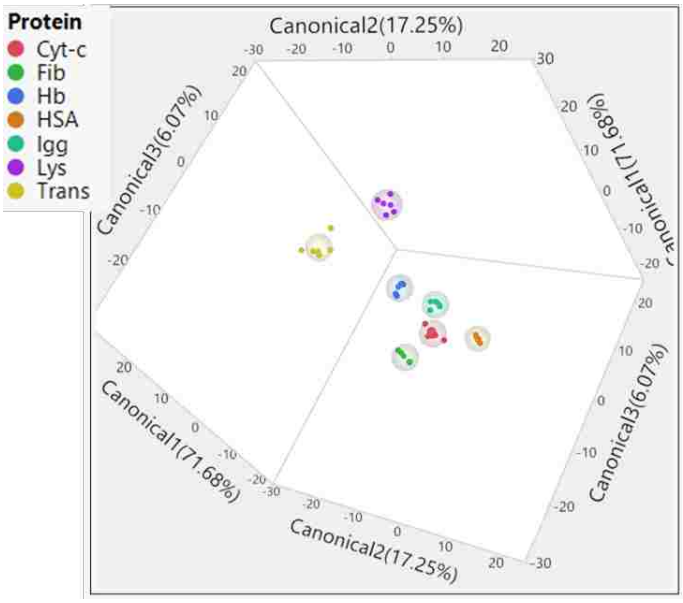

Figure 4. 20. Canonical score plot for discrimination of the seven proteins in artificial urine

4.4 Conclusion

In this study, we have developed a rapid and effective fluorescence sensor array for protein discrimination. This sensor array was constructed using a series of TC-based GUMBOS, which were easily synthesized through a simple ion exchange method. The variation of TC-GUMBOS aggregation due to noncovalent interaction with proteins was believed to be the major driving force for fluorescence protein sensing. Other noncovalent interactions also play indispensable roles, such as TC molecular rotation restriction. It has been successfully demonstrated that this sensor array was capable of discriminating proteins at concentrations as low as 0.1 µg/mL with high accuracy. In addition, a linear relationship was observed between the first canonical score and protein concentration, providing the potential of protein quantification using this sensor array. Furthermore, seven proteins spiked in artificial urine were successfully identified at 0.5 µg/mL

with 100% discriminant accuracy. In comparison with previously reported protein sensor arrays, this TC-GUMBOS-based fluorescence sensor array provides favorable discriminant accuracy at a much lower protein concentration. [10, 11, 16, 59, 60] Thus, we believe that this TC-GUMBOS-based sensor array has great potential for highly sensitive and accurate medical diagnosis, as well as for discrimination of other biomolecules.

4.5 References

1. Hornbeck PV. Enzyme‐linked immunosorbent assays. *Current protocols in immunology.* 2015;110(1):2.1. 1-2.1. 23.

2. Ambrosi A, Airo F, Merkoçi A. Enhanced gold nanoparticle based ELISA for a breast cancer biomarker. *Analytical chemistry.* 2009;82(3):1151-1156.

3. Ikeda T. Protein A immunocapture assay detecting antibodies to fluke cysteine proteinases for immunodiagnosis of human paragonimiasis and fascioliasis. *Journal of helminthology.* 2001;75(3):245-249.

4. Butler JE. Enzyme-linked immunosorbent assay. *Journal of immunoassay.* 2000;21(2-3):165-209.

5. Jia C-P, Zhong X-Q, Hua B, et al. Nano-ELISA for highly sensitive protein detection. *Biosensors and Bioelectronics.* 2009;24(9):2836-2841.

6. Dille BJ, Surowy TK, Gutierrez RA, et al. An ELISA for detection of antibodies to the E2 protein of GB virus C. *Journal of Infectious Diseases.* 1997;175(2):458-461.

7. De M, Rana S, Akpinar H, et al. Sensing of proteins in human serum using conjugates of nanoparticles and green fluorescent protein. *Nature chemistry.* 2009;1(6):461-465.

8. Miranda OR, You C-C, Phillips R, et al. Array-based sensing of proteins using conjugated polymers. *Journal of the American Chemical Society.* 2007;129(32):9856-9857.

9. Galpothdeniya WIS, Fronczek FR, Cong M, Bhattarai N, Siraj N, Warner IM. Tunable GUMBOS-based sensor array for label-free detection and discrimination of proteins. *Journal of Materials Chemistry B.* 2016;4(8):1414-1422.

10. Niamnont N, Mungkarndee R, Techakriengkrai I, Rashatasakhon P, Sukwattanasinitt M. Protein discrimination by fluorescent sensor array constituted of variously charged dendritic phenylene–ethynylene fluorophores. *Biosensors and Bioelectronics.* 2010;26(2):863-867.

11. Kong H, Liu D, Zhang S, Zhang X. Protein sensing and cell discrimination using a sensor array based on nanomaterial-assisted chemiluminescence. *Analytical chemistry.* 2011;83(6):1867-1870.

12. Bunz UH, Rotello VM. Gold nanoparticle–fluorophore complexes: sensitive and discerning "noses" for biosystems sensing. *Angewandte Chemie International Edition.* 2010;49(19):3268-3279.

13. Shahrajabian M, Hormozi-Nezhad MR. Design a New Strategy Based on Nanoparticle-Enhanced Chemiluminescence Sensor Array for Biothiols Discrimination. *Scientific reports.* 2016;6:32160.

14. Bigdeli A, Ghasemi F, Golmohammadi H, et al. Nanoparticle-based optical sensor arrays. *Nanoscale.* 2017;9(43):16546-16563.

15. Saha K, Agasti SS, Kim C, Li X, Rotello VM. Gold nanoparticles in chemical and biological sensing. *Chemical reviews.* 2012;112(5):2739-2779.

16. Wei X, Wang Y, Zhao Y, Chen Z. Colorimetric sensor array for protein discrimination based on different DNA chain length-dependent gold nanoparticles aggregation. *Biosensors and Bioelectronics.* 2017;97:332-337.

17. Ramanathan M, Patil M, Epur R, et al. Gold-coated carbon nanotube electrode arrays: Immunosensors for impedimetric detection of bone biomarkers. *Biosensors and Bioelectronics.* 2016;77:580-588.

18. You C-C, Miranda OR, Gider B, et al. Detection and identification of proteins using nanoparticle–fluorescent polymer 'chemical nose'sensors. *Nature nanotechnology.* 2007;2(5):318.

19. Gooding JJ, Wibowo R, Liu J, et al. Protein electrochemistry using aligned carbon nanotube arrays. *Journal of the American Chemical Society.* 2003;125(30):9006-9007.

20. Chen RJ, Choi HC, Bangsaruntip S, et al. An investigation of the mechanisms of electronic sensing of protein adsorption on carbon nanotube devices. *Journal of the American Chemical Society.* 2004;126(5):1563-1568.

21. Landry MP, Ando H, Chen AY, et al. Single-molecule detection of protein efflux from microorganisms using fluorescent single-walled carbon nanotube sensor arrays. *Nature nanotechnology.* 2017;12(4):368.

22. Zhou H, Baldini L, Hong J, Wilson AJ, Hamilton AD. Pattern recognition of proteins based on an array of functionalized porphyrins. *Journal of the American Chemical Society.* 2006;128(7):2421-2425.

23. Kubota R, Hamachi I. Protein recognition using synthetic small-molecular binders toward optical protein sensing in vitro and in live cells. *Chemical Society Reviews.* 2015;44(13):4454-4471.

24. Tesfai A, El-Zahab B, Bwambok DK, et al. Controllable formation of ionic liquid micro-and nanoparticles via a melt–emulsion–quench approach. *Nano letters.* 2008;8(3):897-901.

25. Kirstein S, Daehne S. J-aggregates of amphiphilic cyanine dyes: Self-organization of artificial light harvesting complexes. *International Journal of Photoenergy.* 2006;2006.

26. Würthner F, Kaiser TE, Saha‐Möller CR. J‐Aggregates: From Serendipitous Discovery to Supramolecular Engineering of Functional Dye Materials. *Angewandte Chemie International Edition.* 2011;50(15):3376-3410.

27. Bricks JL, Slominskii YL, Panas ID, Demchenko AP. Fluorescent J-aggregates of cyanine dyes: basic research and applications review. *Methods and applications in fluorescence.* 2017;6(1):012001.

28. Chowdhury A, Wachsmann-Hogiu S, Bangal PR, Raheem I, Peteanu LA. Characterization of chiral H and J aggregates of cyanine dyes formed by DNA templating using stark and fluorescence spectroscopies. *The Journal of Physical Chemistry B.* 2001;105(48):12196-12201.

29. Hranisavljevic J, Dimitrijevic NM, Wurtz GA, Wiederrecht GP. Photoinduced charge separation reactions of J-aggregates coated on silver nanoparticles. *Journal of the American Chemical Society.* 2002;124(17):4536-4537.

30. Lim I-IS, Goroleski F, Mott D, et al. Adsorption of cyanine dyes on gold nanoparticles and formation of J-aggregates in the nanoparticle assembly. *The Journal of Physical Chemistry B.* 2006;110(13):6673-6682.

31. Peyratout C, Daehne L. Aggregation of thiacyanine derivatives on polyelectrolytes. *Physical Chemistry Chemical Physics.* 2002;4(13):3032-3039.

32. Gadde S, Batchelor EK, Kaifer AE. Controlling the Formation of Cyanine Dye H‐and J‐Aggregates with Cucurbituril Hosts in the Presence of Anionic Polyelectrolytes. *Chemistry-A European Journal.* 2009;15(24):6025-6031.

33. Pal SK, Datta A, Mandal D, Bhattacharyya K. Photoisomerisation of diethyloxadicarbocyanine iodide in micelles. *Chemical physics letters.* 1998;288(5-6):793-798.

34. Sabaté R, Gallardo M, de la Maza A, Estelrich J. A spectroscopy study of the interaction of pinacyanol with n-dodecyltrimethylammonium bromide micelles. *Langmuir.* 2001;17(21):6433-6437.

35. García-Jiménez F, Khramov M, Sánchez-Obregón R, Collera O. Formation of J-aggregates of cyanine dyes in bilayer lipid vesicles. *Chemical Physics Letters.* 2000;331(1):42-46.

36. Levitus M, Ranjit S. Cyanine dyes in biophysical research: the photophysics of polymethine fluorescent dyes in biomolecular environments. *Quarterly reviews of biophysics.* 2011;44(1):123-151.

37. Tatikolov AS, Costa SlM. Complexation of polymethine dyes with human serum albumin: a spectroscopic study. *Biophysical chemistry.* 2004;107(1):33-49.

38. Armitage BA. Cyanine dye–DNA interactions: intercalation, groove binding, and aggregation. *DNA binders and related subjects*: Springer; 2005: 55-76.

39. Cong M, Siraj N, Bhattarai N, et al. Ratiometric fluorescence detection of hydroxyl radical using cyanine-based binary nanoGUMBOS. *Sensors and Actuators B: Chemical.*

2018;257:993-1000.

40. Siraj N, El-Zahab B, Hamdan S, et al. Fluorescence, phosphorescence, and chemiluminescence. *Analytical chemistry.* 2015;88(1):170-202.

41. De M, Rana S, Akpinar H, et al. Sensing of proteins in human serum using conjugates of nanoparticles and green fluorescent protein. *Nature chemistry.* 2009;1(6):461.

42. McLachlan G. *Discriminant analysis and statistical pattern recognition.* Vol 544: John Wiley & Sons; 2004.

43. Fisher RA. The use of multiple measurements in taxonomic problems. *Annals of human genetics.* 1936;7(2):179-188.

44. Wang H, Wang Z, Leng Y, Wu X, Li Q. PCA plus F-LDA: A new approach to face recognition. *International Journal of Pattern Recognition and Artificial Intelligence.* 2007;21(06):1059-1068.

45. Yang J, Yang J-y. Why can LDA be performed in PCA transformed space? *Pattern recognition.* 2003;36(2):563-566.

46. Belhumeur PN, Hespanha JP, Kriegman DJ. Eigenfaces vs. fisherfaces: Recognition using class specific linear projection. *IEEE Transactions on pattern analysis and machine intelligence.* 1997;19(7):711-720.

47. Yu H, Yang J. A direct LDA algorithm for high-dimensional data—with application to face recognition. *Pattern recognition.* 2001;34(10):2067-2070.

48. Khairutdinov R, Serpone N. Photophysics of cyanine dyes: Subnanosecond relaxation dynamics in monomers, dimers, and H-and J-aggregates in solution. *The Journal of Physical Chemistry B.* 1997;101(14):2602-2610.

49. Gieseking RL, Mukhopadhyay S, Risko C, Marder SR, Brédas JL. 25th Anniversary Article: Design of Polymethine Dyes for All‐Optical Switching Applications: Guidance from Theoretical and Computational Studies. *Advanced Materials.* 2014;26(1):68-84.

50. Tatikolov AS. Polymethine dyes as spectral-fluorescent probes for biomacromolecules. *Journal of Photochemistry and Photobiology C: Photochemistry Reviews.* 2012;13(1):55-90.

51. Strekowski L. *Heterocyclic polymethine dyes: synthesis, properties and applications.* Vol 14: Springer; 2008.

52. Nordén B, Tjerneld F. Optical studies on complexes between DNA and pseudoisocyanine. *Biophysical chemistry.* 1976;6(1):31-45.

53. Cao R, Venezia CF, Armitage BA. Investigation of DNA binding modes for a symmetrical cyanine dye trication: effect of DNA sequence and structure. *Journal of Biomolecular Structure and Dynamics.* 2001;18(6):844-857.

54. Yarmoluk S, Lukashov S, Losytskyy MY, Akerman B, Kornyushyna O. Interaction of cyanine dyes with nucleic acids: XXVI. Intercalation of the trimethine cyanine dye Cyan 2 into double-stranded DNA: study by spectral luminescence methods. *Spectrochimica Acta Part A: Molecular and Biomolecular Spectroscopy.* 2002;58(14):3223-3232.

55. Chen SY, Horng ML, Quitevis EL. Picosecond spectroscopic studies of electronic energy relaxation in H-aggregates of 1, 1'-diethyl-2, 2'-dicarbocyanine on colloidal silica. *The Journal of Physical Chemistry.* 1989;93(9):3683-3688.

56. West W, Pearce S. The dimeric state of cyanine dyes. *The Journal of Physical Chemistry.* 1965;69(6):1894-1903.

57. Volkova KD, Kovalska V, Balanda A, et al. Specific fluorescent detection of fibrillar α-synuclein using mono-and trimethine cyanine dyes. *Bioorganic & medicinal chemistry.* 2008;16(3):1452-1459.

58. Yao H, Ashiba K. Highly fluorescent organic nanoparticles of thiacyanine dye: A synergetic effect of intermolecular H-aggregation and restricted intramolecular rotation. *RSC Advances.* 2011;1(5):834-838.

59. Xu S, Wu Y, Sun X, Wang Z, Luo X. A multicoloured Au NCs based cross-reactive sensor array for discrimination of multiple proteins. *Journal of Materials Chemistry B.* 2017;5(22):4207-4213.

60. Xu S, Lu X, Yao C, et al. A visual sensor array for pattern recognition analysis of proteins using novel blue-emitting fluorescent gold nanoclusters. *Analytical chemistry.* 2014;86(23):11634-11639.

CHAPTER 5: CONCLUSIONS AND FUTURE WORK

5.1 Conclusions

The research presented in this dissertation is primarily focused on development of sensors, sensor arrays, and a magnetic solid-phase extraction (MSPE) method based on use of a ***g***roup of ***u***niform ***m***aterials ***b***ased on ***o***rganic ***s***alts (GUMBOS) and the nanomaterials derived from GUMBOS (*i.e.* nanoGUMBOS). The GUMBOS compounds were used due to their favorable properties including simple synthesis, tunable physicochemical properties, and negligible vapor pressure. In Chapter 2, cyanine-based binary nanoGUMBOS were designed and synthesized for ratiometric sensing of hydroxyl radicals. It was successfully demonstrated that this binary nanoprobe displayed a higher sensitivity and selectivity toward hydroxyl radicals over other reactive oxygen species. We believe that this novel nanoprobe can play a great role in studies aimed at understanding the role of hydroxyl radicals in cellular activity. In Chapter 3, an imidazolium-dysprosium-based nanoGUMBOS was prepared using a facile method. This nanomaterial can serve as a magnetic nanoadsorbent for selective hemoglobin isolation with high adsorption capacity and good selectivity toward hemoglobin. Furthermore, in Chapter 4, a cyanine-based fluorescent sensor array composed of six TC-GUMBOS was developed to discriminate proteins. This sensor array is able to discriminate protein mixtures at different concentration levels with high accuracy. In addition, this sensor array is capable of discriminating proteins in urine at low concentrations. Based on studies outlined in this

dissertation, we can conclude that task-specific GUMBOS can be successfully designed for detection, discrimination, and extraction of a wide range of analytes.

5.2 Future Work

Use of GUMBOS as sensors or solid phase extraction (SPE) substrates is proven to be promising due to the tunable properties of GUMBOS through simple counterion alteration. Thus, more task-specific GUMBOS can be easily designed and prepared for sensing and extraction. For example, $[C_{16}mim]_5[Dy(SCN)_8]$, the material described in Chapter 3, is useful for selectively isolating hemoglobin from a complex mixture. Due to the selective interaction between $[C_{16}mim]_5[Dy(SCN)_8]$ and hemoglobin, this material or its derivatives can be further developed as hemoglobin sensors for clinic diagnosis.

In addition, while this work is primarily focused on development of novel fluorescent sensors and design of novel SPE methods, there are many areas where further investigations could be focused. For example, TC-GUMBOS, which are used to compose the sensor array illustrated in Chapter 4, are able to form different aggregates with variation of the environment. This property provides further insight into development of sensors targeting other small molecules or biological macromolecules.

VITA

Mingyan Cong was born and raised in Weihai, China. Mingyan attended Shandong University where she gained her first research experience in chemistry under Dr. Yan Bing and Dr. Li Bin. She graduated from Shandong University with a B.S. in Chemistry (May 2013). In the fall of 2013, she began her graduate studies at Louisiana State University where she was mentored by Boyd Professor Isiah Warner. Mingyan intends to graduate with a degree of Doctor of Philosophy in chemistry from Louisiana State University in December of 2018.